

# Unsteady Aerodynamic Load Control Using DBD Plasma Actuators

VARIOUS TRAILING-EDGE SHAPES AND MULTI-DBDs

A. Rezaeiha

August 17, 2015





# **Unsteady Aerodynamic Load Control Using DBD Plasma Actuators**

## **Various Trailing-edge shapes and Multi-DBDs**

MASTER OF SCIENCE THESIS

For obtaining the degree of Master of Science in Engineering Wind Energy  
at Technical University of Denmark and in Aerospace Engineering at Delft  
University of Technology.

A. Rezaeiha

August 17, 2015

European Wind Energy Master - EWEM  
DUWIND - Delft University of Technology  
Risø - Denmark Technical University



Risø DTU



Copyright © A. Rezaeiha  
All rights reserved.

EUROPEAN WIND ENERGY MASTER - EWEM  
OF  
ROTOR DESIGN TRACK

The undersigned hereby certify that they have read and recommend to the European Wind Energy Master - EWEM for acceptance a thesis entitled “**Unsteady Aerodynamic Load Control Using DBD Plasma Actuators**” by **A. Rezaeiha** in partial fulfillment of the requirements for the degree of **Master of Science**.

Dated: August 17, 2015

Supervisor:

\_\_\_\_\_  
Dr. Marios Kotsonis of Delft University of Technology

Supervisor:

\_\_\_\_\_  
Dr. Martin O.L. Hansen of Denmark Technical University

Reader:

\_\_\_\_\_  
Prof.dr.ir. G.J.W. van Bussel (Gerard) of Delft University of Technology

Reader:

\_\_\_\_\_  
Theo Michelis, M.Sc. of Delft University of Technology



---

# Summary

Big wind farms with big wind turbines are more cost effective and produce greener electricity compared to smaller ones. This is one of the reasons for the growth of wind turbine size during the last 3 decades. However, as wind turbines become bigger, their blades become longer, thicker and heavier. This results in larger unsteady loads on blades which is an important limitation for their life time and their size growth. Flow control has emerged as the promising solution both for improving the aerodynamic efficiency and controlling the unsteady loads on wind turbine blades. DBD plasma actuator is an active flow control mechanism that has shown high potentials for unsteady load control with the capability to change lift coefficient to a significant amount with a very fast response time.

The current research first intends to identify the variations of angle of attack and lift coefficient on wind turbine blades as a result of gravitational loads, mass and aerodynamic imbalances, turbulence, wind shear, yawed inflow and tower shadow and investigate their corresponding frequencies and the fatigue damage from the blade root bending moments. Then, (single and multi) DBD plasma actuator with different configurations will be used on three different trailing-edge shapes (round, half-round and sharp) of modified version of 'NACA64-2-A015' airfoil to control the aerodynamic loads via circulation control. This is managed either by manipulation of Kutta condition or acting as a virtual Gurney flap. Furthermore, it is intended to investigate the correlation between the frequency of actuation, frequency of vortex shedding and the amount of lift enhancement.

It is hoped that the results of this research can be a contribution to active load control on wind turbine blades and other load control applications.



---

# Acknowledgements

I would like to thank all the individuals who helped me during different phases of my thesis, from early planning, simulations, experiments, processing the result and writing and editing the report. First, I wish to thank my supervisors, Marios from TU Delft and Martin from DTU for supervising my thesis. A special thanks goes to Marios for our regular meetings and his help during all steps of the thesis, specially experiments and post processing. I would also like to thank my friend, Theo, for his assistance with preparing the setup for the hot-wire and PIV experiments and post processing with Davis. Moreover, I would like to thank all my friends and fellows at TU Delft, DTU and especially EWEM program for making this two year an amazing journey. Last but not least, my gratitude goes to all my professors at TU Delft and DTU plus EWEM administrative and coordinative team; especially Carlos, Wim, Zarah, Linda and Soumaya; which had a great contribution to me getting to the graduation point.

On a personal level, firstly I would like to thank my mother and my late father for all their devotion and motivation in all moments of my life. They are the reason for me being what I am today. Secondly, I would like to thank my lovely wife for all her continuous support and love during the tough moments far from home. For the last word, I would like to dedicate this work to my love, Sahba, and my new-born son, Radin.

Delft, The Netherlands  
August 17, 2015

A. Rezaeiha



# CONTENTS

<b>Acknowledgements</b> . . . . .	<b>vii</b>
<b>List of Figures</b> . . . . .	<b>xv</b>
<b>List of Tables</b> . . . . .	<b>xvii</b>
<b>Nomenclature</b> . . . . .	<b>xix</b>
<b>1 Introduction</b> . . . . .	<b>1</b>
1.1 Introductory background . . . . .	1
1.2 Gap statement . . . . .	2
1.3 Aims and objectives . . . . .	3
1.4 Significance/Contribution to the discipline . . . . .	3
1.5 Outline . . . . .	3
<b>2 Unsteady Loads on Wind Turbines</b> . . . . .	<b>5</b>
2.1 Introduction . . . . .	5
2.2 The main frequency range of unsteady loads . . . . .	6
2.3 <i>HAWC2</i> simulations . . . . .	9
2.3.1 Frequency analysis . . . . .	10
2.3.2 Fatigue analysis . . . . .	14
2.3.3 Influence on angle of attack and variations of lift . . . . .	25
2.3.4 Conclusions for an 'Active Load Control' system . . . . .	36
<b>3 Load Control for Wind Turbine Blades</b> . . . . .	<b>39</b>
3.1 Flow control . . . . .	39
3.2 Flow control on wind turbines . . . . .	39
3.2.1 Active load control on wind turbine blades . . . . .	41
3.3 DBD Plasma Actuators . . . . .	45
3.3.1 Introduction to Plasma Actuators . . . . .	45
3.3.2 Physics of DBD Plasma Actuator . . . . .	46
3.3.3 DBD plasma actuators for flow control . . . . .	52
<b>4 Methodology and Experimental Set-up</b> . . . . .	<b>53</b>
4.1 Airfoil models . . . . .	53
4.2 Wind tunnel . . . . .	54
4.3 Plasma actuator facility . . . . .	54
4.3.1 Plasma actuator racks . . . . .	54
4.3.2 Plasma actuator table . . . . .	56
4.4 Force measurement . . . . .	56
4.4.1 Force sensor . . . . .	56
4.4.2 Force balance . . . . .	56
4.4.3 Wind tunnel correction . . . . .	58
4.4.4 Test matrix . . . . .	59
4.5 Particle Image Velocimetry (PIV) . . . . .	61
4.5.1 Test matrix . . . . .	65
4.6 Power measurement . . . . .	65
4.6.1 Integrated capacitor method . . . . .	66
4.6.2 Test matrix . . . . .	67
<b>5 Results and discussion</b> . . . . .	<b>69</b>
5.1 Quiescent-flow force measurements . . . . .	69
5.2 Aerodynamic loads and PIV flow field measurements . . . . .	72
5.2.1 $c_l$ as a function of actuator settings . . . . .	73
5.2.2 Round trailing-edge . . . . .	75
5.2.3 Sharp trailing-edge . . . . .	86
5.2.4 Half-round trailing-edge . . . . .	94

5.3	Electrical consumed power measurements . . . . .	105
<b>6</b>	<b>Conclusion . . . . .</b>	<b>109</b>
6.1	Concluding remarks . . . . .	109
6.2	Future recommendations . . . . .	110
	<b>References . . . . .</b>	<b>111</b>
<b>A</b>	<b>Appendix A: Correction for the ratio between the actuator length and airfoil span . .</b>	<b>115</b>
<b>B</b>	<b>Appendix B: Plasma model for prediction of body force spatial distribution . . . . .</b>	<b>117</b>

# LIST OF FIGURES

1.1	Wind turbine size growth since 1985. [68]	1
2.1	Energy spectrum of turbulence and loads due to rotational sampling. [67]	6
2.2	Turbulence in neutral condition at different heights. [21]	7
2.3	Campbell diagram of NREL 5MW reference wind turbine. [36]	8
2.4	Energy spectrum of in-plane -left- and out-of-plane -right- blade root moments of NREL 5MW Reference wind turbine. [44]	8
2.5	Distribution of turbulence intensity with wind speed at hub height.	10
2.6	Frequency analysis of unsteady load by gravity and imbalances.	12
2.7	Frequency analysis of unsteady load by tower shadow.	12
2.8	Frequency analysis of unsteady load by wind shear.	13
2.9	Frequency analysis of unsteady load by yawed inflow.	13
2.10	Frequency analysis of unsteady load by turbulence at TI of 0.16.	14
2.11	Frequency analysis of unsteady load on blade root bending moment.	14
2.12	Weibull distribution with $k = 2.03$ and $A = 11.9$ utilized for fatigue calculation.	15
2.13	PDF and Weibull distribution fitted to the wind data from the mast.	15
2.14	Normalized LEFL values with the reference case.	17
2.15	Fatigue damage distribution vs. wind speed and LEFL values for case 1.	17
2.16	Normalized LEFL values with the reference case for various TI as a result of tower shadow.	18
2.17	Fatigue damage distribution vs. wind speed and LEFL values for case 4.	19
2.18	Normalized LEFL values with the reference case for various TI as a result of wind shear.	19
2.19	Fatigue damage distribution vs. wind speed and LEFL values for case 5.	20
2.20	Normalized LEFL values with the reference case for various TI.	21
2.21	Fatigue damage distribution vs. wind speed and LEFL values for case 9.	21
2.22	Fatigue damage distribution vs. wind speed and LEFL values for case 30.	22
2.23	Normalized LEFL values with the reference case for various Yaw angles in the absence of turbulence.	23
2.24	Normalized LEFL values with the reference case for various Yaw angles in the presence of turbulence.	24
2.25	Fatigue damage distribution vs. wind speed and LEFL values for case 32.	24
2.26	Fatigue damage distribution vs. wind speed and LEFL values for case 33.	25
2.27	Contributions of unsteady loads to overall Mx (flapwise) LEFL.	26
2.28	Contributions of unsteady loads to overall My (edgewise) LEFL.	26
2.29	Contributions of unsteady loads to overall Mz LEFL.	27
2.30	DTU-10MW-RWT airfoils' polars.	28
2.31	DTU-10MW-RWT airfoils' design values.	28
2.32	Variations of $\alpha$ vs. radial position and wind speed for the reference case.	29
2.33	Variations of $\alpha$ and $C_L$ with shaded standard deviations vs. radial position at $8m/s$ for the reference case.	30
2.34	Variations of $C_L$ vs. $\alpha$ for wind speed $4-24m/s$ shown together with the corresponding airfoil plot for the reference case.	31
2.35	Variations of $C_L$ vs. azimuth for the reference case.	32
2.36	Variations of mean values of $\alpha$ and $C_L$ for various unsteady loading cases.	33
2.37	Influence of unsteady loads on angle of attack.	34
2.38	Influence of unsteady loads on angle of attack.	34
2.39	Variations of standard deviation of lift coefficient at 3 different radial positions on blade ( $0.35, 0.56, 0.9 \frac{r}{R}$ representing max, average and min values respectively) for various unsteady loading scenarios.	35
2.40	Contour of angle of attack for Case 30 under a combination of turbulence, wind shear, tower shadow, gravity, mass and aerodynamic imbalances.	35
2.41	Influence of unsteady loads on angle of attack.	37
3.1	Flow control objectives.[26]	40
3.2	Flow control methods.	40

3.3	Achieved $\Delta C_L$ for various flow control methods.[8]	41
3.4	Schematic SDBD plasma actuator. [18]	45
3.5	Schematic of electron impact with a neutral atom in EI ionization method. [34]	47
3.6	Light emission from a SDBD captured with a PMT focused on a narrow 2D area of plasma. [49]	49
3.7	Schematic of electron impact with a neutral atom in EI ionization method. [34]	50
3.8	Application of DBD plasma actuator in flow control.	52
4.1	The original and modified versions of NACA64-2-A015 airfoil with sharp, round and half-round trailing-edges.	54
4.2	The schematic of the V-tunnel used in the experiments: 1)measurement room; 2)fan room; 3)fan; 4)settling chamber; 5&6) spikes; 7)contraction; 8)noise suppressor.	55
4.3	The KD40S force sensor.	56
4.4	The schematic of the force measurement balance employed in the experiments [52].	57
4.5	The schematic of the force and moments applied on the force balance [52].	57
4.6	The schematic of the aerodynamic loads and moments applied on airfoil axis and aerodynamic center [52].	58
4.7	Vortex image system used for slipstream curvature correction in a 2D open jet test section[12]. The variable 'd' is the distance from the airfoil leading edge to nozzle exit.	59
4.8	Illustration of how the correction in angle of attack changes the $C_L - \alpha$ curve [52].	59
4.9	Actuation modes for different trailing-edge shapes. The position of the plasma onset is shown with a red circle. Three different positions (A,B and C) were investigated for the sharp trailing-edge.	61
4.10	Illustration of arrangement of laser, camera and optics for the PIV experiments.	63
4.11	Schematic of the electric circuit of the integrated capacitor method [3].	66
5.1	Variations of force with carrier frequency for various applied voltages and dielectric thicknesses.	70
5.2	Variations of force with applied voltage for various carrier frequencies and dielectric thicknesses.	71
5.3	Variations of force with dielectric thickness for various applied voltages and carrier frequency.	71
5.4	Momentum coefficient ( $c_\mu$ ) as a function of applied voltages and carrier frequency.	72
5.5	Momentum coefficient ( $c_\mu$ ) as a function of dielectric thickness.	72
5.6	Variations of lift coefficient (per unit length of the actuator) as a function of carrier frequency (left) and applied voltage (right) for the round trailing edge. The actuator is positioned at centerline of the trailing-edge (Kutta mode).	73
5.7	Variations of lift coefficient (per unit length of the actuator) as a function of carrier frequency (left) and applied voltage (right) for the half-round trailing edge. The actuator is positioned at centerline of the trailing-edge (Kutta mode).	74
5.8	Variations of lift coefficient (per unit length of the actuator) as a function of carrier frequency (left) and applied voltage (right) for the sharp trailing edge. The actuator is positioned as a tab (position A).	74
5.9	Variations of lift coefficient (per unit length of the actuator) as a function of pulsation frequency (top) and duty cycle (bottom) for the round trailing edge. The actuator is positioned at centerline of the trailing-edge (Kutta mode).	75
5.10	Lift, drag and moment coefficient as a function of angle of attack for the round trailing edge. The actuator is positioned at centerline of the trailing-edge (Kutta mode). ( $c_\mu = 0.3\%$ , $Re = 145,000$ )	76
5.11	Variations of lift coefficient (per unit length of the actuator) relative to baseline as a function of freestream velocity and angle of attack for the round trailing-edge. The actuator is positioned at centerline of the trailing-edge blowing towards pressure side (Kutta mode).	77
5.12	Variations of lift coefficient (per unit length of the actuator) relative to baseline as a function of freestream velocity and angle of attack for the round trailing-edge. The actuator is positioned at centerline of the trailing-edge blowing towards either pressure side or suction side.	78
5.13	Time-averaged velocity vector field for the round trailing-edge. The actuator is positioned at centerline of the trailing-edge blowing towards pressure side (Kutta mode). ( $\alpha = 0\&5^\circ$ , $c_\mu = 0.3\%$ , $U = 10m/s$ , $Re = 145,000$ )	79
5.14	Location of the maximum streamwise velocity deficit in the wake for plasma 'off' and 'on' for the round trailing-edge. The actuator is positioned at centerline of the trailing-edge (Kutta mode). ( $c_\mu = 0.3\%$ , $U = 10m/s$ , $Re = 145,000$ )	80
5.15	Wake deflection angle ( $\theta$ ) as a result of plasma actuation versus $\alpha$ for the round trailing-edge. The actuator is positioned at centerline of the trailing-edge (Kutta mode). ( $c_\mu = 0.3\%$ , $U = 10m/s$ , $Re = 145,000$ )	80

5.16	Flow streamlines for the round trailing-edge. The actuator is positioned at centerline of the trailing-edge blowing towards the pressure side (Kutta mode). ( $c_\mu = 0.3\%$ , $U = 10m/s$ , $Re = 145,000$ ) . . . . .	81
5.17	Time-averaged velocity vector field for the round trailing-edge. The actuator is positioned at centerline of the trailing-edge blowing towards suction side (Kutta mode). ( $\alpha = 10\&14^\circ$ , $c_\mu = 0.3\%$ , $U = 10m/s$ , $Re = 145,000$ ) . . . . .	82
5.18	Flow streamlines for the round trailing-edge. The actuator is positioned at centerline of the trailing-edge blowing towards suction side (Kutta mode). ( $c_\mu = 0.3\%$ , $U = 10m/s$ , $Re = 145,000$ ) . . . . .	83
5.19	Turbulent kinetic energy for the round trailing-edge. The actuator is positioned at centerline of the trailing-edge (Kutta mode). ( $\alpha = 0\&5^\circ$ , $c_\mu = 0.3\%$ , $U = 10m/s$ , $Re = 145,000$ ) . . . . .	83
5.20	Turbulent kinetic energy for the round trailing-edge. The actuator is positioned at centerline of the trailing-edge (Kutta mode). ( $\alpha = 10\&14^\circ$ , $c_\mu = 0.3\%$ , $U = 10m/s$ , $Re = 145,000$ ) . . . . .	84
5.21	Normalized, non-dimensional vorticity fields of the first POD mode for the round trailing-edge. The actuator is positioned at centerline of the trailing-edge blowing to pressure side (Kutta mode). ( $\alpha = 0\&5^\circ$ , $c_\mu = 0.3\%$ , $U = 10m/s$ , $Re = 145,000$ ) . . . . .	84
5.22	Normalized, non-dimensional vorticity fields of the first POD mode for the round trailing-edge. The actuator is positioned at centerline of the trailing-edge blowing to suction side (Kutta mode). ( $\alpha = 0\&5^\circ$ , $c_\mu = 0.3\%$ , $U = 10m/s$ , $Re = 145,000$ ) . . . . .	85
5.23	Lift, drag and moment coefficient as a function of angle of attack for the round trailing edge. One actuator is positioned at centerline of the trailing-edge (Kutta mode) and the second one on the pressure side blowing upstream (tab mode). . . . .	85
5.24	Variations of lift coefficient (per unit length of the actuator) relative to baseline as a function of freestream velocity and angle of attack for the round trailing-edge. One actuator is positioned at centerline of the trailing-edge (Kutta mode) and the second one on the pressure side blowing upstream (tab mode). . . . .	86
5.25	Variations of lift coefficient as a function of pulsation frequency for the round trailing-edge. The actuator is operating as Npush mode. . . . .	87
5.26	Variations of vortex shedding frequency as a function of freestream velocity and angle of attack for the round (top) and half-round (bottom) trailing-edges. . . . .	87
5.27	Lift, drag and moment coefficient as a function of angle of attack for the sharp trailing edge. The actuator is positioned on the pressure side blowing upstream (tab mode - pos A). . . . .	88
5.28	Variations of lift coefficient (per unit length of the actuator) relative to baseline as a function of freestream velocity and angle of attack for the sharp trailing-edge. The actuator is positioned on the pressure side blowing upstream (tab mode - pos A). . . . .	89
5.29	Variations of lift coefficient (per unit length of the actuator) relative to baseline as a function of freestream velocity and angle of attack for the sharp trailing-edge. The actuator is positioned either on the pressure or suction side blowing upstream at position A. . . . .	89
5.30	Variations of lift coefficient (per unit length of the actuator) relative to baseline as a function of freestream velocity and angle of attack for the sharp trailing-edge and different positioning of the virtual plasma tab. The actuator is positioned on the pressure side blowing upstream (tab mode - pos A, B and C). . . . .	90
5.31	Time-averaged velocity vector field for the sharp trailing-edge. The actuator is positioned on the pressure side blowing upstream (tab mode - pos A). ( $\alpha = 0\&5^\circ$ , $c_\mu = 0.3\%$ , $U = 10m/s$ , $Re = 145,000$ ) . . . . .	91
5.32	Time-averaged velocity vector field of the boundary layer for the sharp trailing-edge. The actuator is positioned on the pressure side blowing upstream (tab mode - pos A). The position of the plasma onset is shown with a black circle. ( $\alpha = 0\&5^\circ$ , $c_\mu = 0.3\%$ , $U = 10m/s$ , $Re = 145,000$ ) . . . . .	92
5.33	Time-averaged velocity vector field for the sharp trailing-edge. The actuator is positioned on the pressure side blowing upstream (tab mode - pos A). ( $\alpha = 0\&5^\circ$ , $c_\mu = 0.3\%$ , $U = 10m/s$ , $Re = 145,000$ ) . . . . .	93
5.34	Turbulent kinetic energy for the sharp trailing-edge. The actuator is positioned on the pressure side blowing upstream (tab mode - pos A). ( $\alpha = 0\&5^\circ$ , $c_\mu = 0.3\%$ , $U = 10m/s$ , $Re = 145,000$ ) . . . . .	94
5.35	Turbulent kinetic energy for the sharp trailing-edge. The actuator is positioned on the pressure side blowing upstream (tab mode - pos A). ( $\alpha = 0\&5^\circ$ , $c_\mu = 0.3\%$ , $U = 10m/s$ , $Re = 145,000$ ) . . . . .	95
5.36	Normalized, non-dimensional vorticity fields of the first POD mode for the sharp trailing-edge. The actuator is positioned on the suction side blowing upstream (tab mode - pos A). ( $\alpha = 0\&5^\circ$ , $c_\mu = 0.3\%$ , $U = 10m/s$ , $Re = 145,000$ ) . . . . .	95

5.37	Fluctuating energy budget of first 8 POD modes for the sharp trailing-edge. The actuator is positioned on the pressure side blowing upstream (tab mode - pos A). ( $\alpha = 0\&5^\circ, c_\mu = 0.3\%, U = 10m/s, Re = 145,000$ ) . . . . .	96
5.38	Lift, drag and moment coefficient as a function of angle of attack for the half-round trailing edge. The actuator is positioned at centerline of the trailing-edge (Kutta mode). . . . .	97
5.39	Variations of lift coefficient (per unit length of the actuator) relative to baseline as a function of freestream velocity and angle of attack for the half-round trailing-edge. The actuator is positioned at centerline of the trailing-edge (Kutta mode). . . . .	97
5.40	Time-averaged velocity vector field for the half-round trailing-edge. The actuator is positioned at centerline of the trailing-edge (Kutta mode). ( $\alpha = 0\&5^\circ, c_\mu = 0.3\%, U = 10m/s, Re = 145,000$ ) . . . . .	98
5.41	Location of the maximum streamwise velocity deficit in the wake for plasma 'off' and 'on' for the round trailing-edge. The actuator is positioned at centerline of the trailing-edge (Kutta mode). ( $c_\mu = 0.3\%, U = 10m/s, Re = 145,000$ ) . . . . .	99
5.42	Wake deflection angle ( $\theta$ ) as a result of plasma actuation versus $\alpha$ for the round trailing-edge. The actuator is positioned at centerline of the trailing-edge (Kutta mode). ( $c_\mu = 0.3\%, U = 10m/s, Re = 145,000$ ) . . . . .	99
5.43	Turbulent kinetic energy for the half-round trailing-edge. The actuator is positioned at centerline of the trailing-edge (Kutta mode). ( $\alpha = 0\&5^\circ, c_\mu = 0.3\%, U = 10m/s, Re = 145,000$ ) . . . . .	100
5.44	Normalized, non-dimensional vorticity fields of the first POD mode for the half-round trailing-edge. The actuator is positioned at centerline of the trailing-edge (Kutta mode). ( $\alpha = 0\&5^\circ, c_\mu = 0.3\%, U = 10m/s, Re = 145,000$ ) . . . . .	101
5.45	Fluctuating energy budget of first 8 POD modes for the half-round trailing-edge. The actuator is positioned on the centerline of the trailing-edge (Kutta mode). ( $c_\mu = 0.3\%, U = 10m/s, Re = 145,000$ ) . . . . .	101
5.46	Lift, drag and moment coefficient as a function of angle of attack for the half-round trailing edge. The actuator is positioned on the pressure side blowing upstream (tab mode). . . . .	102
5.47	Variations of lift coefficient (per unit length of the actuator) relative to baseline as a function of freestream velocity and angle of attack for the half-round trailing-edge. The actuator is positioned on the pressure side blowing upstream (tab mode). . . . .	103
5.48	Time-averaged velocity vector field of the boundary layer for the half-round trailing-edge. The actuator is positioned on the pressure side blowing upstream (tab mode). The position of the plasma onset is shown with a white circle. ( $c_\mu = 0.3\%, U = 10m/s, Re = 145,000$ ) . . . . .	103
5.49	Lift, drag and moment coefficient as a function of angle of attack for the half-round trailing edge. One actuator is positioned at centerline of the trailing-edge (Kutta mode) and the second one on the pressure side blowing upstream (tab mode). . . . .	104
5.50	Variations of lift coefficient (per unit length of the actuator) relative to baseline as a function of freestream velocity and angle of attack for the half-round trailing-edge. One actuator is positioned at centerline of the trailing-edge (Kutta mode) and the second one on the pressure side blowing upstream (tab mode). . . . .	104
5.51	Variations of lift coefficient (per unit length of the actuator) relative to baseline as a function of freestream velocity and angle of attack for the half-round trailing-edge for different actuation modes (Kutta, tab and 2push modes). . . . .	105
5.52	Applied and capacitor voltages (left) and Lissajous curve for one period (right) at $40kV_{pp}$ and $1000Hz$ carrier frequency. The dielectric thickness is $3mm$ . . . . .	106
5.53	Electrical power consumption of the plasma actuator as a function of carrier frequency (left) and applied voltages (right). . . . .	106
5.54	Electrical power consumption of the plasma actuator as a function of dielectric thickness. . . . .	107
A.1	Change in lift coefficient by the actuator per unit length of the actuator (top) and correction factor for force coefficient (bottom) versus the ratio between the actuator length and airfoil span. . . . .	116
B.1	Light intensity of plasma actuator using Sensicam. Plasma onset is at about $x = 0$ . . . . .	118
B.2	Light intensity of plasma actuator using Sensicam and a $394nm$ bandpass filter which only allows emission from some energetic states of Nitrogen. Plasma onset is at about $x = 0$ . . . . .	118
B.3	Defined spatial distribution for charge density based on plasma emission. . . . .	119
B.4	Geometry, unstructured and structured grid created to solve the Poisson equation in MATLAB pdetool. . . . .	120
B.5	Electric potential calculated for the plasma actuator in MATLAB pdetool. The upper rectangular represents the plasma containing region. . . . .	120

B.6 Electric potential calculated for the plasma actuator in MATLAB pdetool interpolated to structured grid. . . . . 121

B.7 Electric field calculated for the plasma actuator in MATLAB pdetool. . . . . 121

B.8 Electric field calculated for the plasma actuator in MATLAB pdetool interpolated to structured grid. . . . . 122

B.9 Body force spatial distribution calculated for the plasma actuator. . . . . 122

B.10 Body force spatial distribution calculated for the plasma actuator. . . . . 123

B.11 Flowchart of iterative process to calculate the body force spatial distribution for the plasma actuator. . . . . 124



# LIST OF TABLES

2.1	Simulation general inputs into HAWC2 and statistics. . . . .	9
2.2	Structural and wind inputs into HAWC2. . . . .	10
2.3	Aerodynamic inputs into HAWC2. . . . .	10
2.4	Description of HAWC2 simulation matrix. . . . .	11
2.5	Lifetime equivalent fatigue loads (LEFL) for 34 various unsteady loading cases. . . . .	16
2.6	Contributions (%) to total LEFL. . . . .	23
2.7	<i>DTU-10MW-RWT</i> airfoils and design values. . . . .	27
3.1	Comparison of advantages and disadvantages of passive and active load control methods for wind turbines. (P=passive; A=active) . . . . .	44
4.1	Dimensions of the airfoils. . . . .	53
4.2	Test matrix for the actuator settings experiments. . . . .	60
4.3	Test matrix for the main force measurement experiments. . . . .	60
4.4	Dimensions and positions of the electrodes for round trailing edge [mm]. . . . .	62
4.5	Dimensions and positions of the electrodes for half-round trailing edge [mm]. . . . .	62
4.6	Dimensions and positions of the electrodes for sharp trailing edge [mm]. . . . .	62
4.7	FOV of the camera for different trailing-edge shapes. . . . .	63
4.8	PIV hardware employed in the tests. . . . .	64
4.9	Test matrix for the PIV experiments. . . . .	65
4.10	PIV setup parameters for the experiments. . . . .	65
4.11	The test matrix for the power measurement experiments. . . . .	67



---

# Nomenclature

$A$	Weibull distribution scale factor
$C_D$	Coefficient of drag
$C_L$	Coefficient of lift
$C_m$	Coefficient of moment
$C_{m,c/4}$	Aerodynamic pitching moment around quarter chord
$E$	Electric field
$E$	Fluctuating energy budget
$E_b$	Break down electric field
$E_s$	Sustaining electric field
$J$	Total momentum of the induced jet of the actuator
$K$	Electron temperature
$L$	Lift
$L$	Lift
$L_{act.}$	Actuator lift
$L_{ce}$	Length of covered electrode
$R$	Blade radius
$S$	Area
$U_\infty$	Freestream velocity
$V$	Electric voltage
$V$	Resultant velocity
$V_{ap}$	Applied voltage
$V_{pp}$	Peak-to-peak voltage
$\Delta c_l/m$	Change in lift coefficient per unit length of the actuator
$\Gamma$	Circulation
$\alpha$	Angle of attack
$\epsilon$	Dielectric coefficient
$\epsilon$	Dielectric constant

$\epsilon_0$	Vacuum permittivity
$\epsilon_r$	Dielectric constant/relative permittivity
$\omega$	Angular frequency of unsteadiness
$\rho_c$	Charge density
$\rho_\infty$	Freestream density
$\theta$	Wake deflection angle
$c$	Chord
$c$	Chord
$c_l/m$	Lift coefficient per unit length of the actuator
$c_\mu$	Actuator momentum coefficient
$c_{l,on}$	Lift coefficient with actuator on
$dc_l/m$	Change in lift coefficient per unit length of the actuator
$f$	Force density or force per unit volume
$f_c$	Carrier frequency of the actuator
$f_p$	Pulsation frequency of the actuator
$g$	Gap spacing
$h$	Dielectric material thickness
$k$	Reduced frequency
$k$	Weibull distribution shape factor
$n$	Number density
$q_\infty$	Dynamic pressure
$r$	Radial position on blade
$t_d$	Dielectric thickness
$x$	Distance from the edge of the covered electrode
$1P, 2P, 3P, \dots$	Periodic Excitations
$AC - DBD$	Alternating-Current DBD
$AEP$	Annual Energy Production
$BEM$	Blade element momentum
$CoE$	Cost of Energy
$DBD$	Dielectric Barrier Discharge
$EFL$	Equivalent fatigue load
$FOV$	Field of view
$HAWC2$	Horizontal Axis Wind turbine simulation Code 2nd generation
$IPC$	Individual pitch control
$LDV$	Laser Doppler Velocimetry
$LEFL$	Lifetime equivalent fatigue load
$NREL$	National Renewable Energy Laboratory
$NTM$	Normal turbulence model
$Nd : YAG$	Neodymium-doped yttrium aluminum garnet
$PDF$	Probability density function
$PIV$	Particle image velocimetry
$POD$	Proper orthogonal decomposition
$PTU$	programmable timing unit
$SDBD$	single DBD

<i>SH</i>	Wind shear
<i>TE</i>	Trailing-edge
<i>TI</i>	Turbulence intensity (%)
<i>TKE</i>	Turbulent kinetic energy
<i>TS</i>	Tower shadow
<i>VG</i>	Vortex generator
<i>Y</i>	Yaw
<i>ns – DBD</i>	Nano-second DBD
<i>Hz</i>	Hertz
<i>MW</i>	Mega-Watts
<i>eV</i>	Electron Volts
<i>ms</i>	Milli-seconds



## Introduction

### 1.1 Introductory background

Wind energy is a promising alternative to fossil fuels with many advantages including sustainability, renewability, high-potential, and being domestic. However, it still has to overcome the challenge of cost of energy (CoE) to become competitive to conventional energies. Studies have shown that big wind turbines - bigger in size but less in number - are more cost-efficient [68] and produce greener electricity [13] than a wind farm with the same annual energy production (AEP) with more but smaller wind turbines. This is one of the main reasons for the rapid size growth of wind turbines Figure 1.1.

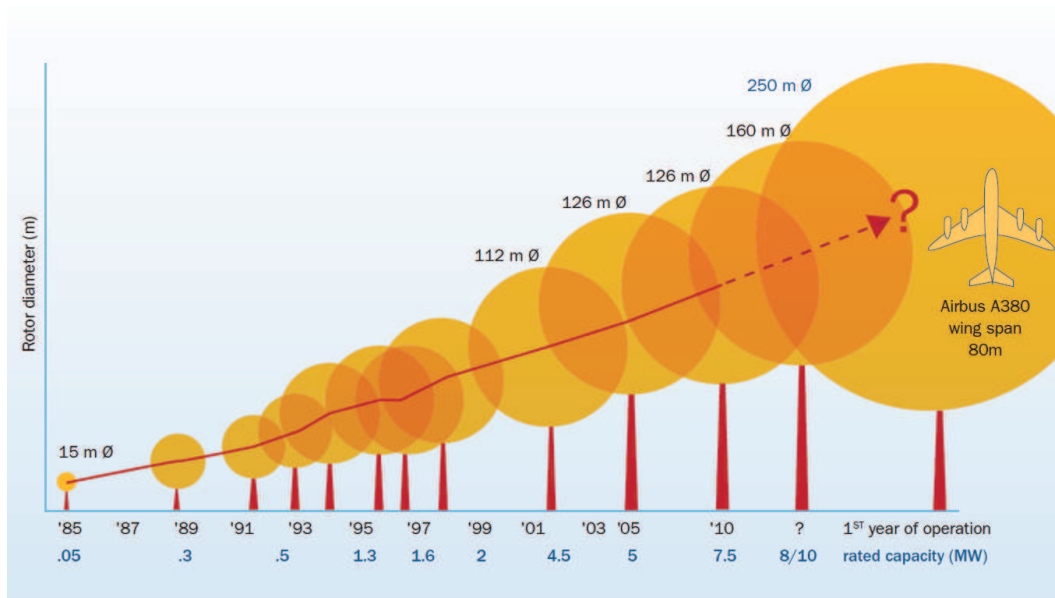


*Figure 1.1: Wind turbine size growth since 1985. [68]*

As wind turbine become bigger, blades become heavier, therefore, higher loads are exerted on the blade

roots. Consequently they require thicker blade sections in order to increase their second moment of inertia and consequently their bending stiffness.

On the other hand, due to the intrinsically unsteady nature of the incoming flow to wind turbines together with their rotational operating conditions, these loads of high magnitude are significantly fluctuating as well.

These highly-variant loads can be a result of wind shear, turbulence, yawed inflow, tower shadow, imbalances and gravitational loads. These fluctuations are extremely of high importance as during long term operation can result in structural fatigue and dramatically decrease the turbine lifetime. These unsteady loads can be significantly mitigated through aerodynamic flow control on wind turbine blades.

Aerodynamic flow control for general flow applications [26, 15] as well as in the flow regime corresponding to wind turbines [8, 35, 50] has been extensively investigated by many researchers and various flow control mechanisms have been applied to achieve higher aerodynamic efficiency and control the unsteady loads on wind turbine blades in various operating conditions.

Among the passive and active flow control mechanisms/methods for wind turbines, vortex generators [29, 63], Gurney flaps [16, 74], plasma actuators [48, 20], suction [75, 19], blowing [70, 28, 60], trailing-edge flaps/microtabs [69, 5, 10], morphing blades [72], and synthetic jets [46] each have been studied to some extent to this date and the studies cover a range of experimental and numerical studies.

The aforementioned methods addressed the flow in this regime with respect to separation control (delay or augmentation), circulation control, unsteady load control, transition control (boundary layer stabilization and active wave cancellation), noise suppression, wing tip vortex control, and drag reduction (skin friction drag and form drag).

Despite the many efforts, there is still a great need for improvements in unsteady loads for wind turbine blades as the unsteady loads are still a major concern for fatigue and an important hindrance for scaling-up the size of the wind turbines and are highly desired to be alleviated.

Having said that, the main motivation for this research is the application of DBD plasma actuators for unsteady load control applications.

## 1.2 Gap statement

Recently, numerical research by Zhang et al. [73] and experimental research by Kotsonis and Pul [52, 39] showed the capabilities of DBD plasma actuators to control the aerodynamic loads on a rounded trailing-edge airfoil. The change in loads was done with manipulation of Kutta-condition and consequently changing the circulation around the airfoil. However, the conducted studies were more targeted to prove the concept and were limited with regard to several aspects as some are listed below:

1. The spacing of the actuator electrodes were rough on the round trailing edge due to the low diameter of the model.
2. Limited positions were considered for the actuator.
3. The studies was focused on the effect of actuation on only one trailing-edge shape (round).
4. Limited Reynolds numbers (140,000-280,000) were studied.
5. The actuator applied voltage was limited by the HV amplifier to  $35kV_{pp}$ .
6. The number of actuators were limited to one.
7. The correlation between frequency of the actuator (carrier or pulsation), the change in aerodynamic loads and vortex shedding frequency at trailing edge was not studied.

Furthermore, to the best knowledge of the author, the transient unsteady effect of the plasma actuation at the trailing-edge has not been studied yet. Moreover, a relationship between the electrical inputs to the actuator and actuator effectiveness needs to be established.

## 1.3 Aims and objectives

Considering the discussed gaps, the following research intends to conduct a series of planar particle image velocimetry (PIV) measurements together with force measurement for a range of angle of attack, Reynolds number, three different trailing-edge geometries, one and double actuators and various actuation modes to target the aforementioned gaps while pursuing the following objectives:

1. Understanding the effect of plasma actuation for different airfoil trailing-edge shapes with different combination of angles of attack, Reynolds number and actuation modes on aerodynamic loads and wake dynamics
2. Studying the potential of plasma blowing on pressure side or suction side for load control applications
3. Understanding the correlation between the actuator frequency,  $\Delta c_l$  and vortex shedding frequency

## 1.4 Significance/Contribution to the discipline

The author believes that realization of the above objectives can be helpful in designing wind turbine blades with higher efficiency, lower mass, lower cost and higher reliability. This can be a step to have more efficient wind farms, lower CoE and subsequently more widespread utilization of renewable energy, finally approaching a greener sustainable planet.

## 1.5 Outline

Chapter 2 will give an overview on the unsteady loads on wind turbine blades and will identify the effect of unsteady loads based on their frequency of occurrence and their impact on angle of attack, lift coefficient and lifetime equivalent fatigue loads (LEFL) using a series of aeroelastic simulations with the DTU wind turbine-dedicated aero-servo-elastic software (HAWC2).

Chapter 3 will review active load control methods studied by the literature. The chapter will continue on the physics and applications of DBD plasma actuators and how they can contribute to active load control on wind turbine blades.

Chapter 4 will discuss the methods that will be employed to achieve the objectives of the project. It will have a section on PIV, force measurements, and power measurements. Moreover, it will provide the experimental set-up designed for the tests, models to be tested, facilities, test matrix, calibration, post-processing and correction procedures.

Chapter 5 will present the results of the experiments and discuss the understandings based on the observations.

Chapter 6 will be the conclusion and future recommendations for the continuation of the research.



# Unsteady Loads on Wind Turbines

## 2.1 Introduction

The unsteady loads on wind turbines are usually considered based on their frequency of occurrence with respect to rotational frequency of the blades. Therefore, loads with the same frequency as rotational frequency are named as 1P loads. Similarly, loads with frequency twice the rotational frequency are named as 2P loads. The same principle defines 3P, 4P, ... loads respectively.

The unsteady loads on wind turbines can be categorized in three groups:

- Harmonic loads
- Non-harmonic periodic loads
- Non-periodic random loads

Harmonic loads for a wind turbine can be a result of aerodynamic imbalance, gravity and mass imbalance and they are 1P loads.

Non-harmonic periodic loads are complex cyclic loadings which can be expressed as a Fourier series of 1P, 2P, 3P, ... loads. Loads due to wind shear, yaw misalignment, tower shadow and large-scale turbulence are in this category.

Periodic loads on blades due to wind shear and yaw misalignment are caused by gradual variation of wind speed in plane of rotation in vertical or lateral plane respectively. They result in a series of 1P and multiples on the blade where 1P loading has much higher amplitude and can be considered the main loading caused by the two sources.

Periodic loads on blades due to tower shadow is caused by sudden wind speed drop in the stagnation region in the shadow of the tower in each rotation for each blade. This results in a series of 1P and multiples on the blade where they have amplitudes of the same order of magnitude.

Periodic loads on blades due to large-scale turbulence is caused by passing of large low-frequency coherent structures on rotor plane. Therefore, the fluctuations in the wind speed result in unsteady periodic loading

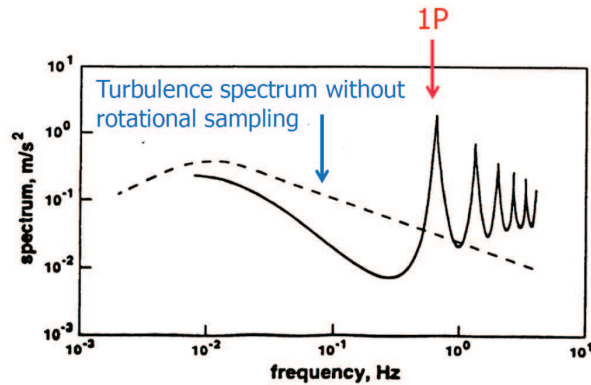


Figure 2.1: Energy spectrum of turbulence and loads due to rotational sampling. [67]

on blades.

Atmospheric turbulence is basically generated as large-scale eddies due to surface roughness or thermal instability. Its energy is transferred to smaller-scale eddies where it finally dissipates into heat. More explanation of turbulence and relevant loads are provided later in this section.

The energy spectrum of turbulence shows the level of energy and related frequency of large and small eddies. Therefore, in each rotation of the blade it may encounter a series of eddies of different size and frequency and they result in loads of different frequency on blades. This is called '*rotational sampling*'. The bigger the eddy is the lower the frequency and the higher amplitude of the load will be. Figure 2.1 shows that 1P loads created by turbulence are of highest amplitude.

Non-periodic random loads are higher-frequency loads mainly due to small-scale turbulence.

The other type of unsteady loads on wind turbines can be a result of thermal instability or gusts. Lee (2012) [44] has reported little significance of thermal stability of atmospheric boundary layer on unsteady loading on wind turbines and consequent fatigue. However, more recent research at TU Delft has found contradicting results which emphasizes the importance of stability of the boundary layer on loads on wind turbine blades.

Another source of high turbulence intensity can be placing wind turbines in the wake of another one. Lee (2012) [44] reported on the significant increase of unsteady loading and fatigue with increase in turbulence intensity as a result of placing wind turbines in the wake of each other.

## 2.2 The main frequency range of unsteady loads

In order to better understand the loads on the wind turbine blades, it is necessary to understand the characteristics of the atmospheric boundary layer. The air velocity near the earth surface is reduced as a result of the friction caused by the surface roughness, i.e. land, trees, buildings, etc. This is while the velocity is higher at higher altitudes. This basically results in two phenomena. Firstly, wind shear which is the vertical velocity variation along the rotation plane as a result of the velocity profile of the atmospheric boundary layer. Secondly, turbulence which is generated by the gradient of velocity normal to the surface.

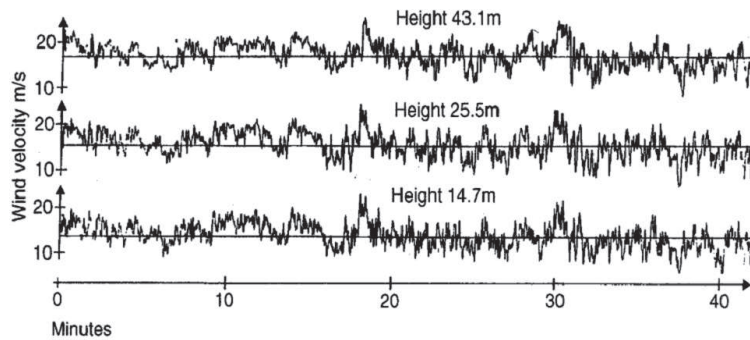


Figure 2.2: Turbulence in neutral condition at different heights. [21]

The velocity profile of the atmospheric boundary layer can be modeled with a logarithmic (or a power) law. The profile is a function of the surface roughness and thermal stability.

Turbulence is a 3D vortex system with results in the local velocity fluctuations. Larger surface roughness results in higher turbulence intensity and more variations in velocity. The length scales of the coherent structures in atmospheric turbulence cover a wide range from centimeters (covering parts of airfoil or smaller) to a few hundred meters (covering parts of rotor plane or larger). The relevant timescales vary from seconds, corresponding to smaller vortices, to minutes, corresponding to larger vortices. Bigger vortex structures have higher levels of energy and can create loads in higher scales but in lower frequencies.

Figure 2.2 shows the wind speed measurements at 3 different heights. The effect of large-scale low-frequency turbulent coherent structures can be clearly seen repeated in the three measurements as they cover the whole area. While, the higher-frequency small-scale fluctuations are distinctive at each height.

The lowest natural frequency in a wind turbine structure is in the range of 0.3-0.5 Hz based on the size of the wind turbine and it corresponds to the tower. Therefore, unsteady loads with lower frequencies, corresponding to meteorological weather events, are not of interest for investigation of resonance on wind turbines. On the other hand, higher frequency dynamic loading will be of particular interest as they might intersect with the natural frequencies of the wind turbine.

Figure 2.3 shows the Campbell diagram of NREL 5MW reference wind turbine. It shows the natural frequencies of components of the wind turbine, including blades, tower and drive train together with the most important periodic dynamic loading frequencies of the wind turbine, i.e. 1P, 2P, 3P, etc.

Figure 2.4 shows the energy spectrum of in-plane and out-of-plane blade root moments of NREL 5MW wind turbine. It shows that the unsteady loads for the 3-bladed wind turbine where highest amplitudes are 1P, 2P and 3P loads and the amplitude reduces with increasing frequency. The load corresponding to 1.1 Hz is the first edgewise moment which is only present in the in-plane moment spectrum. The 2.02 Hz loading corresponds to the second flapwise loading on blades.

Figure 2.4 showed the importance of 1P, 2P and 3P loads for a 3-bladed wind turbine. Understanding from Figure 2.3 and Figure 2.4 shows the importance of unsteady loads with **frequency range 0.1-0.6 Hz** which corresponds to the 1P to 3P loads for the most probable wind speed regime of 8-15 m/s for a wind turbine. These loads can be a result of wind shear, yawed inflow and large-scale low-frequency turbulent coherent structures. The significance of each are to be identified in next section.

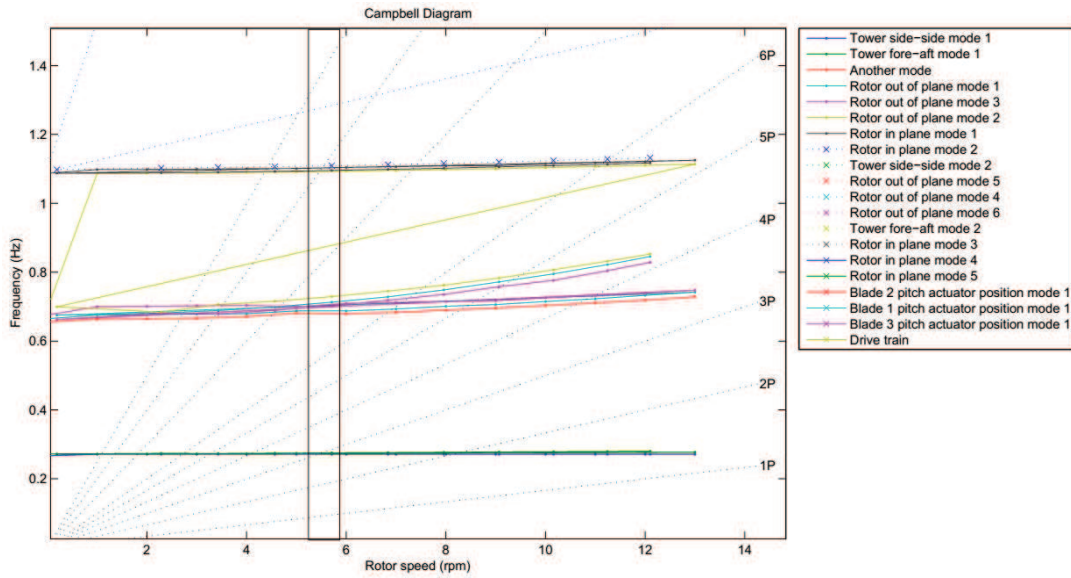


Figure 2.3: Campbell diagram of NREL 5MW reference wind turbine. [36]

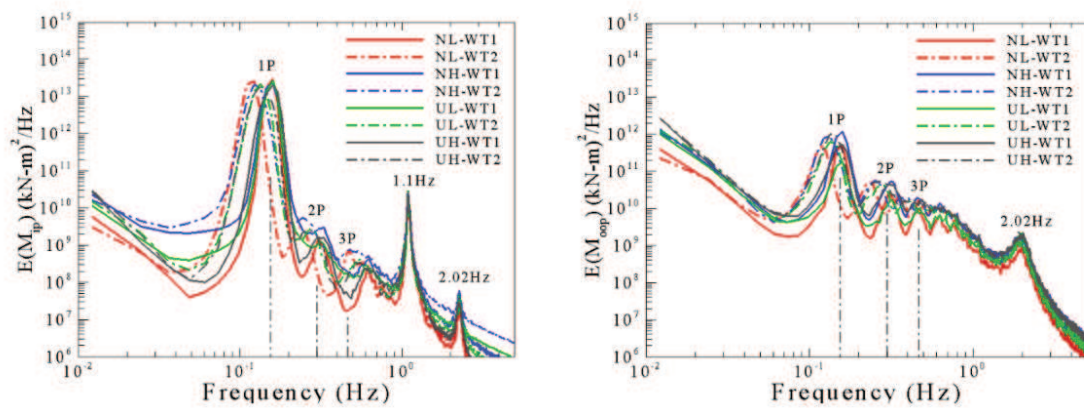


Figure 2.4: Energy spectrum of in-plane -left- and out-of-plane -right- blade root moments of NREL 5MW Reference wind turbine. [44]

## 2.3 HAWC2 simulations

Gravity, aerodynamic imbalance, mass imbalance, tower shadow, wind shear, turbulence and yaw misalignment are the main sources of unsteady loads on wind turbine blades.

In order to identify the effects of these sources of unsteady loading of wind turbines on the spectrum of the blade root bending moment, equivalent fatigue load (EFL) and variations of angle of attack ( $\alpha$ ) and coefficient of lift ( $C_L$ ), a series of 34 aeroelastic simulation cases were carried out using DTU dedicated wind turbine aeroelastic software *HAWC2* developed by DTU Wind Energy at DTU Ris Campus in Roskilde, Denmark '[www.hawc2.dk](http://www.hawc2.dk)'.

Each simulation case itself consisted of 11 individual cases with wind speed from 4 to 24  $m/s$  with steps of 2  $m/s$  which makes 11 different wind speeds between the cut-in and cut-out velocities. Each simulation case has a duration of 1100  $s$ . The last 600  $s$  is the duration where results are captured and it is chosen to comply with the the simulation time prescribed by the design requirements for wind turbines *IEC – 61400 – 1* edition-3 standard [31]. To avoid the initial transient simulation effects, a cut-out time of 500  $s$  has been applied to all the simulation cases at the beginning. The final case (case 34) was with wind steps of 0.5  $m/s$  and covering wind speeds from 3 to 25  $m/s$  which makes 45 individual cases for case 34. The simulation inputs are described in Table 2.1.

**Table 2.1:** Simulation general inputs into HAWC2 and statistics.

Parameter	Value	Unit
Simulation time	1100	s
Cut-out time	500	s
Calculation time	600	s
Wind step	2	$m/s$
Wind speed range	04 – 24	$m/s$
<b>General</b>		
Total No. of cases	408	(33 * 11 + 45)

In total, 408 simulation cases of each 1100s and time step of 0.2s were used for the 34 simulation cases in order to obtain the aforementioned simulation goals.

The simulations were done using reference wind turbine *DTU-10MW-RWT version 3* structural model and controller. The wind model applied used a '*Power law*' with exponential of 0.2 for wind shear, the *Mann* turbulence model to generate turbulent inflow wind and the potential flow model (2nd type available in the software) for the tower shadow. The structural and wind inputs are described in Table 2.2. For details of each model and further explanation, refer to *HAWC2* manual [43].

The aerodynamic model used was the BEM model implemented into *HAWC2* which accounted for tip loss correction, induction correction by Glauret method, yawed inflow wind, dynamic stall correction by MMH Beddoes method (a modified BeddoesLeishman dynamic stall model [45, 51, 30] for wind turbines) and aerodynamic drag for the tower and nacelle. The aerodynamic inputs are described in Table 2.3. For details of each model and further explanation, refer to *HAWC2* manual [43].

The simulation matrix describing the 34 main cases is shown in Table 2.4. The table shows each study focuses on identifying the effect of which sources from tower shadow (TS), wind shear (SH), turbulence intensity (TI) and yawed inflow (Y). The values for the yaw, wind shear and turbulence show the yaw angle ( $deg$ ),

*Table 2.2: Structural and wind inputs into HAWC2.*

Model		
1	Structure	DTU-10MW-RWT
2	Controller	DTU-10MW-RWT
<b>Wind</b>		
1	Wind shear	Power law (Exp=0.2)
2	Turbulence	Mann
3	Tower shadow	Potential flow (2nd type)

*Table 2.3: Aerodynamic inputs into HAWC2.*

Correction	Method	
1	Tip loss	
2	Induction	Glauret
3	Yawed inflow	
4	Dynamic stall	MMH Beddoes
5	Tower drag	
6	Nacelle drag	

wind shear power law exponential and turbulence intensity (%) respectively and a star sign '\*' is used to show the presence of tower shadow in columns. The '†' sign shows that case 34 is the case with wind steps 0.5 m/s and for 3-25 m/s. The value of turbulence intensity is reference turbulence intensity value and the distribution can be calculated based on [31] and the distribution for various wind speeds at hub height is shown in Figure 2.5.

Based on the results of the 34 cases, three separate studies on the blade root bending moment frequency analysis, equivalent fatigue loads and variations of  $\alpha$  and  $C_L$  are provided in the following subsections.

### 2.3.1 Frequency analysis

In this section, we intend to study the main frequencies which cause the unsteady loads with highest amplitudes corresponding to different sources of unsteady loading, i.e. gravitational and imbalance loads, tower

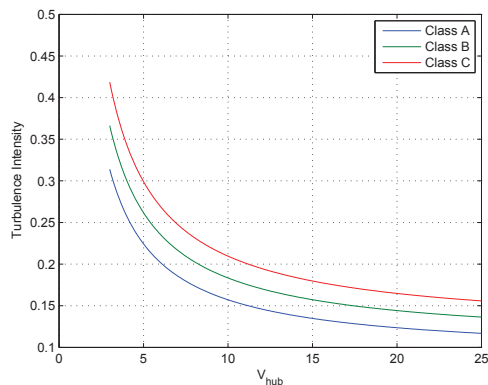
*Figure 2.5: Distribution of turbulence intensity with wind speed at hub height.*

Table 2.4: Description of HAWC2 simulation matrix.

Case	TS	Y	SH	TI	Notes	Case	TS	Y	SH	TI	Notes
<b>1</b>						<b>18</b>	*			16	TS+TI
<b>2</b>		10			Y	<b>19</b>	*			20	TS+TI
<b>3</b>		-10			Y	<b>20</b>	*	10		16	TS+TI+Y
<b>4</b>	*				TS	<b>21</b>	*	-10		16	TS+TI+Y
<b>5</b>			0.2		SH	<b>22</b>		10	0.2		SH+Y
<b>6</b>				4	TI	<b>23</b>		-10	0.2		SH+Y
<b>7</b>				8	TI	<b>24</b>	*		0.2		TS+SH
<b>8</b>				12	TI	<b>25</b>	*	10	0.2		TS+SH+Y
<b>9</b>				16	TI	<b>26</b>	*	-10	0.2		TS+SH+Y
<b>10</b>				20	TI	<b>27</b>	*		0.2	4	TS+SH+TI
<b>11</b>		10		16	TI+Y	<b>28</b>	*		0.2	8	TS+SH+TI
<b>12</b>		-10		16	TI+Y	<b>29</b>	*		0.2	12	TS+SH+TI
<b>13</b>	*	10			TS+Y	<b>30†</b>	*		0.2	16	TS+SH+TI
<b>14</b>	*	-10			TS+Y	<b>31</b>	*		0.2	20	TS+SH+TI
<b>15</b>	*			4	TS+TI	<b>32</b>	*	10	0.2	16	TS+SH+TI+Y
<b>16</b>	*			8	TS+TI	<b>33</b>	*	-10	0.2	16	TS+SH+TI+Y
<b>17</b>	*			12	TS+TI	<b>34††</b>	*		0.2	16	TS+SH+TI

<sup>a</sup> TS: tower shadow, SH: wind shear, Y: yawed inflow, TI: turbulence intensity.

<sup>b</sup> The '†' sign shows the reference case (case 30) where the values of the other cases are compared with. This case contains all the sources of unsteady loads and has a  $I_{ref} = 0.16$  for Class-A.

<sup>c</sup> The '††' sign shows that case 34 is the case with wind steps  $0.5 m/s$  and for  $3-25 m/s$ .

shadow, wind shear, turbulence and yawed inflow.

As already mentioned, the frequency analysis has been conducted on blade root bending moments and the studies are focused on wind speeds of 8, 10 and 12  $m/s$ , i.e. before and after rated speed. However, the results of the study at 12  $m/s$  has been presented unless there is a distinct difference between the two results.

### 2.3.1.1 Gravity, mass and aerodynamic imbalance

The results of the frequency analysis of case 1 show that gravity and imbalances result in a harmonic loading with the frequency of 1P as shown in Figure 2.6. These harmonic loads are a result of harmonic gravitational loads on blades during each rotation, the imbalance in the center of mass of blades with the center of rotation, and the imbalance between the twist and pitch of each blade with respect to others.

### 2.3.1.2 Tower shadow

The results of the frequency analysis of case 4 show that tower shadow results in a non-harmonic periodic loading with the frequency of 1P, 2P, and multiples of 1P which have the same amplitude as shown in Figure 2.7. The tower shadow is a result of sudden drop in wind speed in the stagnation point in front of the tower.

### 2.3.1.3 Wind shear

The results of the frequency analysis of case 5 show that wind shear results in a non-harmonic periodic loading with the main frequency of 1P with the highest amplitude and reducing amplitude for multiples of

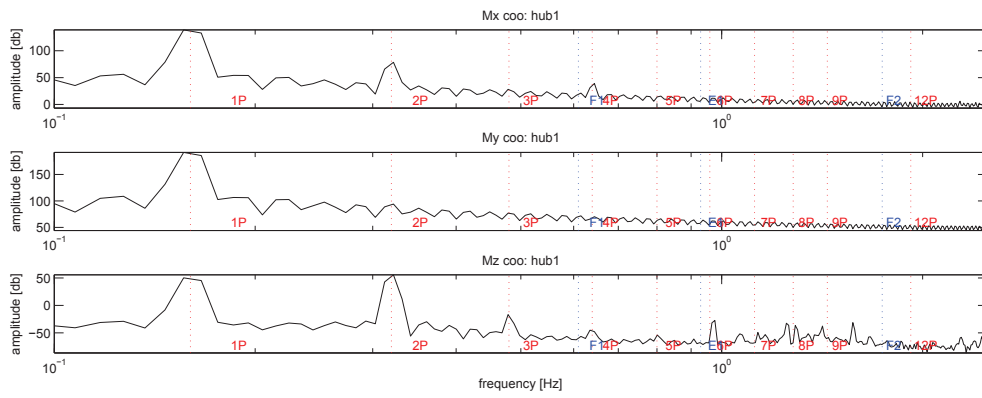


*Figure 2.6: Frequency analysis of unsteady load by gravity and imbalances.*

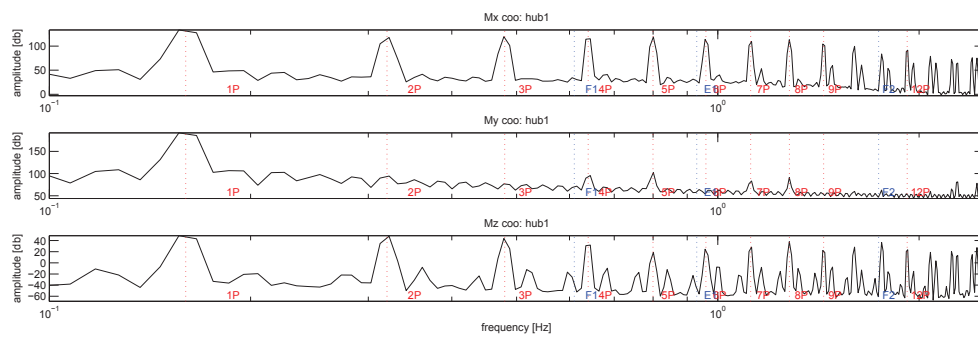


*Figure 2.7: Frequency analysis of unsteady load by tower shadow.*

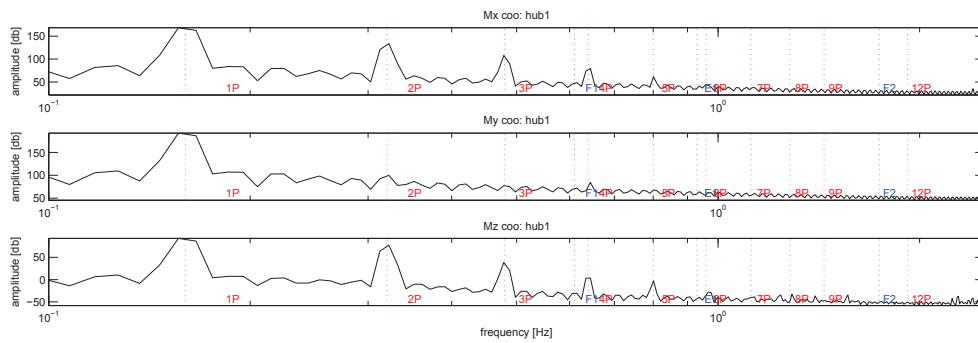


*Figure 2.8: Frequency analysis of unsteady load by wind shear.*

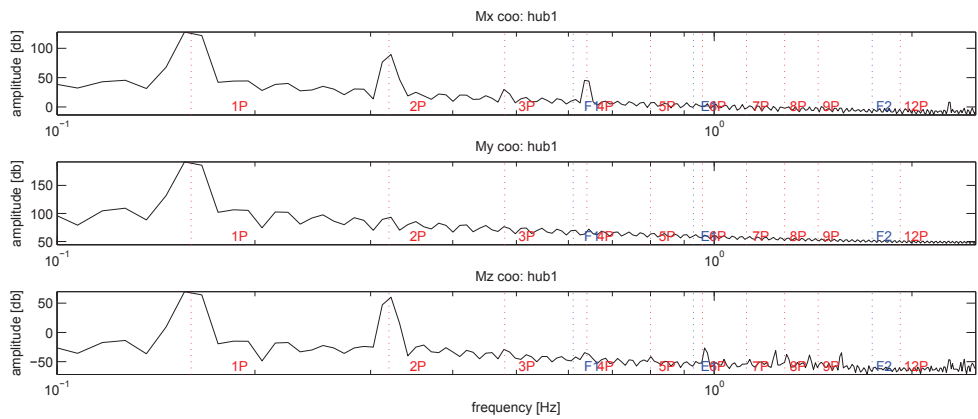


*Figure 2.9: Frequency analysis of unsteady load by yawed inflow.*

1P loading as shown in Figure 2.8. This type of loading is a result of gradual variations of wind speed on rotor plane in vertical direction.

#### 2.3.1.4 Yawed inflow

The results of the frequency analysis of cases 2 and 3 show that yaw angle results in a non-harmonic periodic loading with the main frequency of 1P with the highest amplitude and reducing amplitude for multiples of 1P loading as shown in Figure 2.9. The result is similar to wind shear but in lower amplitudes. This type of unsteady loading is a result of gradual variations of wind speed on rotor plane in lateral direction.

#### 2.3.1.5 Turbulence

The results of the frequency analysis of case 9 shown in Figure 2.10 imply that turbulence results in two kinds of unsteady loading based on the length scale of turbulent coherent structures.

- Non-harmonic periodic loading caused by low-frequency large-scale eddies: It has the highest amplitude at frequency of 1P which can be correlated to eddies with length scale in the order of blade radius. It also has lower amplitude at multiples of 1P.
- Non-periodic random loading caused by high-frequency small-scale eddies: It results in high-frequency low-amplitude loading on blades which does not seem to be a major concern as the amplitudes are very low.

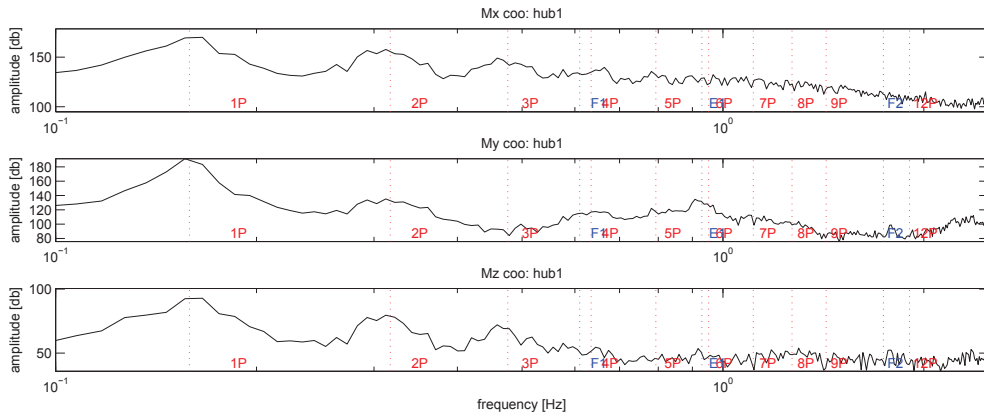


*Figure 2.10: Frequency analysis of unsteady load by turbulence at TI of 0.16.*

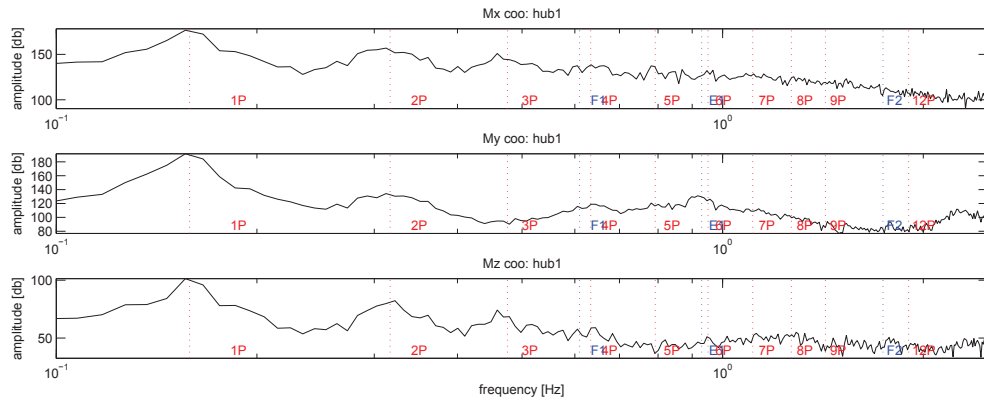


*Figure 2.11: Frequency analysis of unsteady load on blade root bending moment.*

This type of unsteady loading is mainly a result of passing of large-scale turbulent eddies on the rotor plane which results in velocity fluctuations and periodic loads on blades.

### 2.3.1.6 Combined effect

The results of the frequency analysis of case 30 shown in Figure 2.11 illustrate a combined effect of all the unsteady loading sources similar to a real case for a wind turbine. It has amplitude peaks at 1P and multiples of 1P with the highest peak at 1P as the main frequency for unsteady loading of wind turbine.

This frequency is the main target for any type of unsteady load control on wind turbines as it has the highest amplitudes and mitigation of this loading will have the greatest impact on wind turbine.

## 2.3.2 Fatigue analysis

The second study was analysis of equivalent fatigue loads. Each equivalent fatigue load was calculated for each case with 11 time series (wind speed increasing from 4 to 24 m/s with steps of 2 m/s) of 600s with different turbulence seeds. The IEC-61400-1 edition-3 standard [31] Annex G is the reference where the calculation of fatigue loads for normal turbulence model (NTM) are based on. The reference value of

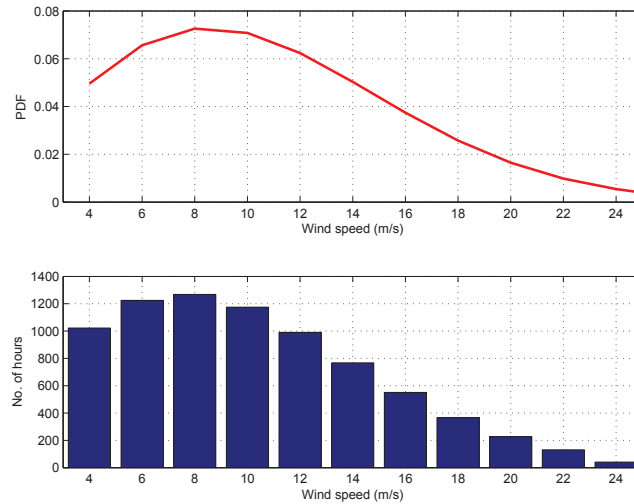


Figure 2.12: Weibull distribution with  $k = 2.03$  and  $A = 11.9$  utilized for fatigue calculation.

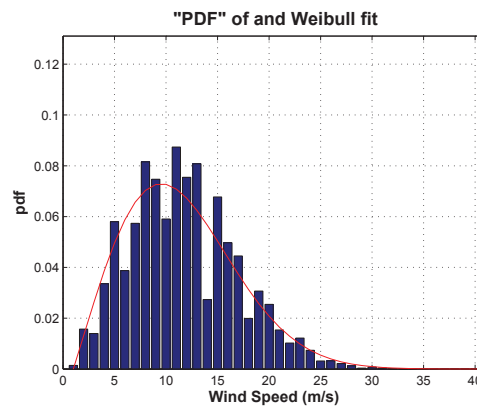


Figure 2.13: PDF and Weibull distribution fitted to the wind data from the mast.

turbulence intensity is 0.16 based on 'Class-A' for wind turbines.

The Weibull distribution used to determine the annual number of hours for each wind speed and the corresponding load time series used for the fatigue calculations has a shape factor ( $k$ ) of 2.03 and a scale factor ( $A$ ) of 11.9 and is shown in Figure 2.12. The Weibull distribution was fitted to 23 years of wind data with one measurement per hour and a return rate of 91.5% taken from the off-shore 10m-height meteorological mast at station 321 Europlatform provided by Koninklijk Nederlands Meteorologisch Instituut (KNMI) in the Netherlands which was scaled up to the DTU-10MW-RWT hub height (119 m) using logarithmic law. The station is located 40km away from the Dutch coast at 51.999 latitude and 3.276 longitude. The probability density function (PDF) and fitted Weibull distribution to wind data are shown in Figure 2.13.

Lifetime Equivalent Fatigue Load (LEFL) of a wind turbine corresponds to  $10^7$  cycles which is equal to 20 years of operation and for calculation of each case the whole range of wind speed (4 – 24 m/s) and the aforementioned Weibull distribution has been considered. LEFL was calculated based on Palmgren-Miner's summation rule as detailed in [64].

The LEFL for blade root bending moment around the three axes (Mx [flapwise], My [edgewise], Mz [torsion])

for the 34 cases are summarized in Table 2.5 and the normalized values with the reference case are plotted in Figure 2.14. The results will be categorized based on the load source and compared later in this section.

**Table 2.5:** Lifetime equivalent fatigue loads (LEFL) for 34 various unsteady loading cases.

Case	Mx	My	Mz	Notes	Case	Mx	My	Mz	Notes
	LEFL (KNm)					LEFL (KNm)			
<b>1</b>	4339	19461	161		<b>18</b>	22235	22455	363	TS+TI16
<b>2</b>	2602	20223	202	Y	<b>19</b>	27002	23733	476	TS+TI20
<b>3</b>	4939	19365	162	Y	<b>20</b>	22516	22480	355	TS+TI16+Y
<b>4</b>	4404	19590	161	TS	<b>21</b>	21970	21882	326	TS+TI16+Y
<b>5</b>	7122	20066	172	SH	<b>22</b>	9614	20223	202	SH+Y
<b>6</b>	6232	19650	167	TI4	<b>23</b>	5427	19942	165	SH+Y
<b>7</b>	11842	20238	202	TI8	<b>24</b>	8284	20116	172	TS+SH
<b>8</b>	17010	21156	268	TI12	<b>25</b>	10888	20304	202	TS+SH+Y
<b>9</b>	22295	22401	358	TI16	<b>26</b>	6609	19967	165	TS+SH+Y
<b>10</b>	27248	23637	463	TI20	<b>27</b>	10504	20405	191	TS+SH+TI4
<b>11</b>	22328	22363	353	TI16+Y	<b>28</b>	14732	21068	235	TS+SH+TI8
<b>12</b>	22020	21846	327	TI16+Y	<b>29</b>	19465	22065	295	TS+SH+TI12
<b>13</b>	4210	19539	165	TS+Y	<b>30</b>	24191	23377	370	TS+SH+TI16
<b>14</b>	5373	19409	162	TS+Y	<b>31</b>	28418	24645	433	TS+SH+TI20
<b>15</b>	6264	19719	167	TS+TI4	<b>32</b>	24807	23561	391	TS+SH+TI16+Y
<b>16</b>	11737	20312	203	TS+TI8	<b>33</b>	23014	22664	337	TS+SH+TI16+Y
<b>17</b>	17037	21225	268	TS+TI12	<b>34</b>	24844	23474	380	TS+SH+TI16

<sup>a</sup> TS: tower shadow, SH: wind shear, Y: yawed inflow, TI: turbulence intensity and the values corresponding to its percentage.

### 2.3.2.1 Gravity, mass and aerodynamic imbalance

The value of LEFL corresponding to unsteady gravitational loads and unsteady loads due to mass imbalance (as a result of location of center of mass of blades off the center of rotation) and aerodynamic imbalance (as a result of twist and pitch difference between blades) are studied in Case 1.

A first impression from the Figure 2.14 is that the LEFL due to blade root edgewise moment (My) is almost constant for all the various 34 loading cases. It simply shows that this LEFL is mainly caused by unsteady loads due to gravity and imbalance and almost up to about 85% independent of the wind conditions.

On the other hand, only about 18% of the LEFL caused by the blade root flapwise bending moment is a result of unsteady loads due to gravity and imbalance and it is more than 80% dependent on wind conditions.

The LEFL value caused by torsion (Mz) is very small compared to the same value for Mx and My, therefore, its contribution to the blade fatigue is negligible. Thus, the behavior of the values corresponding to Mz will not be discussed and the values will only be presented and plotted. It is good to note that about 50% of the total LEFL due to Mz is caused by gravity and imbalance.

The distribution of fatigue damage caused by gravity and imbalance versus wind speed and LEFL values for Mx, My and Mz are shown in Figure 2.15. It is seen that in this case the edgewise fatigue damage does not change significantly over the wind speed. As already discussed it is almost independent of wind conditions. A gradual increase in flapwise fatigue damage caused gravity and imbalances over the wind speed is observed.

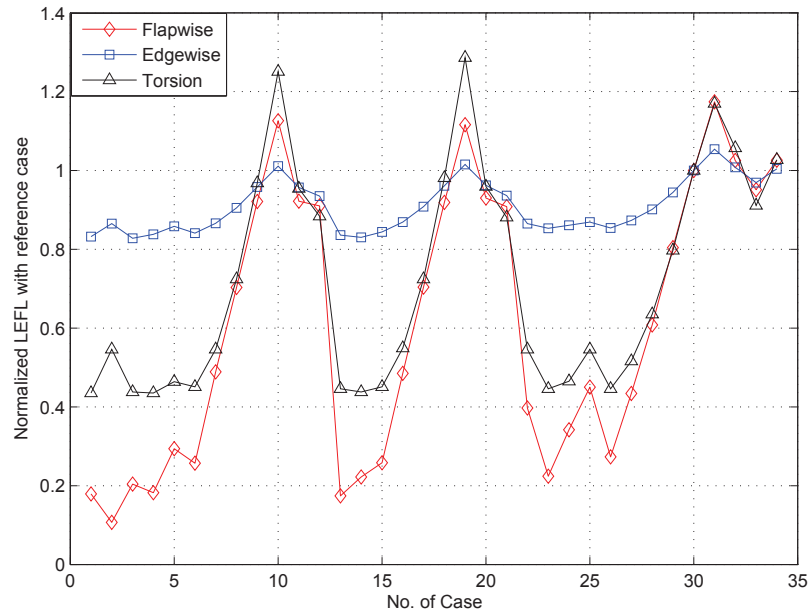


Figure 2.14: Normalized LEFL values with the reference case.

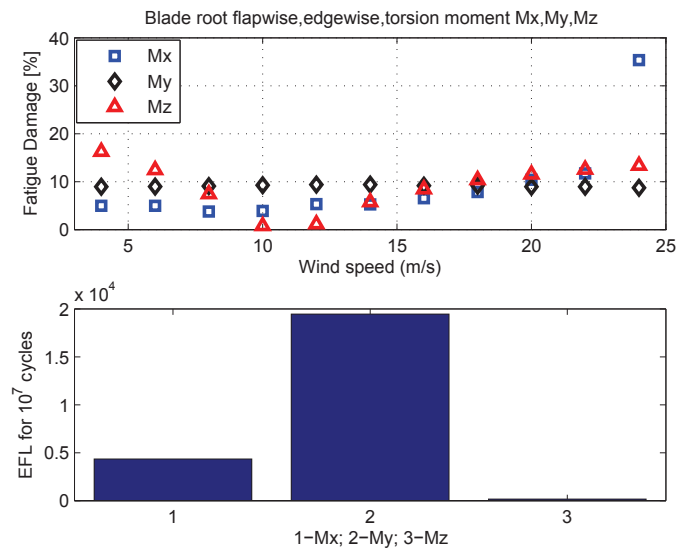
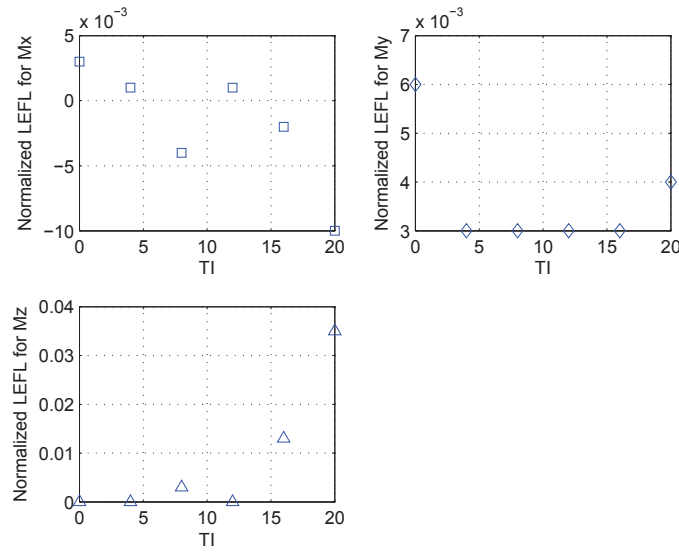


Figure 2.15: Fatigue damage distribution vs. wind speed and LEFL values for case 1.



*Figure 2.16: Normalized LEFL values with the reference case for various TI as a result of tower shadow.*

### 2.3.2.2 Tower shadow

The comparison of the results from cases 1,4 with the reference case show that tower shadow can increase the flapwise LEFL by 0.3% and the edgewise LEFL by 0.6% in the absence of turbulence. The effect of tower shadow in the presence of turbulence is shown in Figure 2.16. It shows that the effect of tower shadow in the presence of turbulence is still negligible and stays between  $\pm 0.3\%$  for flapwise LEFL and is 0.3% for edgewise LEFL up to TI of 16%.

Figure 2.17 shows the fatigue damage distribution caused by a combination of gravity, imbalances and tower shadow versus wind speed and a comparison of LEFL values for Mx, My and Mz. It is seen that tower shadow does not change the fatigue damage distribution.

### 2.3.2.3 Wind shear

The comparison of the results from cases 1 and 5 with the reference case show that wind shear can increase the flapwise LEFL by about 12% and the edgewise LEFL by about 2% in the absence of turbulence. The effect of wind shear in the presence of turbulence is shown in Figure 2.18. It shows that the effect of wind shear in the presence of turbulence decreases from 16% to 8% with increasing TI from 0% to 16% for flapwise LEFL and increases from about 2% to about 4%.

Figure 2.19 shows the fatigue damage distribution caused by a combination of gravity, imbalances and wind shear versus wind speed and a comparison of LEFL values for Mx, My and Mz. It is seen that wind shear does not change the edgewise fatigue damage distribution. However, it strongly affects the slope of the flapwise fatigue damage and results in a sharper increase in fatigue damage as wind speed increases. The increase in the amount of flapwise LEFL due to wind shear is also observed.

### 2.3.2.4 Turbulence

The results from cases 1,6-10 and 4,15-19 and 24,27-31 shown in Figure 2.20 imply almost a linear increase in normalized LEFL (with the reference case) due to Mx, My and Mz.

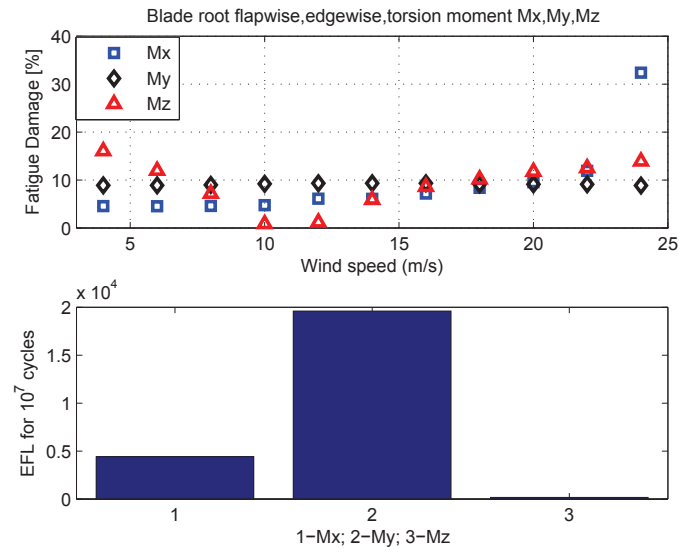


Figure 2.17: Fatigue damage distribution vs. wind speed and LEFL values for case 4.

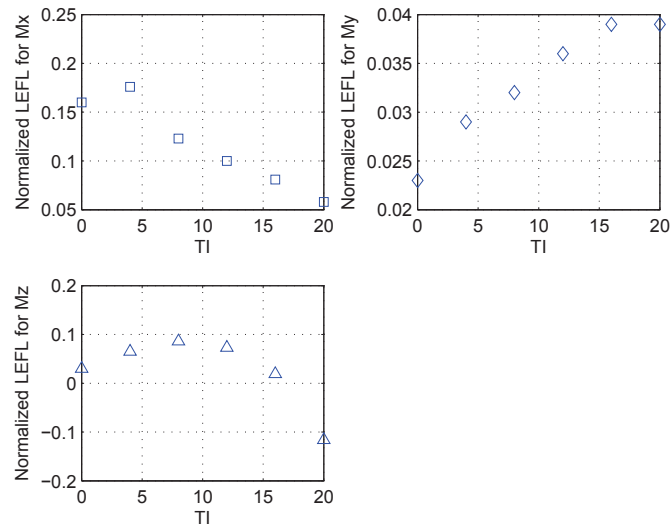
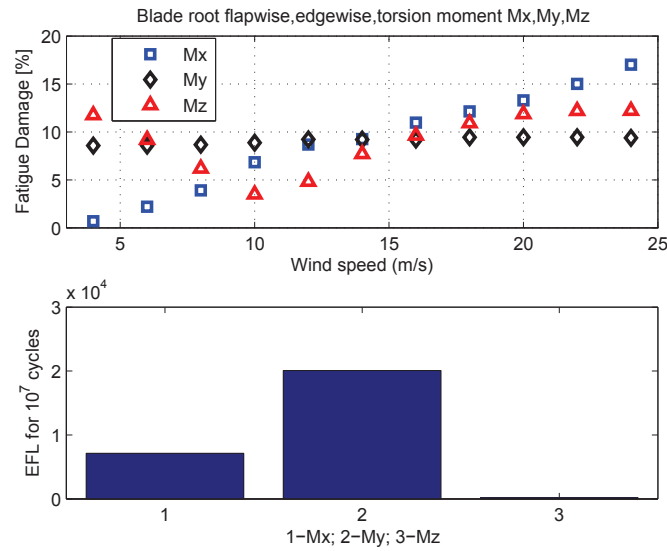


Figure 2.18: Normalized LEFL values with the reference case for various TI as a result of wind shear.



*Figure 2.19: Fatigue damage distribution vs. wind speed and LEFL values for case 5.*

The results show that when TI increases from 0% to 16%, the normalized flapwise LEFL increase from 0.34 to 1.00 which shows an increase of 65.8% of the maximum. The comparison clearly implies that about 66% of flapwise LEFL is caused by the turbulence at the reference TI and the other 34% is a result of a combination of gravity, mass and aerodynamic imbalance, tower shadow and wind shear.

The increase in the edgewise LEFL due to the same value of turbulence is only about 14% of the maximum. This again expresses the low impact of wind conditions for edgewise LEFL and the great impact of gravity and imbalances which contribute to over 86% of the fatigue.

Figure 2.21 shows the fatigue damage distribution caused by a combination of gravity, imbalances and turbulence versus wind speed and a comparison of LEFL values for Mx, My and Mz. It is seen that turbulence slightly changes the distribution for flapwise fatigue damage and causes more damage at higher wind speeds. It also induces a low slope for the edgewise fatigue damage and results in slightly higher damage at higher wind speeds.

The massive leap in the amount of flapwise LEFL due to turbulence is obvious in Figure 2.21. It is seen that TI of 16% causes the flapwise and edgewise LEFL to become in the same order. Turbulence causes the flapwise fatigue damage as much as the combination of gravity and imbalances result in edgewise fatigue damage.

Figure 2.22 shows the fatigue damage distribution for the reference case which is a representative of a real case with all unsteady load sources (except yaw) for a 'Class-A' wind turbine caused by a combination of gravity, imbalances, tower shadow, wind shear and turbulence (TI of 16%) versus wind speed and a comparison of LEFL values for Mx, My and Mz.

Regarding the flapwise LEFL, an important understanding is that firstly wind shear and secondly turbulence play the most important role in the *slope* of the fatigue damage and is the main cause for having higher damage at higher wind speeds. The *magnitude* of flapwise LEFL is firstly a result of turbulence, secondly gravity and imbalances and thirdly wind shear.

The case is different for the edgewise LEFL where the magnitude of LEFL is mainly caused by gravity and imbalances while the slow slope is caused by the turbulence.

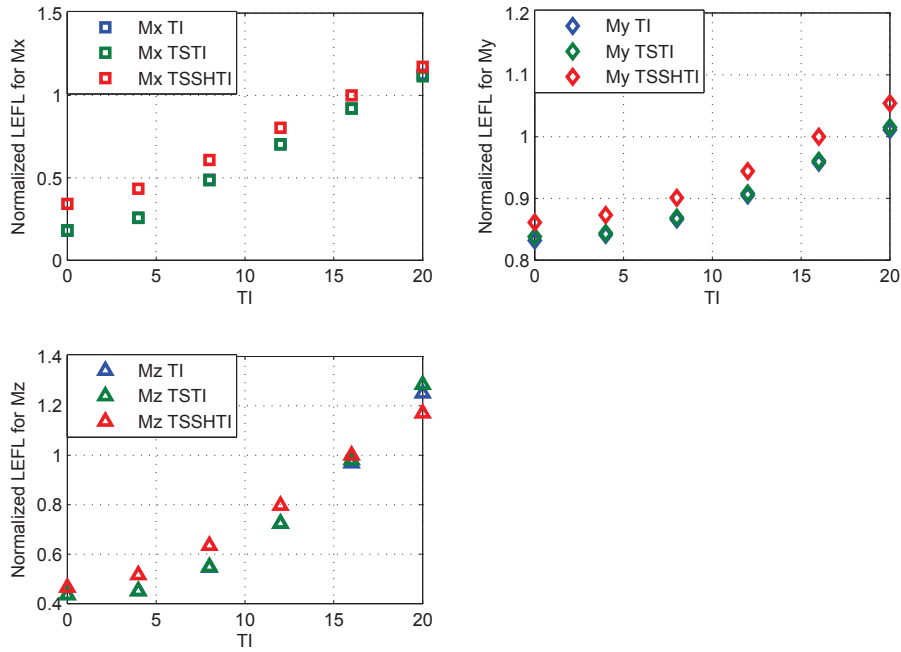


Figure 2.20: Normalized LEFL values with the reference case for various TI.

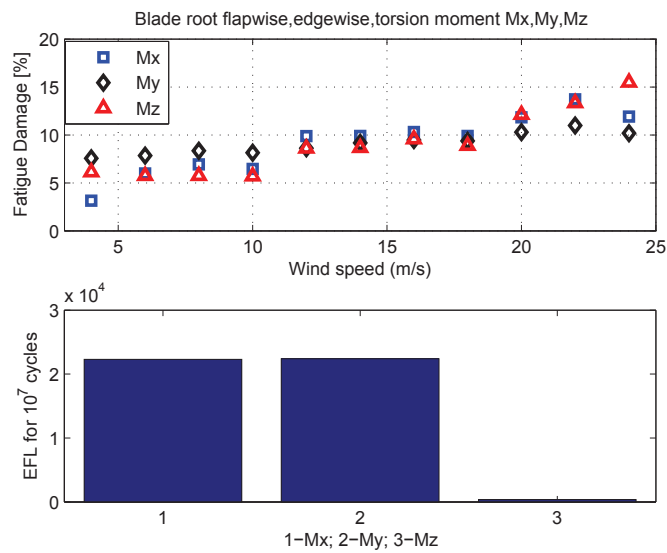


Figure 2.21: Fatigue damage distribution vs. wind speed and LEFL values for case 9.

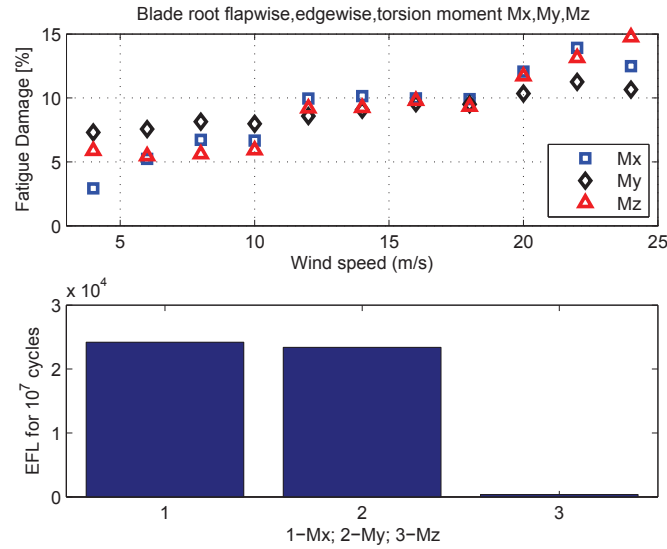


Figure 2.22: Fatigue damage distribution vs. wind speed and LEFL values for case 30.

### 2.3.2.5 Yawed inflow

The results of simulation were used to investigate the effect of yaw angle on the fatigue loads. The main understanding implies that yaw angle of  $+10$  can increase the fatigue loads up to 2.5% for flapwise and up to 0.8% for edgewise LEFL when compared to a zero yaw angle while yaw angle of  $-10$  can decrease the flapwise LEFL up to 5% and edgewise LEFL up to 3%. The results are based on adding the yaw angles to the reference case which has a TI of 16%.

Figure 2.23 and Figure 2.24 show the effect of yaw angle for various unsteady loading cases in the absence and presence of turbulence. The cases are shown in two different figures as presence of turbulence changes the magnitude of LEFL and therefore it is hard to have a focus on both ranges to show the effect of yaw angle. It can be seen that the presence of wind shear has a prominent effect on the resultant effect of yaw angle on fatigue loads. Wind shear results in a reduction in fatigue loads for negative yaw angles and an increase in fatigue loads for positive yaw angles. The case is different in the absence of wind shear.

Figure 2.25 and Figure 2.26 show how yaw angles of  $+10deg$  and  $-10deg$  can change the fatigue damage distribution compared to the reference case. It can be seen that yawed inflow does not have a significant influence on the fatigue damage distribution of the reference case.

### 2.3.2.6 Overall contribution

Based on the results of the 34 cases and the individual effect of each source of unsteady loading already studied, an approximate quantification of the contribution of each unsteady load source on fatigue loads has been carried out for the studied case and is summarized in Table 2.6 and illustrated in Figure 2.27 to Figure 2.29 for Mx, My and Mz.

Figure 2.27 elucidates the main contribution of turbulence for flapwise LEFL while gravity, imbalances and wind shear are the other prominent effects. From the comparison of results it was understood that the flapwise LEFL caused by aerodynamic imbalance (pitch and twist off-set of the blades) increase by 8% when

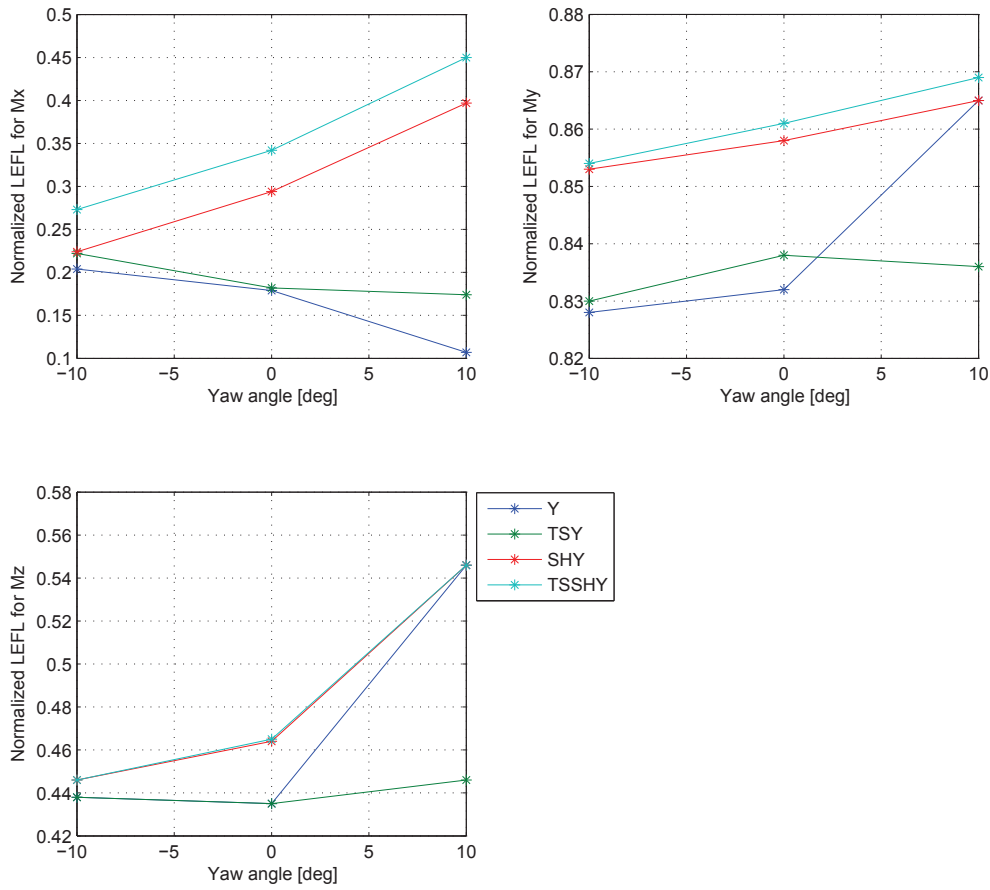


Figure 2.23: Normalized LEFL values with the reference case for various Yaw angles in the absence of turbulence.

Table 2.6: Contributions (%) to total LEFL.

Source	Mx	My	Mz
Gravity and imbalance	17.9	81.8	43.5
Ower shadow	0.2	0.3	1.5
Wind shear	8.1	3.9	1.9
Turbulence (TI=0.16)	65.8	14	53.1
Added Aero-Imb by TI	8		
SUM	100	100	100
<b>YAW</b>			
yaw +10	2.5	0.8	5.7
yaw-10	-5	-3	-8.9

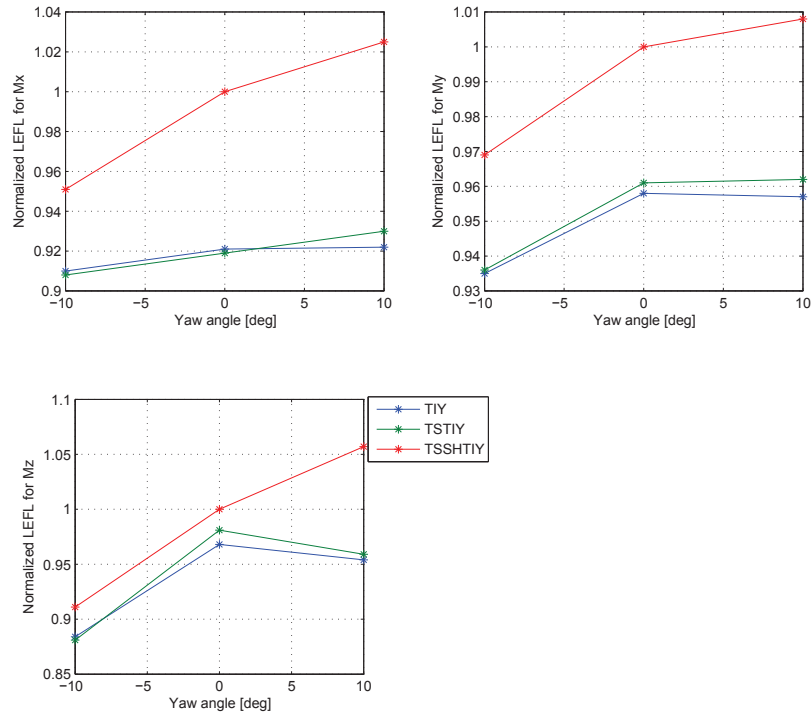


Figure 2.24: Normalized LEFL values with the reference case for various Yaw angles in the presence of turbulence.

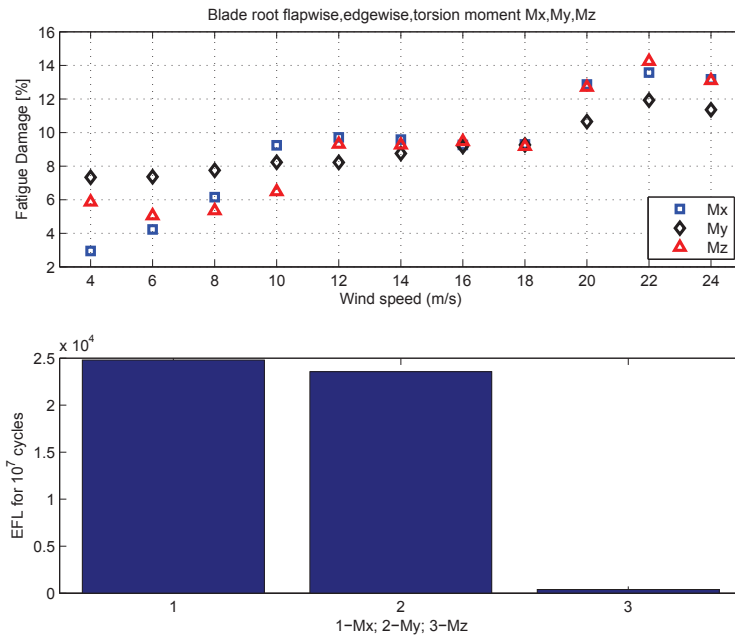


Figure 2.25: Fatigue damage distribution vs. wind speed and LEFL values for case 32.

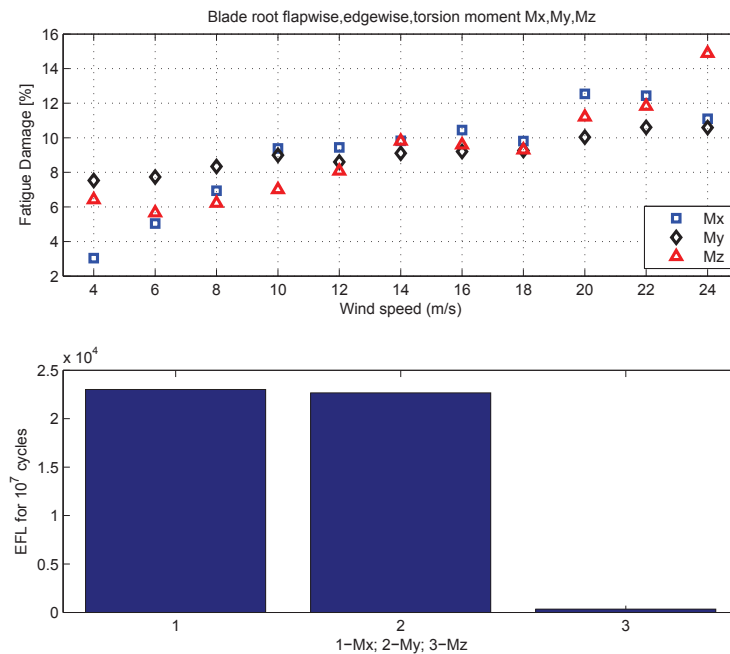


Figure 2.26: Fatigue damage distribution vs. wind speed and LEFL values for case 33.

the turbulence intensity increases to 16%.

Figure 2.28 clearly shows the main contribution of gravitational loads for edgewise LEFL while turbulence has a second role with wind shear as a third effect.

### 2.3.3 Influence on angle of attack and variations of lift

A study is conducted based on the results of the *HAWC2* simulations as listed in Table 2.4 to elucidate the effect of the wind turbine unsteady loading on variations of  $\alpha$  and  $C_L$  in the rotor plane for various wind speeds.

The study has excluded the root sections with  $\frac{r}{R} < 0.2$  as the sections where close to cylindrical shape and a correlation with polars was not conclusive.

As the wind turbine used in the simulations is the *DTU-10MW-RWT*, it is first required to know the airfoils and their design characteristics in order to better understand the operating conditions based on the angle of attack for different radial positions. Therefore, the relevant data are provided in Table 2.7.

The polars of the airfoils and the distribution of their design values are illustrated in Figure 2.30 and Figure 2.31.

At the first step, the variations of the angle of attack for the reference case, which is a representative of a real case for a wind turbine including gravity, mass and aerodynamic imbalances, turbulence, wind shear

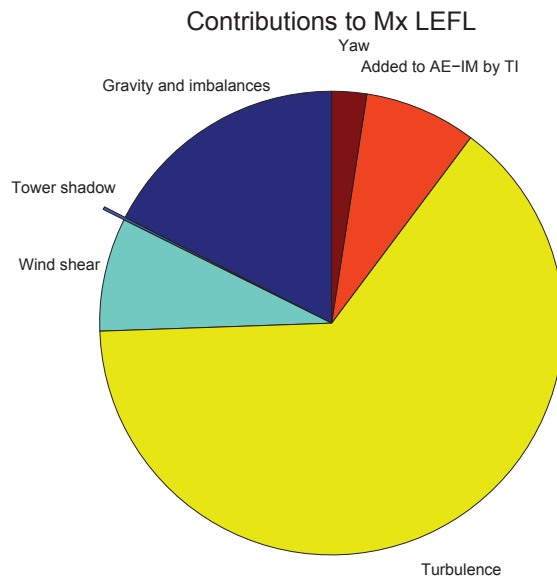


Figure 2.27: Contributions of unsteady loads to overall Mx (flapwise) LEFL.

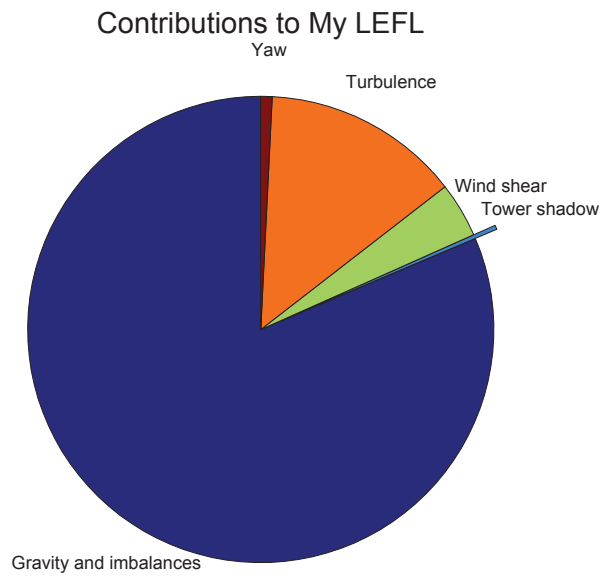
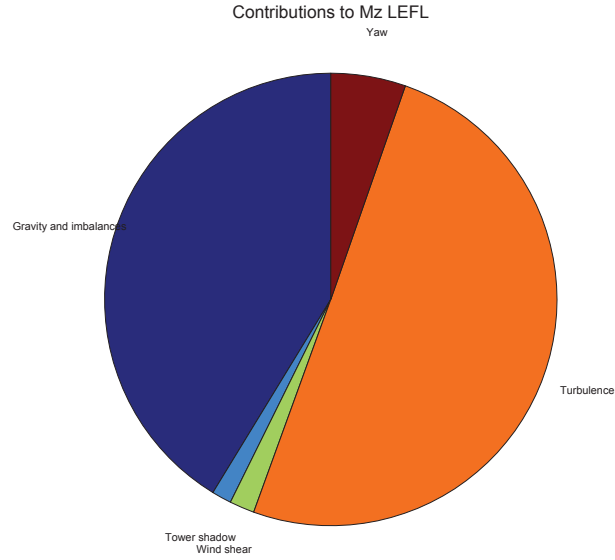


Figure 2.28: Contributions of unsteady loads to overall My (edgewise) LEFL.



**Figure 2.29:** Contributions of unsteady loads to overall Mz LEFL.

**Table 2.7:** DTU-10MW-RWT airfoils and design values.

Airfoils	$(\frac{t}{c})_{Max}$	$\alpha_{des}$	$C_{L,des}$	$C_{L,Max}$	$\alpha_{CL,Max}$	$C_{D,des}$	$(\frac{C_L}{C_D})_{des}$	$\frac{r}{R}$	R (m)
FFA-W3-600	0.6	16 [deg]	1.42	1.82	20	0.15	9.47	0.05-0.16	$5 < R < 16$
FFA-W3-480	0.48	4	0.87	1.80	7	0.034	25.56	0.16-0.25	$16 < R < 24$
FFA-W3-360	0.36	6.58	1.45	1.85	12	0.024	60.78	0.25-0.34	$24 < R < 30$
FFA-W3-301	0.301	8	1.28	1.73	14	0.015	84.69	0.34-0.6	$30 < R < 54$
FFA-W3-241	0.241	9.16	1.41	1.81	16	0.014	98.18	0.6-1	$54 < R < 89$

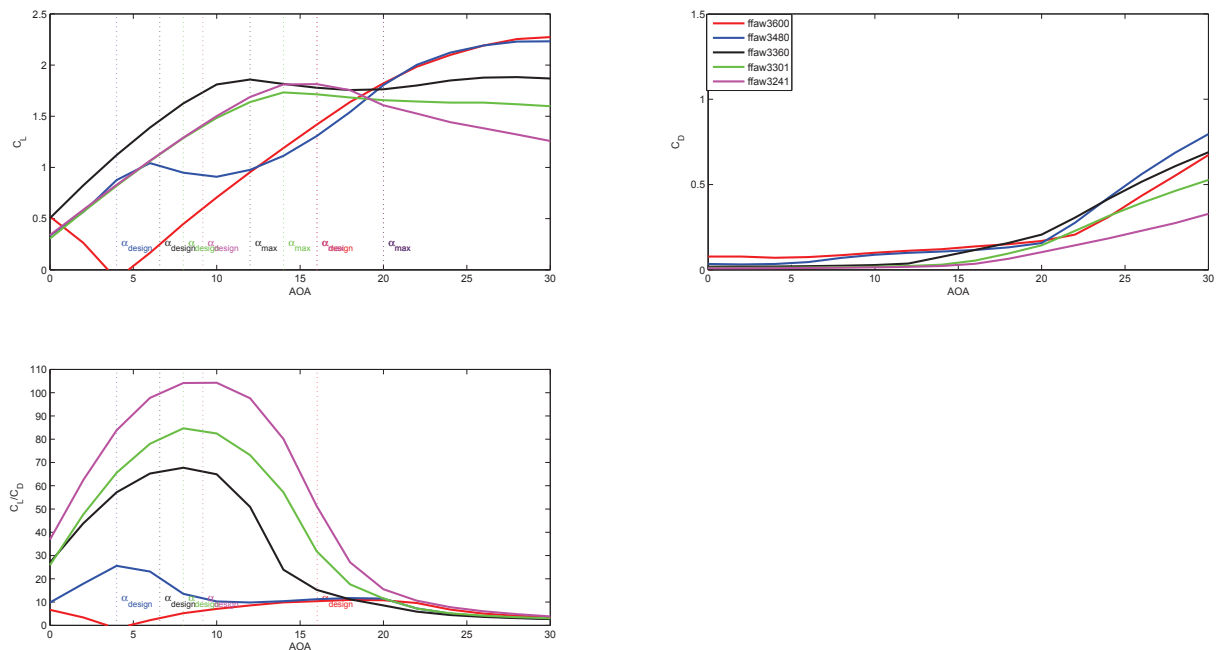


Figure 2.30: DTU-10MW-RWT airfoils' polars.

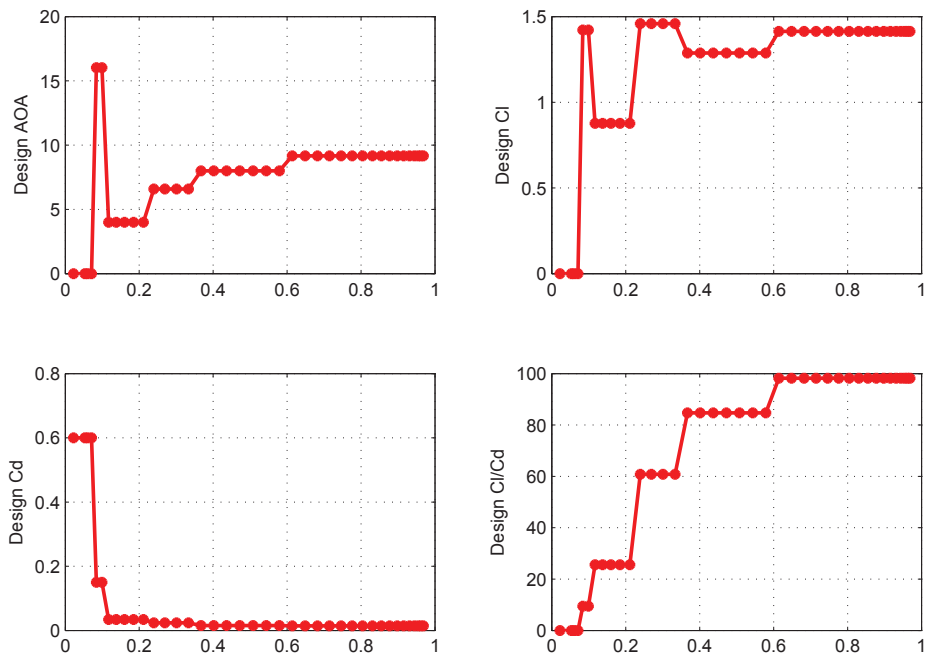
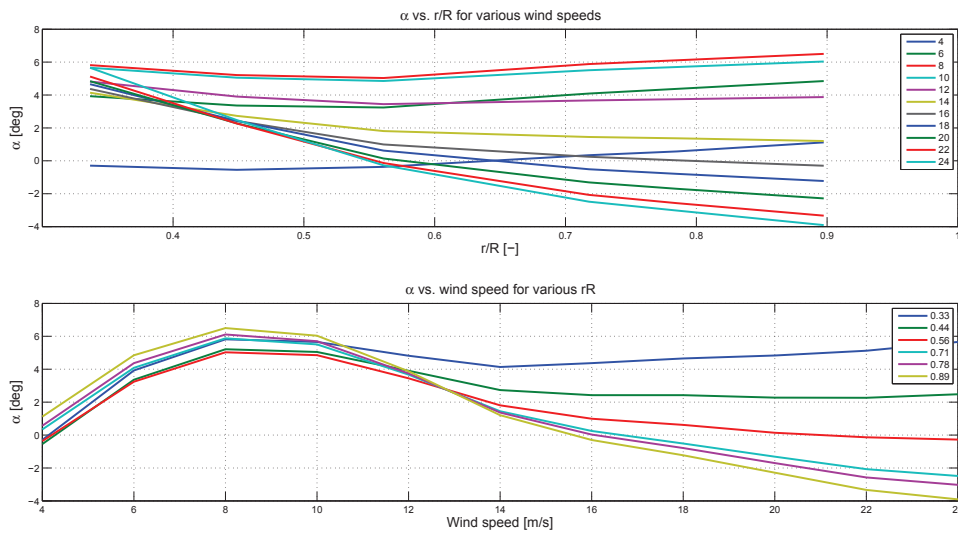


Figure 2.31: DTU-10MW-RWT airfoils' design values.



**Figure 2.32:** Variations of  $\alpha$  vs. radial position and wind speed for the reference case.

and tower shadow, is used to identify the wind speed where the highest angle of attack is experienced for the most parts of the blade.

The results plotted in Figure 2.32 shows that the highest  $\alpha$  for *DTU-10MW-RWT* and for the reference case happens at about 8 m/s. This velocity is slightly before the rated wind speed of the turbine (11.4 m/s).

This study has been conducted for different unsteady loading cases and similar result was observed. Therefore, the focus of the study has been set at results at 8 m/s where the highest angles of attack are experienced on the blade.

Apart from the variations of the mean value of the angle of attack and lift coefficient, the fluctuations of the two are of more importance as they are the main sources of unsteady loading on blades. Therefore, The variations of  $\alpha$  and  $C_L$  with shaded standard deviations versus radial position at 8 m/s for the reference case are shown in Figure 2.33.

This is while the mean values has a small drop in the midspan with slightly higher values at the tip. This is good to note that the root regions of  $\frac{r}{R} < 0.2$  are excluded in the study.

The result shows that there is almost a uniform level of fluctuations of angle of attack along the blade with slightly higher fluctuations near the root. Similar behavior is observed for  $C_L$ . The variations of  $\alpha$  start from  $\pm 4$  near the root and decrease to  $\pm 2$  near tip. This corresponds to approximately a  $\Delta C_L = \pm 0.25$  along the entire blade which results in wide range of variations in lift.

In order to know the position of the operating angles of attack versus the corresponding airfoils for the section and in order to understand the sections that experience stall during the operation at 8 m/s, the angle of attack values are plotted against the polars in Figure 2.34.

The figures show that sections from midspan to tip never experience stall during operation while sections with  $\frac{r}{R} < 0.35$  happen to operate in stall mode.

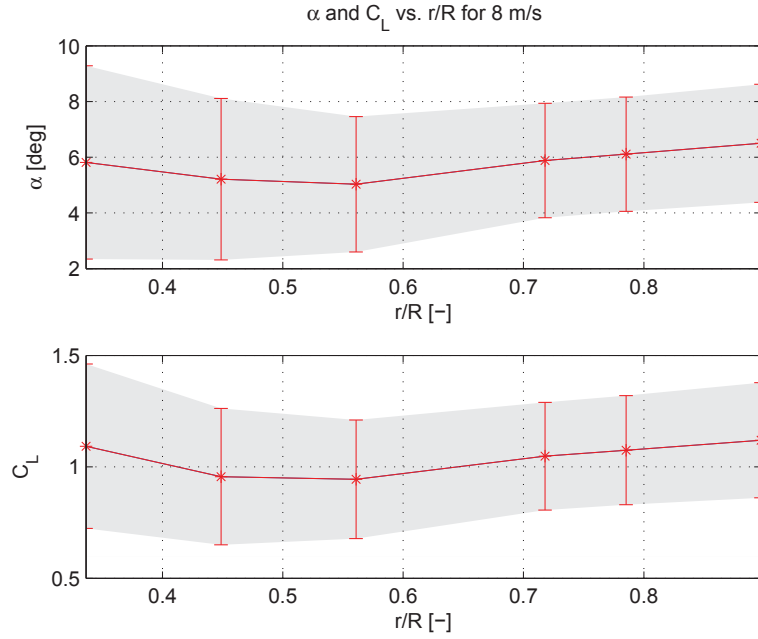


*Figure 2.33: Variations of  $\alpha$  and  $C_L$  with shaded standard deviations vs. radial position at 8m/s for the reference case.*

The variations of  $\alpha$  versus azimuth for  $R = 80m$  is plotted in Figure 2.35 to give an overview of the variations in blade rotations.

Knowing the different behavior of the mean and fluctuations of  $\alpha$  and  $C_L$ , the values for various unsteady loadings are compared in order to identify the effect of the sources.

Figure 2.36 shows the variations of mean values of  $\alpha$  and  $C_L$  for various unsteady loading cases where the 'Clean' case has only gravity and imbalances as the sources of unsteady loading but no tower shadow, no wind shear, no yaw and no turbulence and the other cases are compared to correspondingly to identify the effects.

It shows that almost all the unsteady load sources reduce the mean value of  $\alpha$  and  $C_L$  along the blade. The reduction is to a greater amount from midspan to tip while small to negligible reduction is seen near the root.

The case is totally different for the fluctuations of  $\alpha$  and  $C_L$  shown in Figure 2.37 where all the unsteady load sources increase the fluctuations of  $\alpha$  to various amounts. The values are normalized with the relevant values for the 'Clean' case to make the increments more self-explaining. The normalized values are shown in Figure 2.38.

The result is described as below:

- Tower shadow has a negligible effect on the fluctuations.
- Yaw increases the fluctuations by a factor of 2 almost uniformly along the span.
- Wind shear increases the fluctuations by a factor of 2 near the root. This factor increases almost linearly to 4 for  $\frac{r}{R} = 0.3 - 0.7$  and stays constant outwards to tip.

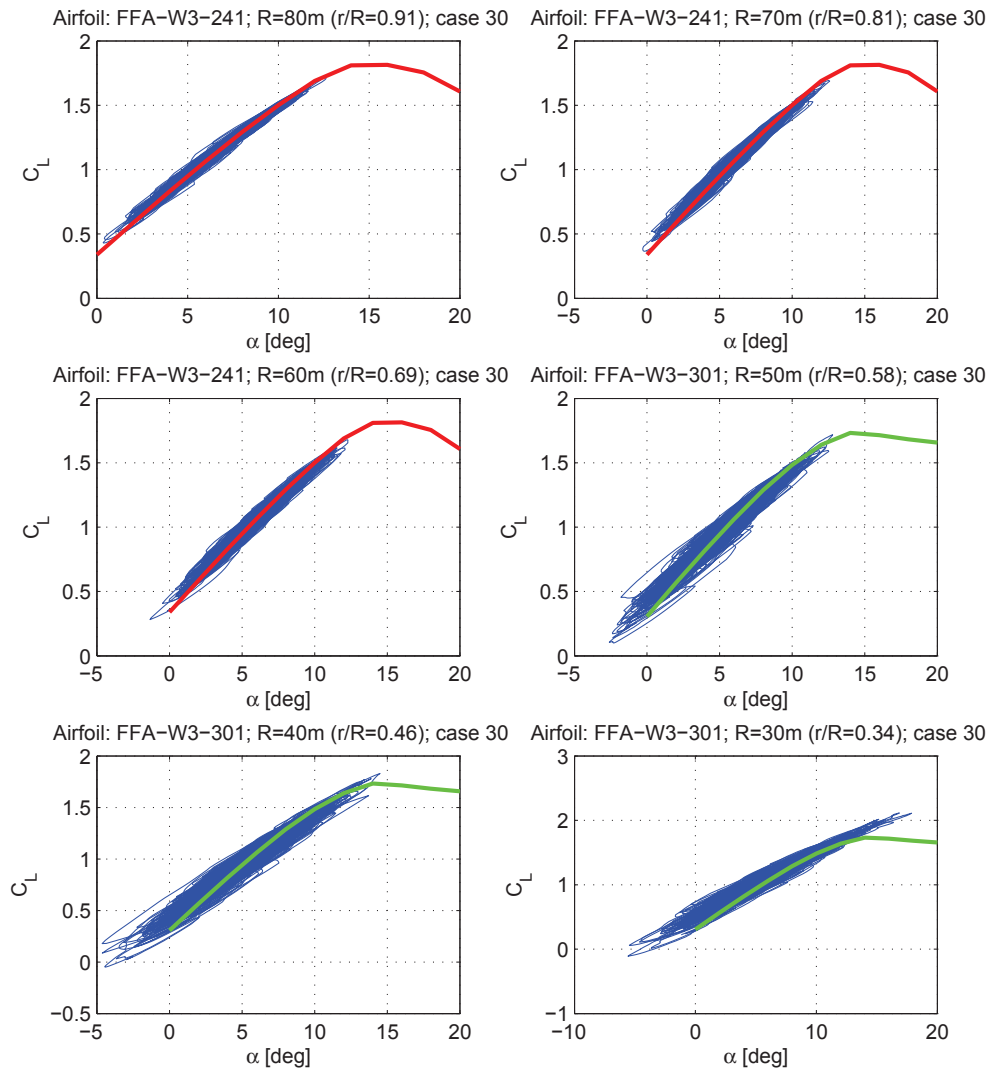
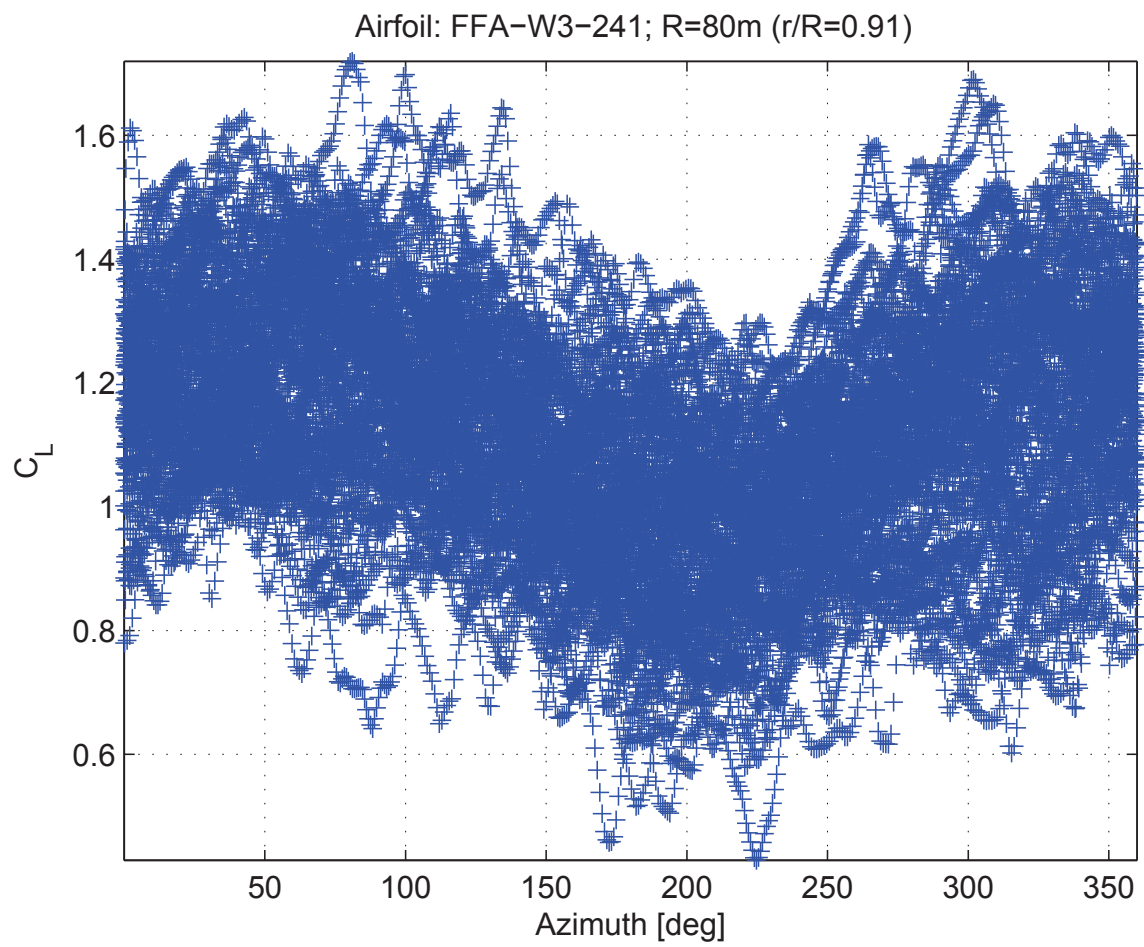
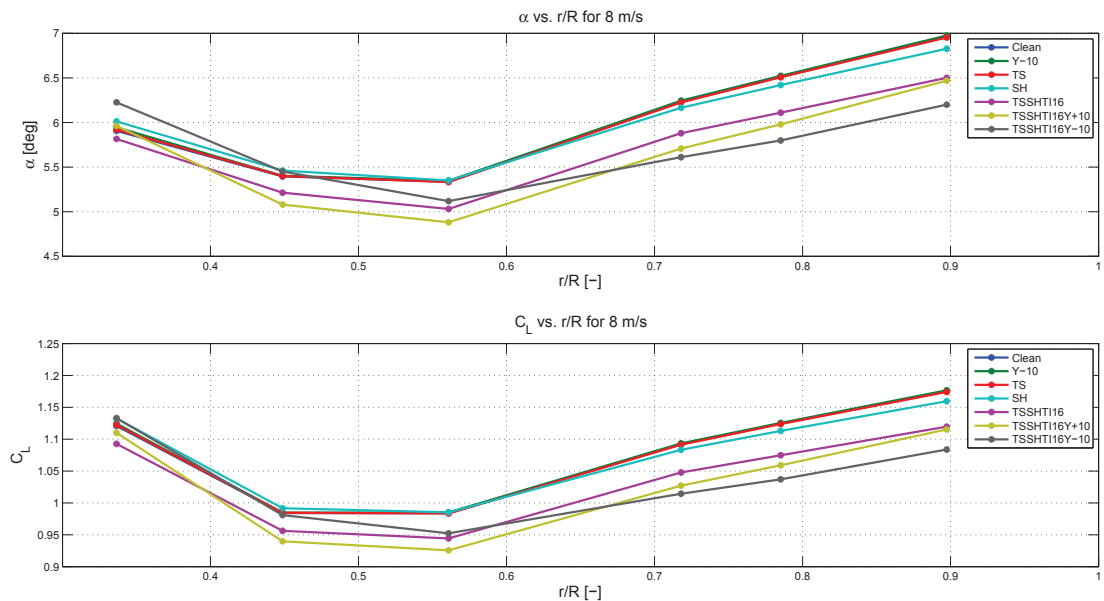


Figure 2.34: Variations of  $C_L$  vs.  $\alpha$  for wind speed 4 – 24m/s shown together with the corresponding airfoil plot for the reference case.



*Figure 2.35: Variations of  $C_L$  vs. azimuth for the reference case.*



**Figure 2.36:** Variations of mean values of  $\alpha$  and  $C_L$  for various unsteady loading cases.

- Turbulence ( $TI = 16\%$ ) will result in a huge increase in fluctuations. The level of increase starts from a factor of 12 near the root, increases to a factor of 14 around the midspan and decreases to a factor of 10 when it reaches the blade tip.

A graphical comparison of the effect of various unsteady loading scenarios in  $\Delta C_L$  is shown in Figure 2.39. It shows variations of standard deviation of lift coefficient at 3 different radial positions on blade ( $0.35, 0.56, 0.9 \frac{r}{R}$  representing max, average and min values respectively) for various unsteady loading scenarios. The average value of  $\Delta C_L = \pm 0.25$  can be a typical value for a real wind turbine and real operating conditions.

Variations of  $\alpha$  for a single rotation of the blades are plotted over the rotor plane (shown in Figure 2.40) for the reference case in which is a representative of a real case for a wind turbine.

It is observed that the wind shear results in higher  $\alpha$  in the upper half of the plane, however, the presence of eddies of various sizes are also observed which result in regions of low and high angle of attack in various parts of the plane.

Therefore, turbulence is the main reason for large  $\Delta C_L$  over the entire blade and the main source of unsteady loads. It is inferred that the unsteadinesses are local and any load control system targeted for maximum mitigation should act local. This is the main reason why distributed flow control can be the best solution for load control on wind turbine blades.

The variations of  $\alpha$  over rotor plane is plotted for various unsteady loading scenarios in Figure 2.41. The following are inferred from the figure:

- Tower shadow results in a region of abrupt low  $\alpha$  in front of it as a result of the presence of the stagnation region.

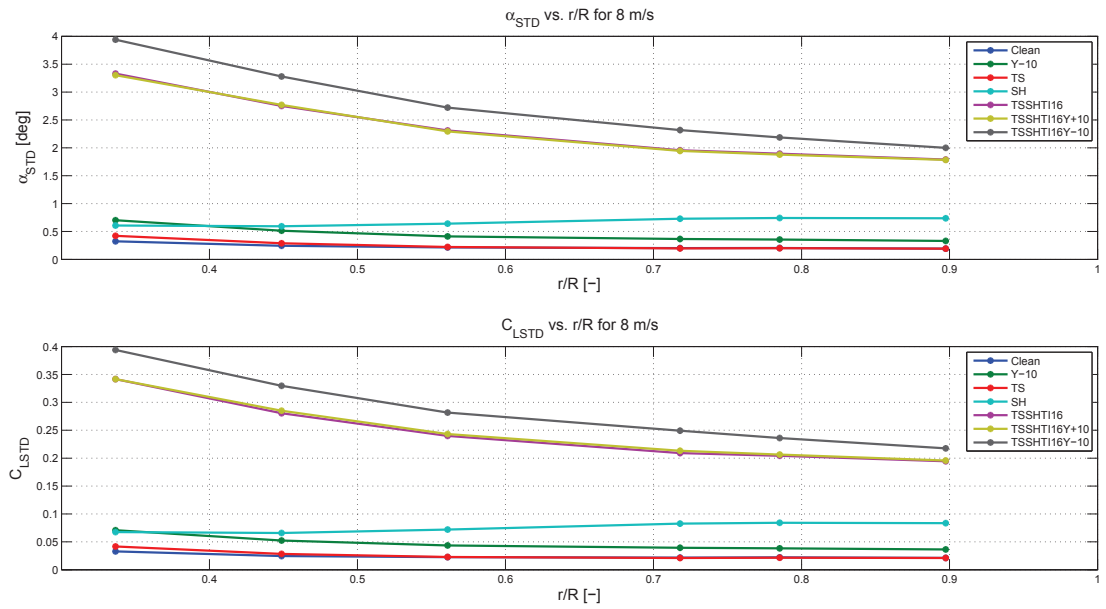


Figure 2.37: Influence of unsteady loads on angle of attack.

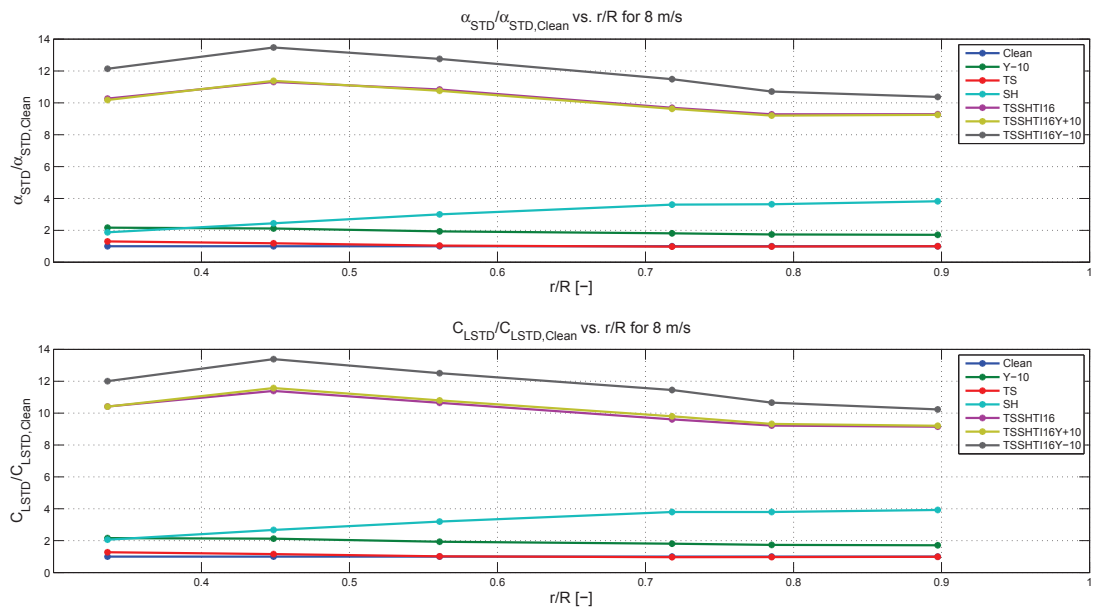
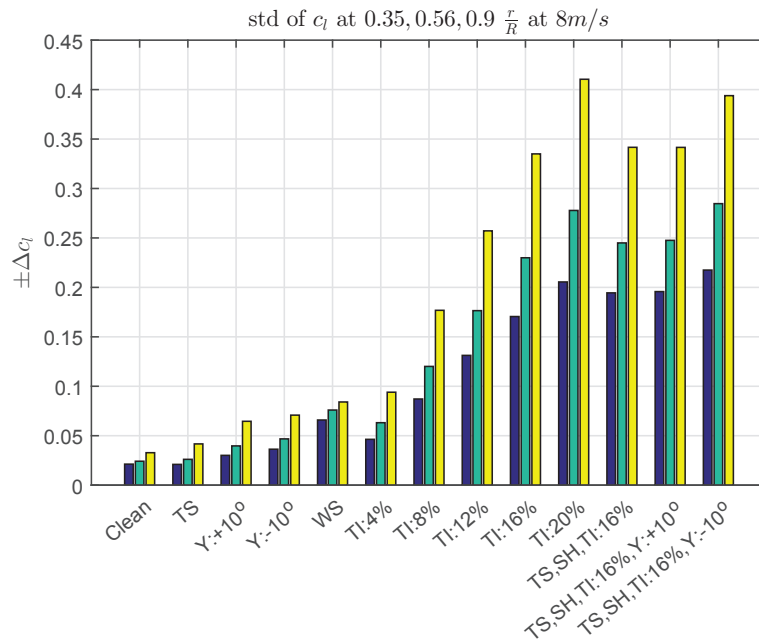
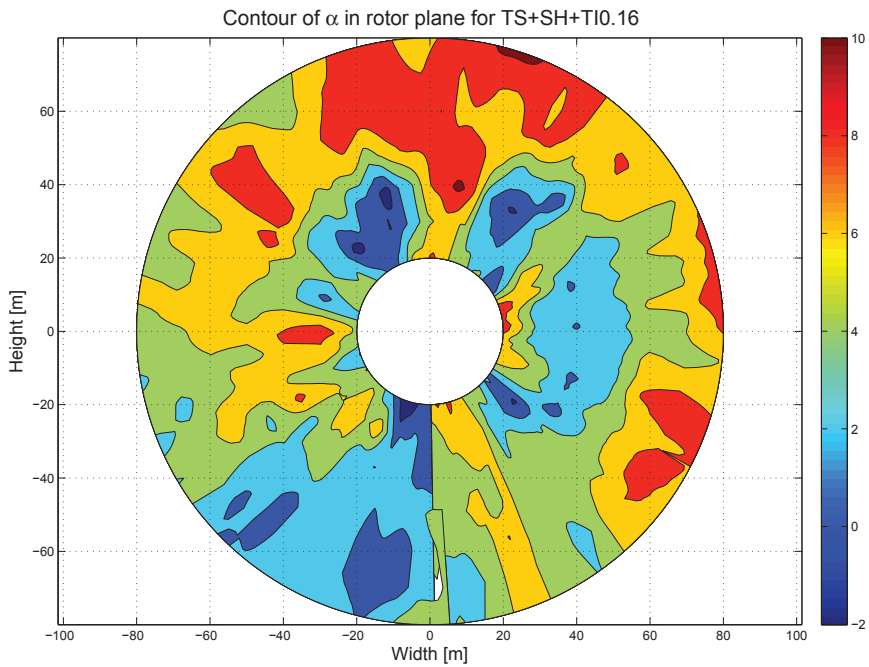


Figure 2.38: Influence of unsteady loads on angle of attack.



**Figure 2.39:** Variations of standard deviation of lift coefficient at 3 different radial positions on blade ( $0.35, 0.56, 0.9 \frac{r}{R}$  representing max, average and min values respectively) for various unsteady loading scenarios.



**Figure 2.40:** Contour of angle of attack for Case 30 under a combination of turbulence, wind shear, tower shadow, gravity, mass and aerodynamic imbalances.

- Yaw will result in a gradual gradient of  $\alpha$  where higher  $\alpha$  is observed in the side where wind is deflected towards. This happens as a result of what happens to the slipstreams during yawed inflow operation [53].
- Wind shear results in a gradual vertical gradient in  $\alpha$  where higher  $\alpha$  is experienced in the upper half.
- Local variations in  $\alpha$  is observed due to turbulent eddies of different sizes passing the rotor plane.
- A combined effect is observed for the last 3 figures where all the effects are applied. They are representatives of real cases for wind turbines.

### 2.3.4 Conclusions for an 'Active Load Control' system

Based on the discussions presented in this chapter, the following conclusions are made. They can be the key points to be considered for the design of an 'Active Load Control' system for wind turbine blades with respect to frequency of loads to target, radial position for the actuators and type of the system.

- The large-scale low-frequency turbulent coherent structures are the main source of unsteady loads on wind turbine blades, the main source of flapwise LEFL and the second main source of edgewise LEFL (after gravitational and imbalance loads).
- The corresponding frequency to the unsteady loads with the highest amplitudes is '1P' which should be the main target for mitigation by any active load control mechanism.
- The frequency range of '1P' loading for a big wind turbine for the applicable range of wind speed is approximately between  $0.1 - 0.6Hz$ .
- Although in the first look this range of frequency seems to be quite low and not demanding for a flow control method to interact. However, it is important to note that as the methods are operated actively based on instantaneous measurements from sensors located locally at the leading-edge of the section, therefore, high response time is a major necessity of any active load control method so that it can respond to real-time data swiftly and counteract with the loads effectively.
- Loads with frequencies of multiples of '1P' ('2P' to '6P') are also of second order of importance considering that the amplitude decreases for increasing the frequency for multiples of '1P'.

Therefore, an active flow control system can target to mitigate the unsteady loads caused by turbulence at these frequencies and be successful at reducing the fatigue loads.

- Due to the local effects of turbulent eddies, unsteadiness in the flow is more of a local phenomena. Therefore, a distributed active load control system intended to damp unsteadiness locally will be the most promising active load control system for a wind turbine blade.
- Within the studied radial range,  $\frac{r}{R} = 0.3 - 0.5$  seems to have the highest variations of  $C_l$ , however, the best radial position for installation of active load control mechanisms is near the tip where the fluctuations are more comparable to the capabilities of active load control mechanisms.
- The fact that sections with  $\frac{r}{R} < 0.35$  happens to experience stall gives the possibility of separation control methods to engage in load control.

However, this conclusion does not reject the possibility of installation of active load control mechanism from midspan to tip as although fluctuations are slightly smaller but larger distance to root can be more effective in mitigation of blade root moments.

- Flapwise and edgewise LEFL are in the same order of magnitude, even if the flapwise LEFL caused by large-scale low-frequency turbulent coherent structures is mitigated by active load control, still the edgewise LEFL which is mainly caused by gravitational loads stays almost in the same level and can be a wind turbine lifetime limiter if the blade mass stays constant. However, the results of a current study [6] show that a 25% reduction in flapwise LEFL can result in a blade with 6% lower weight. This can clearly show that active flow control on blades can directly reduce the flapwise LEFL and

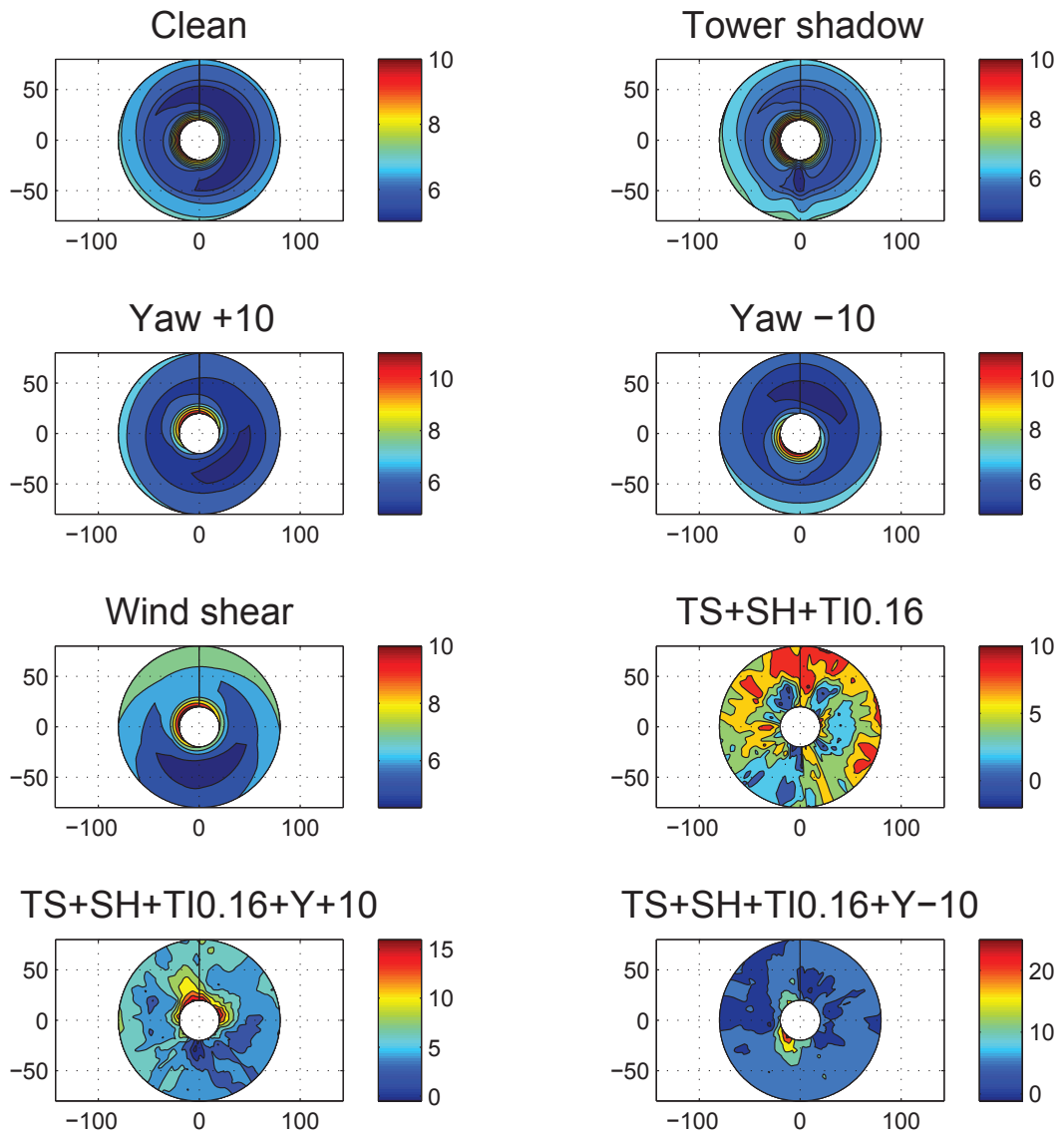


Figure 2.41: Influence of unsteady loads on angle of attack.

indirectly reduce edgewise LEFL by weight reduction.

- Increasing the aerodynamic efficiency of the blade is another solution that can directly result in lighter blade with less fatigue loads. Active flow control on wind turbine blades can be targeted for increasing aerodynamic efficiency of the blade during operation or mitigating the unsteady loads and they both can result in lower fatigue loads and lighter blades.

# Load Control for Wind Turbine Blades

## 3.1 Flow control

Any type of manipulation of the fluid flow including passive or active; geometrical, fluidic, momentum or heat transfer targeted to a beneficial change in the flow characteristics can be identified as '*flow control*'. Flow control methods can address the flow in order to control transition to turbulence, flow separation, circulation, noise, mixing, and loads [26]. These goals and their relation are shown in Figure 3.1. These goals can be achieved using various types of flow control devices listed in Figure 3.2.

The flow control devices have extensively found applications in aircrafts, cars and more recently on wind turbines. Later in this chapter, we will focus on applications of flow control on wind turbine blades.

## 3.2 Flow control on wind turbines

Air flow on wind turbines is complex for several reasons listed below:

1. Wide range of operating conditions
2. Unsteady turbulent inflow with gradient of mean speed in both vertical and lateral directions
3. Flexible rotating blade
4. Contaminations on blades during operation

To achieve higher aerodynamic efficiency from this unsteady complex inflow with desirable loading on blades, flow control emerges as a promising technology.

A variety of flow control methods has ever been investigated on wind turbine blades including vortex generators [29, 63], winglets [27], Gurney flaps [16, 74], plasma actuators [48, 20], suction [75, 19], blowing [70, 28, 60], trailing-edge tabs/flaps [69, 5, 10], morphing blades [72], and synthetic jets [46] and the studies cover both experimental and numerical studies.

The aforementioned methods addressed the flow in this regime with respect to separation control (delay/augmentation), circulation control, unsteady load control, transition control (boundary layer stabilization/active

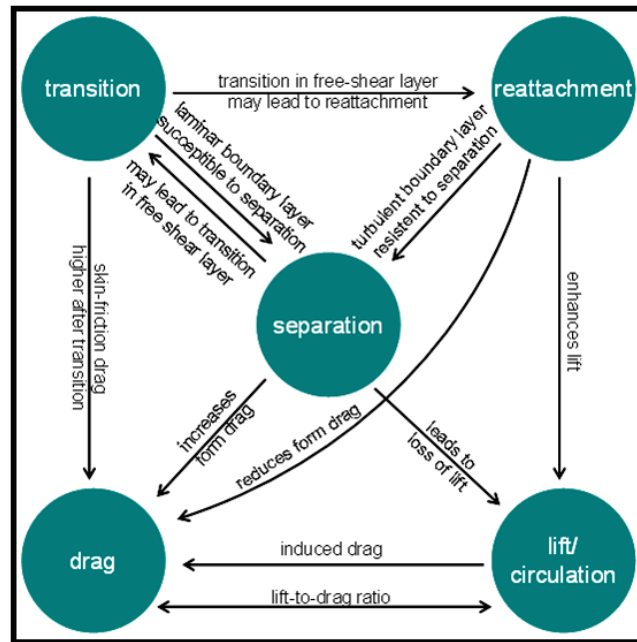


Figure 3.1: Flow control objectives.[26]

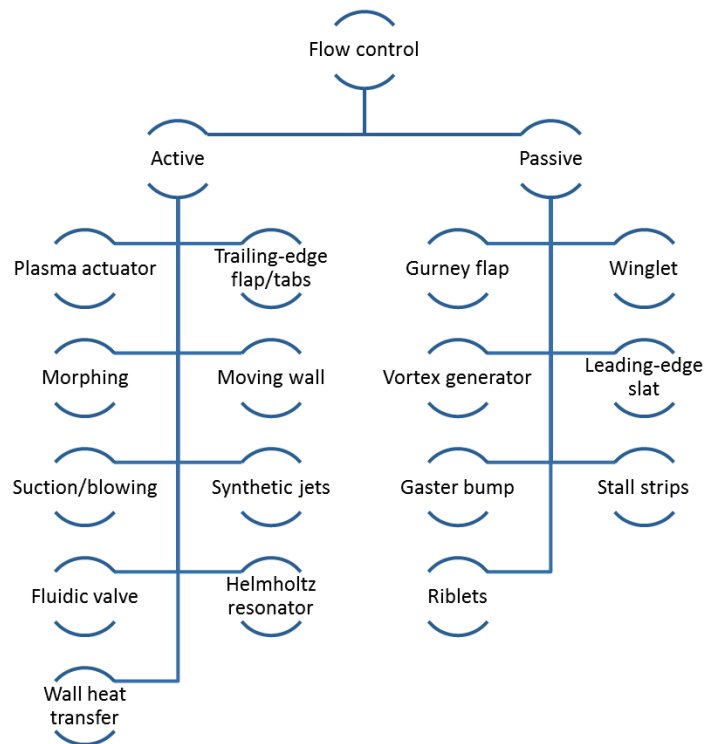


Figure 3.2: Flow control methods.

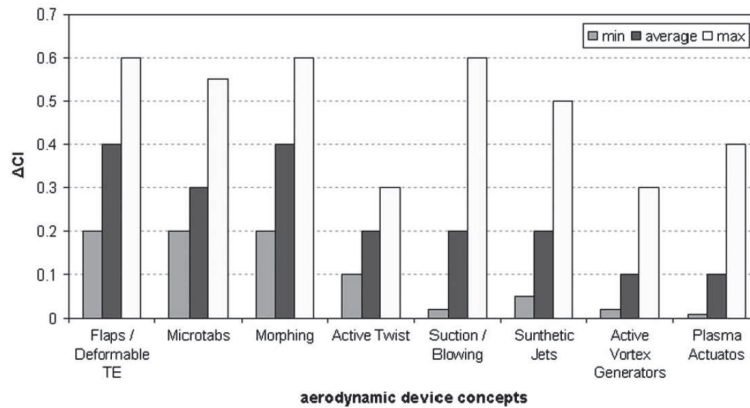


Figure 3.3: Achieved  $\Delta C_L$  for various flow control methods.[8]

wave cancellation), noise suppression, wing tip vortex control, and drag reduction.

Based on the context of this research, the flow control objective which is of main interest in the current research is 'active load control' using 'circulation control' at the trailing-edge. Therefore, this concept and the relevant literature are reviewed in the following sub-sections (subsection 3.2.1 and subsection 3.2.1.1).

### 3.2.1 Active load control on wind turbine blades

The studies show that different methods have been able to control the blade lift to a significant amount. A comparison of the achieved  $\Delta C_L$  for various flow control methods is shown in Figure 3.3.

Figure 3.3 shows that flow control methods have been able to control the lift coefficient up to an average value of  $\Delta C_L = 0.1 - 0.4$  for various methods. This is a very good achievement when compared to the results of the simulation shown in Figure 2.39 in subsection 2.3.3 that declares an average  $\Delta C_L = 0.25 - 0.3$  as an aggregate result of all the unsteady loading sources on wind turbine blades. This shows the great potential of flow control methods to mitigate the unsteady loads on wind turbine blades.

#### Trailing-edge flaps:

Trailing-edge flaps have shown the highest potential with  $\Delta C_L = 0.4$ . Soft-curved trailing-edge flaps have shown better result with respect to  $\frac{L}{D}$  compared to rigid and highly-curved flaps. It has been shown that dynamic lift from oscillating airfoil can be controlled using a counteracting flap for reduced frequencies  $k = 0.09 - 0.36$ .  $k$  is defined as Equation 3.1 where  $\omega$  is the angular frequency of unsteadiness,  $c$  is the blade chord and  $V$  is the resultant velocity.

$$k = \frac{\omega c}{2V} \quad (3.1)$$

Lackner and van Kuik shows that application of trailing-edge flaps with 0.1 chord of the blade and  $\pm 10deg$  deflections at 20% of blade span can reduce the blade root fatigue loads up to 15% in Class-B turbulence ([31]) and wind speeds before rated. This is a great achievement especially when compared to individual pitch control (IPC) which is in the same range. Barlas reported 14% reduction in blade root fatigue loads

applying TE-flaps with 0.1 chord of the blade and  $\pm 8deg$  deflections at 18% of blade span.

Andersen et al. studied a huge reduction of 34% in blade root fatigue loads using TE-flap with former settings. The research used a much lower level of TI and wind shear rather than the prescribed values in the IEC standard[31]. Lackner and van Kuik investigated the hybrid application of IPC and TE-flaps and 20% reduction in blade root fatigue loads was reported. Markou et al. studied an advantage of TE-flaps over IPC in mitigation of loads due to wake of other turbines. The reason is believed to be the fact that unsteady loads due to turbine wakes change with higher frequency compared to loads caused by atmospheric turbulence. This is a result of wake meandering. However, the uncertainty in the reported load reductions is still high as the results are very limited cases with low TI compared to IEC standard[31].

### **Microtabs:**

Microtabs are very small deployable tabs with the size in the order of boundary layer thickness (1 – 2% of chord) which are able to change the average  $C_L$  within  $\Delta C_L = \pm 0.3$ . They are basically active circulation control mechanisms originated from Gurney flaps with the difference that microtabs are deployable.[17, 5, 35]

Microtabs can be used on the pressure side to increase the lift or on the suction side to decrease the lift. They change the position of the trailing-edge, manipulate the Kutta condition and consequently the airfoil circulation. The main operational difference with TE-flaps is that microtabs are operated in 'ON-OFF' modes and normal positioning to the chord is defined as 'ON' mode while TE-flaps can have various angles during operation. Therefore, TE-flaps are more powerful in load control. However, microtabs have faster response time, less mass, cost and complexity compared to TE-flaps.

### **Morphing trailing-edges:**

By using smart materials or deformable structure inside the blade, the camber of the airfoil can be actively controlled and this leads to control  $C_L$  within  $\Delta C_L = \pm 0.4$ . [72, 10]

### **Active twist:**

Another load control method investigated for wind turbines is the active twist control for the whole span or outboard parts. This enables variations of  $C_L$  within  $\Delta C_L = \pm 0.2$  via variation of angle of attack. However, there are several disadvantages with this method which are slow response time, structural limitations, high complexity, mass and cost.[8]

### **Active vortex generator (VG):**

Active VGs are separation control devices that can be used to delay stall and increase lift for high angles of attack or virtually change the airfoil camber and decrease the lift at lower angles of attack. They are simple fast-response devices but with low functionality that can change  $C_L$  within  $\Delta C_L = \pm 0.1$ .

### **Synthetic jet:**

Synthetic jets are zero-net mass flux passive flow control devices that can change the average  $C_L$  within  $\Delta C_L = \pm 0.2$  with momentum addition in boundary layer.

**Suction/blowing:**

Suction can be used for separation control for high angles of attack while blowing can be an active circulation control device. Blowing at the trailing-edge can change the trailing-edge flow and manipulate the Kutta condition. This can change the average  $C_L$  within  $\Delta C_L = \pm 0.2$ . [70, 60]

**Gurney flap:**

Gurney flaps are small fixed tabs with the size in the order of boundary layer thickness (1 – 2% of the chord) which act as passive circulation control devices. They are mainly mounted on the pressure side of the airfoil to increase the lift by manipulation of Kutta condition and trailing-edge flow. They can increase lift significantly with small drag penalty. The reported amount of increase in maximum  $C_L$  is up to 20% at  $\alpha$ . Gurney flap can passively increase the average  $C_L$  for  $\Delta C_L = 0.2$  while increasing the  $C_D$  for average 40 – 50%. [66, 4, 57]

**Plasma actuator:**

Plasma actuators are active flow control devices that can control the aerodynamic loads by control of circulation, transition or separation based on their chordwise positioning and direction of actuation. They can change the average  $C_L$  within  $\Delta C_L = \pm 0.1$ .

Kotsonis et al. showed the high capability of plasma actuators to manipulate the Kutta condition and control the aerodynamic loads when applied at the rounded trailing-edge of a symmetric airfoil. Based on the interest of this research, i.e. active load control by airfoil circulation control using plasma actuators at the trailing-edge of airfoil, plasma actuators are extensively explained in section 3.3. The concept of circulation control is shortly reviewed in subsection 3.2.1.1.

**Comparison of methods:**

The aforementioned load control methods are compared with respect to capability to control the loads, response time, complexity, mass and cost and the result is shown in Table 3.1. Plasma actuators are distinctive as a low cost, low mass, low complexity mechanism with very high response time and competitive capability in load control. Therefore, this method has high potential to be applied as an active flow control method for wind turbines. They are chosen as the load control mechanism in this research.

**3.2.1.1 Circulation control for wind turbines**

Based on Kutta-Joukowski theorem, the relation between airfoil lift and flow circulation around the airfoil is expressed as Equation A.1 where  $U_\infty$ ,  $\rho_\infty$  and  $\Gamma$  are freestream velocity, density and circulation respectively. Therefore, any change in the flow circulation around the airfoil can directly change the lift as the main load on the airfoil.

$$L = -\rho_\infty U_\infty \Gamma \quad (3.2)$$

**Table 3.1:** Comparison of advantages and disadvantages of passive and active load control methods for wind turbines. (P=passive; A=active)

Method	Response time	Mass	Complexity	Average $\Delta C_L$	A/P
IPC	Low	High	High	N/A	A
TE-flap	Low	High	High	0.4	A
Micro-tab	Medium	Medium	Medium	0.3	A
Morphing TE	Low	High	High	0.4	A
Active twist	Low	High	High	0.2	A
Suction/blowing	Medium	High	High	0.2	A
Synthetic jet	High	Low	Low	0.2	P
Active VG	Medium-High	Low-Medium	Low	0.1	A
Plasma actuator	High	Low	Low	0.1	A
Gurney flap	N/A	Low	Low	0.2	P

Circulation on the airfoil can be altered via change in airfoil camber and trailing-edge flow development, i.e. manipulation of Kutta condition. Gurney flap, microtabs, trailing-edge plasma actuators and trailing-edge suction/blowing are the flow control methods investigated for wind turbines. These mechanisms can directly manipulate the Kutta condition and change the circulation around the airfoil and consequently loads.

The application on circulation control on H-type vertical axis wind turbine could increase the power by 24% for a trailing-edge blowing with blowing coefficient of 10% [71]. Further explanations on circulation control and relevant devices can be found elsewhere [41].

### 3.3 DBD Plasma Actuators

#### 3.3.1 Introduction to Plasma Actuators

Plasma is commonly referred to as the fourth state of matter which is combined of neutral and ionized particles and electrons while has a quasi-neutral integrity and shows a collective behavior. Another condition for a plasma is that the number of charged particles in a sphere of influence around a particular charged particle is high enough to secure a collective behavior. The sphere of influence is referred to as Debye sphere. Due to the presence of free electrons, plasma is generally conductive. [11]

Plasma actuators are flow control mechanisms that interfere with the fluid flow via a plasma medium created by the actuator. This kind of actuator can use different mechanisms to control the flow. The two most-widely knowns are *body force* and *thermal energy deposition*.

The first group of plasma actuators transfer body force to fluid by means of an ionic wind. This type is called 'AC-DBD' (Alternating-Current Dielectric Barrier Discharge) plasma actuator which will be comprehensively explained later in this section. This actuator is the most widely studied and used for flow control applications. The second type of the plasma actuators which uses thermal energy deposition into fluid for flow control applications is ns-DBD (Nano-second DBD) which is not a part of this study and can be extensively studied elsewhere [62, 56].

The typical configuration for an AC-DBD plasma actuator consist of two electrodes, one exposed to the air and connected to high-voltage AC source (anode electrode) while the other one is covered under a dielectric layer and connected to ground (cathode electrode). The high-voltage between the electrodes ionizes the air in between and current passing between the electrodes creates an ionic wind which transfers momentum into neutral air particles. This body force can be wisely utilized for many different flow control applications.

This configuration which is shown in Figure 3.4 is commonly referred to as single DBD (SDBD). It can be seen that the electrodes are asymmetrically positioned; on the contrary to the parallel configuration which has a different operating physics and other industrial applications [18].

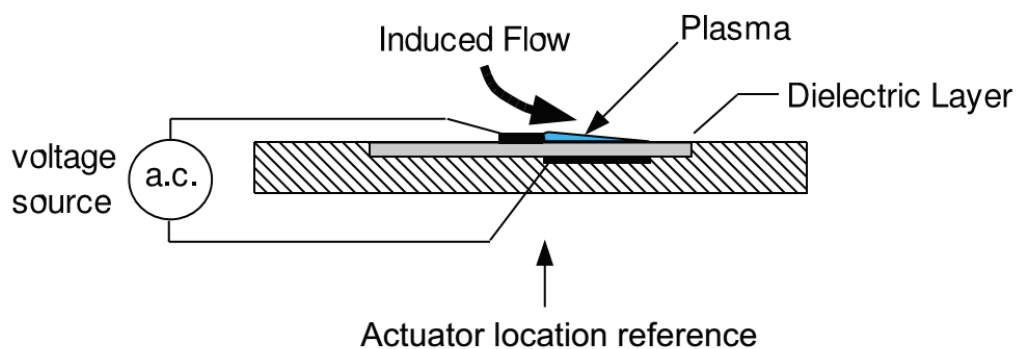


Figure 3.4: Schematic SDBD plasma actuator. [18]

Dielectric Barrier Discharge (DBD) plasma actuator as an active flow control mechanism offers many advantages over the other active and passive flow control mechanisms. Some of the advantages of DBD plasma actuators can be listed as below:

1. All-electric with no moving parts, no hydraulics or pneumatics
2. Very small size and very low mass
3. Very thin, ideal for integration into aerodynamic shapes
4. Very fast response, ideal for unsteady flow control
5. Reynolds number-independent body force
6. High energy conversion efficiency
7. Easy installation
8. Easy to implement the plasma actuator effect (body force) into numerical flow solvers

### 3.3.2 Physics of DBD Plasma Actuator

Before describing the ionization process in a DBD plasma actuator, it is important to mention the main characteristics of the plasma generated by the actuator. The main features of the plasma generated by a DBD plasma actuator can be described by 5 characteristics which are of paramount importance regarding the operating physics of a DBD plasma actuator.

1. *Cold:*

The electron temperature ( $K$ ) of the generated plasma by DBD plasma actuator is less than  $10^5 K$  (less than  $10^1 eV$ ) which is characterized as cold plasma. [14]

2. *Non-thermal equilibrium:*

One of the main reasons for the utilization of the dielectric layer to cover one of the electrode of the actuator is to enable a non-thermal equilibrium between the plasma and the surrounding air. Therefore, the energy deposited will not waste into heating the flow but ejection of high-energy electrons for ionization and acceleration of the particles. Finally, the neutrals and ions will remain at atmospheric temperature while electrons have very high temperatures. This is on the contrary to a spark or thermal arc where a thermal equilibrium exists. The reason for this is that during the discharge charge builds up on the dielectric surface and ultimately self-terminates the discharge before changing into a thermal arc. [24]

3. *Collisional:*

As the DBD plasma actuators typically operate at atmospheric and near-atmospheric air, therefore the density of air is quite high. Thus, the frequency of collisions between electrons and neutral particles is in the order of or greater than the plasma driving voltage frequency. Consequently, these regime of plasma is referred to as collisional plasma.

4. *Weakly ionized:*

The number density  $n$  (charged particles per cubic meter) of the generated plasma by DBD plasma actuator is in the order of  $10^{15}$  which is characterized as weakly ionized plasma. [14]

5. *Extremely low-intensity blue light emission:*

The DBD plasma actuator emits a blue light of very low intensity which requires a dark environment to be visible. The color is a result of decomposition of components of the generated plasma.

The operating physics of DBD plasma actuators can be simply divided into two main phases [18] and each are elaborated separately.

1. Ionization of the fluid to generate the plasma (subsubsection 3.3.2.1)
2. Acceleration of ionized particles (plasma) in order to transfer body force to fluid through ionic wind (subsubsection 3.3.2.4)

### 3.3.2.1 Ionization

A medium (air in case of DBD plasma actuator) can be ionized in different ways. Electron Impact ionization (EI), Fast Atom Bombardment (FAB), Electrospray ionization (ESI), laser-assisted ionization, thermal ionization, radio-frequency and microwave ionization are only a few methods ever investigated for ambient ionization [1].

The main difference of utilization of various methods for the same molecule is ionization of atoms with different relative intensity (of light emission), charge, bi-polarity and ionization efficiency. The ratio between the number of ionized particles formed to the initial neutral particles present is defined as ionization efficiency.

The ionization method for DBD plasma actuators is Electron Impact ionization (EI) which can be simply described as removing electrons from (or adding to) neutral atoms by electron collision (Figure 3.5). The ejection of electrons can be made if the energy of the incoming electron is higher than the ionization potential of the neutral particle. The ionization potential can be defined as the energy to eject the electron with the weakest bound from the neutral molecule.

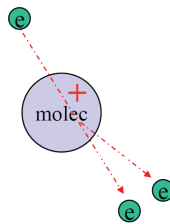


*Figure 3.5: Schematic of electron impact with a neutral atom in EI ionization method. [34]*

In this method, there is an electron emitter source (anode) which is connected to high voltage (AC or DC) and an electron absorber (cathode) which is connected to the same ground. In case of AC current, emitter and absorber change place in each half-cycle if the voltage magnitude changes sign.

When a positive voltage is applied to a DBD plasma actuator, the exposed electrode is the anode and electron emitter source and the covered electrode is the cathode and electron absorber. When the applied voltage changes sign, they also change place. It is important to note that, in case of a DBD plasma actuator, as the covered is covered by the the dielectric layer, it can not directly absorb the electrons but they only accumulate on the surface of the dielectric. The details of this process is described in subsection 3.3.2.2.

The ionization process can be explained as two major processes, i.e. initiation and sustaining the plasma.

#### Initiation of ionization

When the amplitude of electric field across a gap where fluid is present increases above the break down electric field  $E_b$  of the medium, electric current (electrons) starts crossing the gaps and while crossing they collide the neutral fluid particles and change some of the neutral particles into ions [40].

Considering the fluid as air which is the case for DBD plasma actuators, the generated ions can be positive (e.g.  $N^+$  and  $O^+$ ) where an electron is removed from the atom by collision or negative (e.g.  $O^-$ ) where an electron is added into the atom. Another condition for the initiation is the pre-presence of some free

electrons across the gap that make the path and enable the first crossing of the current.

The minimum break down electric field  $E_b$  is dependent on the driving current frequency and is generally lower for AC current compared to DC in atmospheric conditions which are typical of DBD plasma actuators.

### Sustaining the generated plasma

After the plasma is initiated, it needs to be sustained. The electric field required to sustain the generated plasma  $E_s$  is basically lower than  $E_b$ . The difference is mostly dependent on the operating conditions, i.e. static pressure, applied field and electrode cross-section.

#### 3.3.2.2 Importance of the dielectric layer

DBD plasma actuators generate a '*normal glow discharge*' and operate in '*micro-discharge*' mode. The two phenomena are described below.

As a result of the plasma conductivity, current flows from anode to cathode and a region of the plasma is created that is responsible to maintain current at the interface between the plasma and the cathode. The current that passes into the cathode consists of conduction current  $I_c$  and displacement current  $I_d$ . There is an operating condition that the current going to the cathode is independent of the cross-section of the interface region. This type of discharge is called '*normal glow discharge*'. [55]

When one of the electrodes is covered with a dielectric layer, the discharge will change into a number of stable micro-discharges. This mode of operation is referred to as '*micro-discharge*' mode. The micro-discharge mode consists of numerous short-lifetime parallel filaments. [37]

The application of the dielectric layer offers several advantages to the discharge as below:

- Stability
- Homogeneity
- Self-termination of discharge (enabling non-thermal equilibrium plasma)

The latter is of paramount importance as it keeps the plasma in non-thermal equilibrium by preventing the discharge transition into a thermal arc. When the current flows from anode to covered cathode, traveled electrons can not reach the cathode due to the presence of the dielectric layer and therefore accumulate on the surface of the dielectric and a capacitance is created. This leads to a negative charge built-up on the dielectric surface and finally during each period there is a time that the negative charge on the dielectric is more than the anode negative charge. This leads to self-termination of the discharge. Consequently, in the second half of the cycle current flows from the negative charge on the dielectric surface to the exposed electrode and the current reverses. It is good to note that the capacitance of the dielectric affects the lifetime of the micro-discharges. Termination of each micro-discharge follows this principle in a local scale.

#### 3.3.2.3 Main characteristics of a full cycle

Simple visual observation of operation of DBD plasma actuators shows a uniform distribution of the plasma over the electrodes. However, light emission time series [49] showed a series of dynamic temporally- and spatially-evolving processes in each cycle. The time scales of the processes are in the order of or smaller than the period of ac current (ms).

There are some characteristics of physical processes which are similar in both half-cycles. First, ionization occurs only in parts of each half-cycle, however, the behavior of ionization is different in each half-cycle. Second, when ionization occurs, it consists of numerous micro-discharges in both half-cycles. However, the intensity and number of micro-discharges are different in each half-cycle.

Figure 3.6-left [49] shows the light density captured by photo-multiplier tube (PMT) focused on a narrow 2D area of plasma generated by the actuator. It can be seen that the negative-going half cycle consists of higher number of micro-discharges with much lower intensity while the positive-going half cycle consists of less number of micro-discharges with much higher intensity. It can be explained as during the negative-going half-cycle electrons eject from the exposed electrode which is a good source of electrons but during the positive-going half-cycle electrons has to eject from the dielectric surface. This is so important to understand the asymmetry in the physics of DBD plasma actuators. This can help in better optimization of the momentum transfer. Light intensity is considered as a representation of plasma density.

Figure 3.6-right [49] shows the temporal and spatial evolution of light intensity over the DBD plasma actuator. The lower half of the figure belongs to the negative-going half cycle and the upper corresponds to the positive-going half cycle. The position ( $x = 0$ ) shows the edge of the covered electrode and the slope ( $dx/dt$ ) represents the plasma front velocity. The figure implies several important characteristics of physics of the actuator which are listed below:

- Plasma is generated over the dielectric surface for both half cycles.
- Plasma font velocity is almost the same in both half-cycles.
- Plasma travels much farther on the dielectric surface during the positive-going half-cycle.
- The intensity is much higher during the positive-going half-cycle.
- In both half-cycles, plasma reaches the maximum intensity almost quickly but the the positive going half-cycle experiences longer duration of maximum intensity.

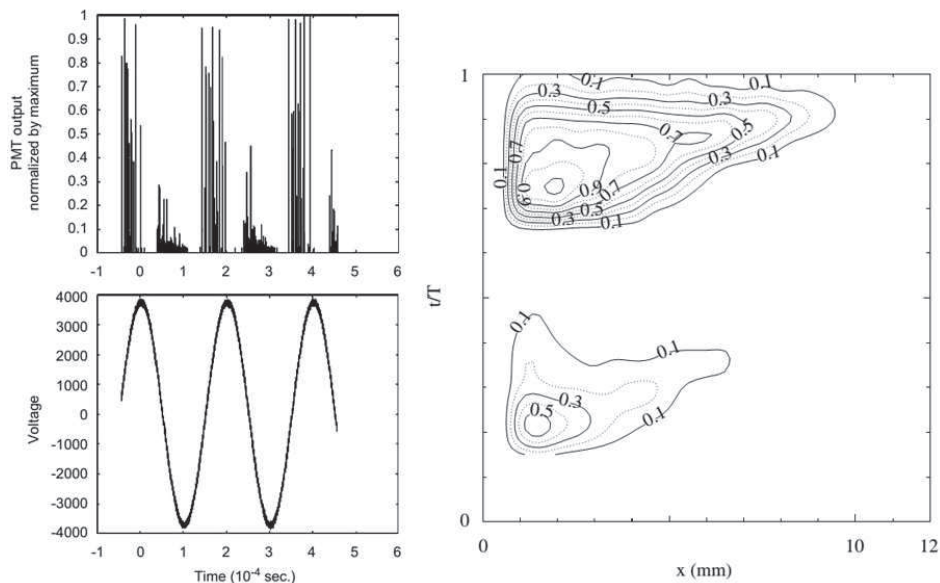


**Figure 3.6:** Light emission from a SDBD captured with a PMT focused on a narrow 2D area of plasma. [49]

The characteristics of each half-cycle are described separately below.

### Negative-going half-cycle

The understanding of the observations implies that in the negative going half-cycle, negative charge starts building up on the exposed electrode. When the generated electric field outnumbers the  $E_B$  (point  $a$  in Figure 3.7), then ionization starts and plasma is created and electrons starts to cross the gap from the exposed electrode toward the covered electrode. Therefore, negative charge accumulate on the dielectric surface. The ionization continues until the increase in the magnitude of voltage stops (point  $b$  in Figure 3.7). At his point, the ionization stops.

During this negative-going half cycle, electrons move from the exposed electrode towards the covered electrode (dielectric surface). On the contrary, the heavy ion particles move from the covered electrode (dielectric surface) towards the exposed electrode.

As the heavy particles make a major contribution to momentum transfer due to their large mass and in this half-cycle they are moving opposite to the desired direction, therefore, this half cycle makes less contribution in the total momentum transfer. It is good to note that although the ions move in the opposite direction but studies [25] have shown that the net force is still in the favorable direction. The direction of the force is most probably only dependent on the configuration of the electrodes and from the exposed electrode towards the covered one.

### Positive-going half-cycle

Ionization will restart in the next positive-going half cycle when voltage has changed sign and the electric field has grown more than the  $E_B$  (point  $c$  in Figure 3.7). The ionization continues until the magnitude of the voltage stops increasing (point  $d$  in Figure 3.7) and this is the end of a full cycle. In the positive-going half-cycle, electrons are moving from the covered electrode (dielectric surface) toward the exposed electrode. On the contrary, the heavy ion particles are moving from the exposed electrode towards the covered electrode (dielectric surface). Due to large mass of ions and their favorable movement direction, this half cycle makes the major contribution to the momentum transfer. The understanding of the processes in a full cycle can greatly assist in designing optimum AC waveforms for the actuator to maximize the body force.

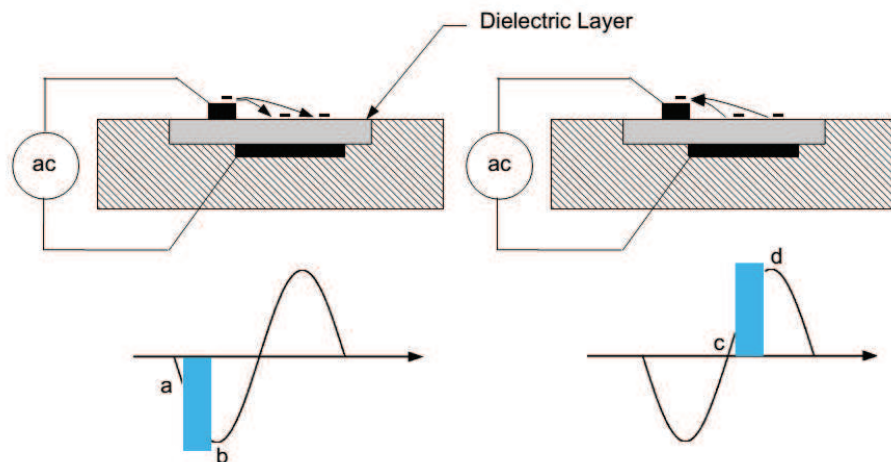


Figure 3.7: Schematic of electron impact with a neutral atom in EI ionization method. [34]

### 3.3.2.4 Momentum transfer

The results of time resolved LDV (laser Doppler velocimetry) [25] and particle image velocimetry (PIV) [23] show that the momentum transfer of the DBD plasma actuator to the flow follows PUSH-push scenario. A major contribution to the momentum (PUSH) is made in the positive-going half-cycle where the heavy positive ions move from the exposed electrode towards the covered electrode and a minor contribution (push) is made during the negative-going half cycle where the heavy positive ions move in the opposite direction. An important conclusion of the PUSH-push scenario is that both half cycles contribute to the momentum transfer and add to the value but in different amounts. The velocity measurement using different methods showed that  $u$  component of velocity has always a positive sign during the full AC cycle and its magnitude varies between a large positive value and a small positive value.

### 3.3.2.5 Optimized design

Experimental Investigations in the last decade have resulted in better understanding of the physics of DBD plasma actuators. Based on the gained understanding, the design of the actuator has been optimized. This has resulted in wider range of flow control applications. Several parameters to be considered for an optimized design of the actuator can be briefed as below:

#### Type of current:

As DBD plasma actuators typically operate at atmospheric and near-atmospheric air, they typically have AC current input. As previously discussed, in the atmospheric conditions  $E_b$  is generally lower for AC currents lower, therefore, they operate at lower voltage. This results in longer lifetime due to less electrode corrosion.

#### AC waveform:

Based on the discussion on the ionization for DBD plasma actuators in subsection 3.3.2.1, to achieve the best ionization, the waveform must be in a way that maximizes the duration between points  $a$  and  $b$  in negative-going half-cycle and between points  $c$  and  $d$  in positive-going half-cycle Figure 3.7. This will result in the various waveforms to be sorted in the order of preference from best to worst: saw-like wave, triangle wave, sinusoidal wave, square wave.

#### AC frequency:

There is an optimum driving frequency for an AC input based on the actuator capacitance which can be chosen for an optimized operation. The value can be experimentally extracted for each design.

#### Thick dielectric material:

As previously discussed, DBD plasma actuator body force is proportional to  $V_{ap}^{3.5}$  where  $V_{ap}$  is the applied voltage. Therefore, to have actuators with higher body force, they need to operate at higher voltage.

Investigations [65] show that in order to enable the actuators to operate at higher voltages, the power loss needs to be minimized. Power loss of the actuator can be minimized by minimizing the capacitance of dielectric. The capacitance is defined as the ratio between the dielectric coefficient over dielectric material thickness ( $\epsilon/h$ ). Therefore, an optimum design should opt for thicker dielectric material with lower dielectric coefficient.

### Electrode geometry:

Studies [25] have shown that non-overlapping electrodes with a non-dimensional gap of  $0 \leq \frac{g}{L_{ce}} \leq 2$  results in maximum induced velocities, where  $g$  is the gap spacing and  $L_{ce}$  is the length of covered electrode.  $g$  is defined positive for non-overlapping electrodes.

### 3.3.3 DBD plasma actuators for flow control

As a result of the many advantages of DBD plasma actuators listed in subsection 3.3.1, they have been the focus of many research activities during the last decade and their design have been significantly optimized (as discussed in subsection 3.3.2.5).

Therefore, DBD plasma actuators have found various applications in flow control in a wide range flow regimes, i.e. subsonic to hypersonic; flow types, i.e. internal and external, multi-phase and multi-species, combustion; and flow scales, i.e. wind turbine scale to microfluidics; and application types from flow control to sensory.

An overview of their applications is shown in Figure 3.8.

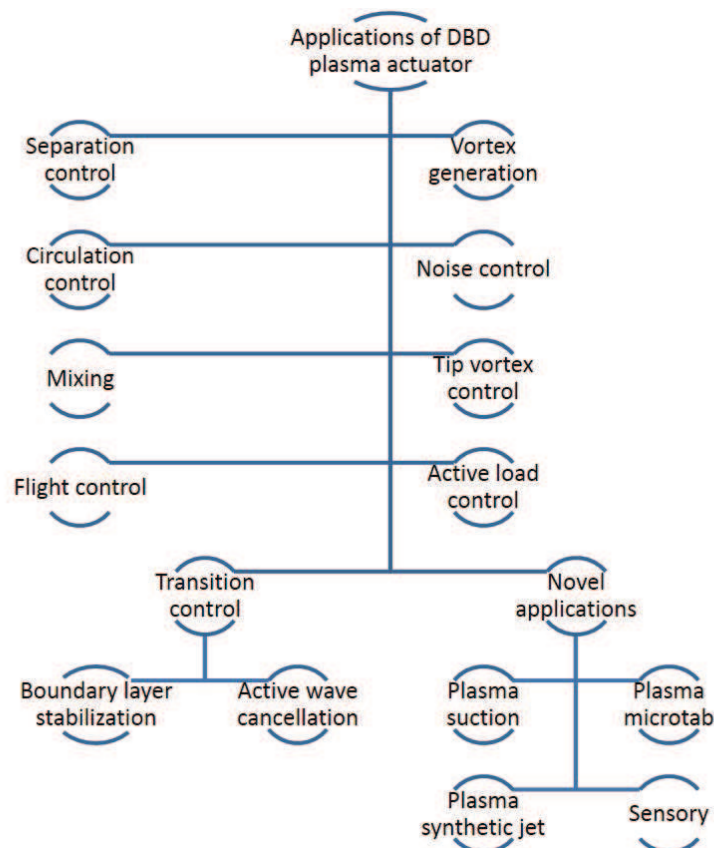


Figure 3.8: Application of DBD plasma actuator in flow control.

In order to understand the capabilities of plasma actuators in flow control, It is important to know how the plasma actuation manipulates the flow both in a transient and steady operation. It can be extensively studied elsewhere [38].

## Methodology and Experimental Set-up

An experimental study has been conducted to investigate the effect of trailing-edge plasma blowing on variation of lift and drag coefficients for three different trailing-edge shapes and various actuation methods. Moreover, the effect of single and multi-DBD plasma actuation has been investigated. In this chapter, the design of the experiments and the airfoil models are explained.

### 4.1 Airfoil models

The original version of NACA64-2-A015 airfoil with a sharp trailing-edge and two modified versions of the same airfoil with half-round and round trailing-edges are utilized in the experiments. Figure 4.1 shows the three airfoil profiles. The airfoil with the round trailing-edge is the modified version from [52].

The main part of the body of the airfoil is made of solid aluminum to ensure minimum surface roughness. The removable section in the middle is made of *Polyoxymethylene (POM)* in order to provide a non-conductive section to prevent the high voltage from plasma actuator to discharge into the airfoil and wind tunnel body for security reasons. The detachable trailing-edges are made of *Polycarbonate*. This part is to serve as the dielectric layer for the DBD plasma actuator and therefore, the material is chosen with respect to its desirable dielectric constant ( $\epsilon_r$ ).

The dimensions of the airfoils are described in Table 4.1.

*Table 4.1: Dimensions of the airfoils.*

	Trailing-edge shape		
	Sharp	Round	Half-round
Chord [mm]	240	217	219
Thickness ratio (t/c)	0.15	0.166	0.164
Detachable trailing-edge thickness [mm]	3	3	3
Span [mm]	560	560	560

In order to force transition to turbulence to ensure similar flow conditions for all test cases and to avoid the laminar separation bubble to affect the results of lower wind speeds, a pair of roughness strips of *Carborandom* grains are attached at approximately  $x/c = 0.1 - 0.2$  on both suction and pressure sides.

Despite the great attention in installation of this strips, the Carborandom strips covers  $x = 2 - 4cm$  from the leading-edge on suction-side and  $x = 2.4 - 4.8cm$  on the pressure-side. This results in earlier stall at

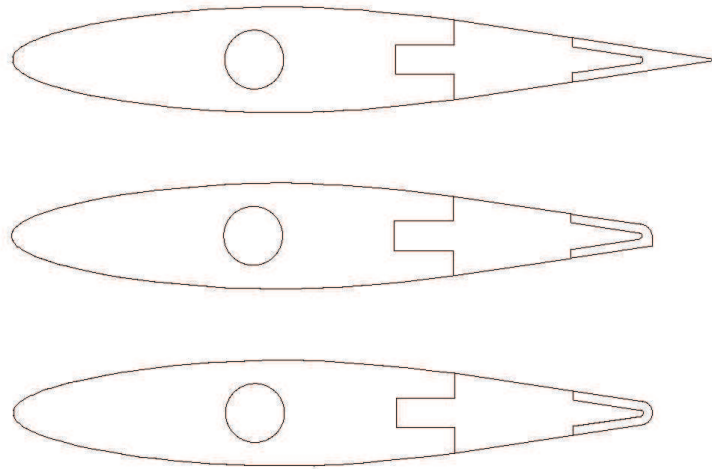


*Figure 4.1: The original and modified versions of NACA64-2-A015 airfoil with sharp, round and half-round trailing-edges.*

negative angles. This is because the carbondom strips on pressure-side are farther from the leading-edge and are earlier covered by the separated flow which results in earlier stall.

In order to ensure a 2D flow and eliminating the tip vortices, 2 circular side plates are used for both sides of the airfoil model. The side plates are made of Plexiglas so that the cameras can look through during the PIV experiments.

## 4.2 Wind tunnel

The wind tunnel utilized for the experiments is the vertical low turbulence tunnel (V-Tunnel) at low speed laboratory, TU Delft which is a high contraction ratio (100 : 1), low turbulence level ( $< 0.1\%$ ), open test section wind tunnel. The tunnel exit diameter where the model is installed is circular with  $0.6m$  diameter and maximum wind speed of  $45m/s$ . The schematic of the tunnel is shown in Figure 4.2.

## 4.3 Plasma actuator facility

The plasma actuator facility consists of the plasma rack and the plasma table; each are separately described below.

### 4.3.1 Plasma actuator racks

Two plasma racks are used in order to supply the high-voltage AC signal of desired shape, peak-to-peak voltage, carrier frequency, pulsation frequency and duty cycle to the plasma actuators. Each rack consists of the following components:

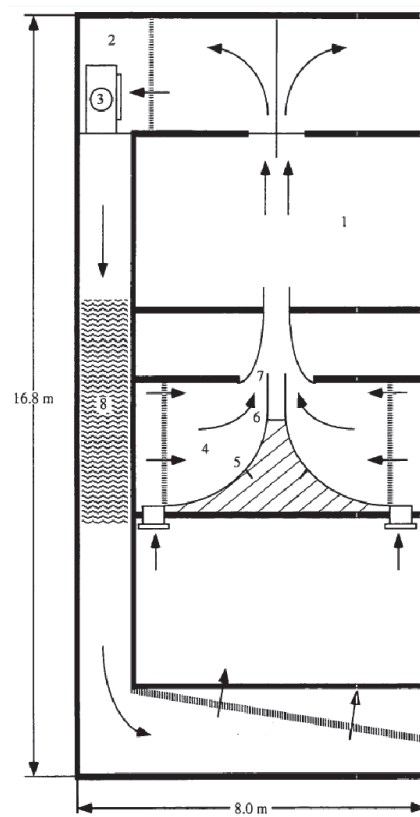


*Figure 4.2:* The schematic of the V-tunnel used in the experiments: 1) measurement room; 2) fan room; 3) fan; 4) settling chamber; 5&6) spikes; 7) contraction; 8) noise suppressor.

- High-voltage amplifier: The amplifiers are TREK 20/20C-HS and TREK 20/20C with maximum  $40kV$  peak-to-peak voltage. The maximum carrier frequency operated during the tests for the maximum voltage is 2000 Hz and the amplifiers are capable of supplying this output. The characteristics of the amplifier are  $\pm 20kV$ ,  $\pm 20mA$ ,  $1000W$ .
- Two National Instruments - Data Acquisition (NI-DAQ) cards
- *LabVIEW* software and the designed control panel

### 4.3.2 Plasma actuator table

The plasma table is used for plasma actuator high-precision force measurements in quiescent airflow. The table consists a set of air bearings which isolates the whole table from the vibrations of the ground.

On the table, an isolation box is used where the plasma actuator is operated inside. The plasma actuator is installed on a plate which is lifted using a NELSON AIR CORP. *RAB1* air bearing in order to ensure minimum friction. The force applied on the plate is measured using a high-precision piezoelectric force sensor.

## 4.4 Force measurement

In order to measure the aerodynamic loads of the airfoil model in the wind tunnel, a force balance was utilized which will be described in this section. Moreover, the calculation method for aerodynamic loads from the load measurements of the balance, the wind tunnel corrections for the open-jet facility and the experimental test matrix are explained.

### 4.4.1 Force sensor

Four one-directional force sensors are employed in the force balance utilized for the aerodynamic force measurements in the wind tunnel. The force sensors are double-bending beam strain-gauge '*KD40S*' sensors from '*ME-Meßsysteme GmbH*' (Figure 4.3). They can measure force withing  $\pm 100N$  with an accuracy of 0.1% and a frequency of  $50kHz$ .



*Figure 4.3: The KD40S force sensor.*

### 4.4.2 Force balance

The force balance (Figure 4.4) consists of an outer rigid frame and an inner flexible frame and 4 strain gauge force sensors. The outer frame is fastened to the wind tunnel body and mounted at the tunnel exit. The inner frame has 2 flexible flat plates and an upper frame. The airfoil model is connected to the upper frame and the upper frame is connected to the lower frame using 3 force sensors ( $V1, V2, V3$ ). The sum of these three forces represent the drag force of the airfoil.

The inner frame is fastened to the outer frame at lower part. The flexible flat plates are assumed to bend freely without friction. Therefore, lift force of the airfoil is directly measured using a force sensor ( $H1$ ) mounted horizontally.

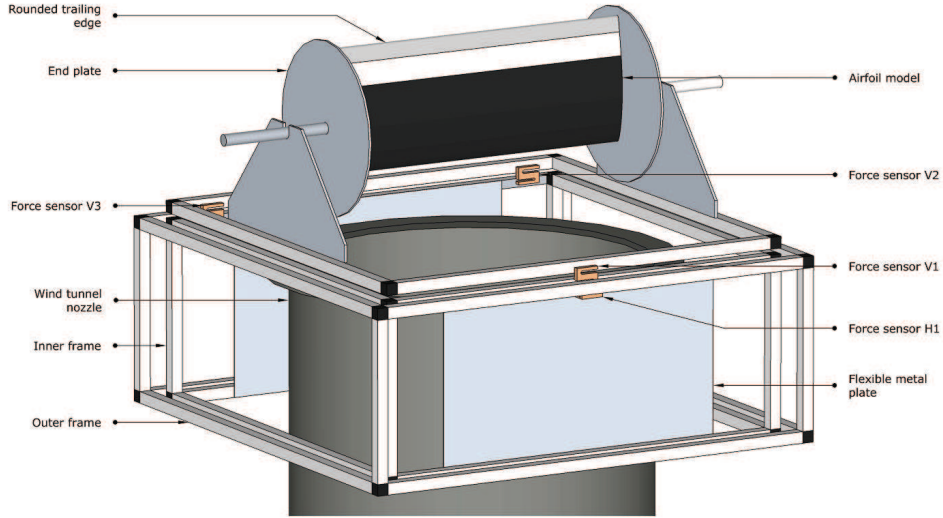


*Figure 4.4:* The schematic of the force measurement balance employed in the experiments [52].

Having said that, the schematic of the forces and moments on the balance from the airfoil and to the sensors are shown in Figure 4.5 and the calculations of lift, drag and moment from the 4 force measurement ( $H1, V1, V2, V3$ ) are as Equation 4.1-Equation 4.3.

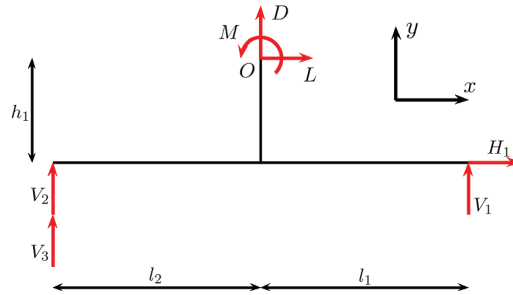


*Figure 4.5:* The schematic of the force and moments applied on the force balance [52].

$$L = -H_1 \quad (4.1)$$

$$D = -(V_1 + V_2 + V_3) \quad (4.2)$$

$$M_O = l_2 \cdot (V_2 + V_3) - h_1 \cdot H_1 - l_1 \cdot V_1 \quad (4.3)$$

where  $L, D, M_O$  are lift, drag and pitching moment around the shaft center ( $O$ ) connecting the airfoil to the force balance, respectively. The distances  $h_1, l_1, l_2$  are as defined in Figure 4.5.

The pitching moment is usually expressed around the quarter chord ( $c/4$ ) which is the aerodynamic center of the airfoil. Therefore, the moment is translated to  $c/4$  as shown in Figure 4.6 and expressed in Equation 4.4

where  $M_{c/4}$ ,  $x$ ,  $\alpha$  are pitching moment about  $c/4$ , distance between  $c/4$  and  $O$  and angle of attach respectively. Lift and drag can be transferred with no change.

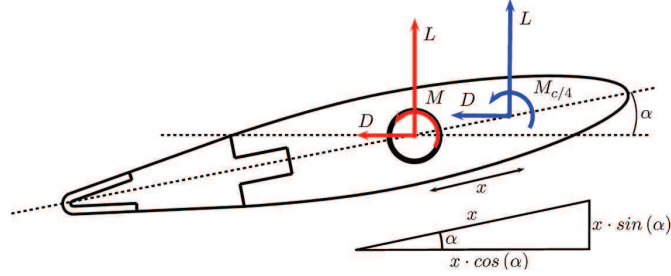


**Figure 4.6:** The schematic of the aerodynamic loads and moments applied on airfoil axis and aerodynamic center [52].

$$M_{c/4} = M_O - x \cdot \sin(\alpha) \cdot D - x \cdot \cos(\alpha) \cdot L \quad (4.4)$$

A correction for the pitching moment is needed due to the static moment as a result of airfoil mass at different angles of attack. This correction is derived experimentally by [52] and is expressed as Equation 4.5 where  $M'_{c/4}$  is corrected pitching moment about  $c/4$ .

$$M'_{c/4} = M_{c/4} - (0.0196\alpha - 0.0045) \quad (4.5)$$

#### 4.4.3 Wind tunnel correction

Aerodynamic force and moment measurements in the wind tunnel require corrections due to several factors which are not present in the real flow application. These effects can be blockage effects due to the presence of the model in walls of the test section (solid blockage) or the wake of the model (wake blockage), change in the slipstream because of the tunnel walls (slipstream curvature) or change in the pressure gradient and velocity due to thickening of the boundary layer on the walls of the tunnel (Horizontal buoyancy effect). The wind tunnel corrections are extensively discussed elsewhere [9].

As flow is free to extend in the test section for open jet wind tunnel, blockage effects are negligible and the only correction required is for slipstream effect. This correction accounts for the fact that the divergence of the slipstream curvature in test section is different from the real flow. This correction is based on the method by Brooks and Marcolini which considers an infinite series of image vortices perpendicular to the chord (shown in Figure 4.7) which induce a reduction in the angle of attack and moment coefficient and an increase in drag coefficient. The corrections are as Equation 4.6-Equation 4.8.

$$\alpha_{cor} = \alpha - \frac{\sqrt{3\sigma}}{\pi} \cdot c_l - \frac{2\sigma}{\pi} \cdot c_l - \frac{\sigma}{\pi} (4c_{m,c/4}) \quad (4.6)$$

$$c_{d,cor} = c_d + \left( \frac{-\sqrt{3\sigma}}{\pi} \cdot c_l \right) \cdot c_l \quad (4.7)$$

$$c_{m,c/4,cor} = c_{m,c/4} - \frac{\sigma}{2} \cdot c_l \quad (4.8)$$

where  $c_l, c_d, c_{m,c/4}$  are measured lift, drag and moment coefficient (about  $c/4$ ),  $\alpha_{cor}, c_{d,cor}, c_{m,c/4,cor}$  are corrected angle of attack, drag and moment coefficient (about  $c/4$ ),  $candh$  are the airfoil chord and the

distance between the model and the first image vortex pair (typically equal to tunnel width) and  $\sigma$  is defined as Equation 4.9.

$$\sigma = \frac{\pi^2}{48} \cdot \left(\frac{c}{h}\right)^2 \tag{4.9}$$

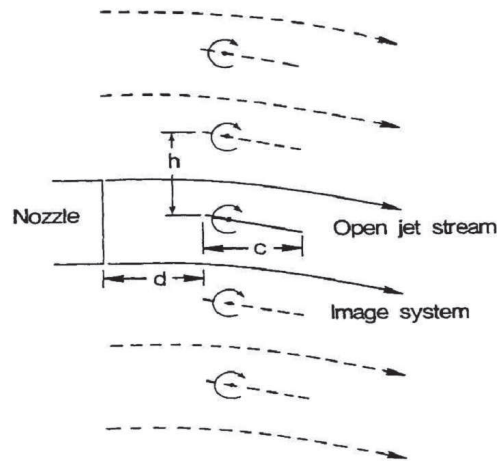


**Figure 4.7:** Vortex image system used for slipstream curvature correction in a 2D open jet test section[12]. The variable 'd' is the distance from the airfoil leading edge to nozzle exit.

As  $\alpha_{cor}$  is a function of  $c_l$ , therefore, slope of the corrected  $c_l - \alpha$  curve will change compared to original as shown in Figure 4.8. The solid lines represent no plasma actuation and dashed line represent plasma actuation.

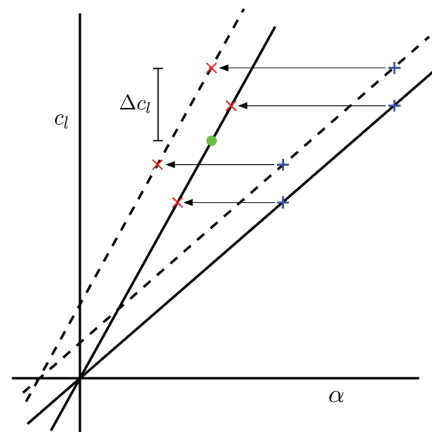


**Figure 4.8:** Illustration of how the correction in angle of attack changes the  $C_L - \alpha$  curve [52].

#### 4.4.4 Test matrix

The force measurements include a series of frequency and voltage study for each trailing shapes and actuation mode. The test matrix is shown in Table 4.2. Then, setting the actuator to an optimum frequency and voltage, a series of polars at different freestream velocities are carried out as detailed in Table 4.3.

**Table 4.2:** Test matrix for the actuator settings experiments.

	$f_c$ study			$V_{pp}$ study	
Free stream velocity ( $U_0$ ) [m/s]	10		15	10	15
Reynolds number (Re) [ $*1e^+3$ ]	40		210	40	210
Angle of attack ( $\alpha$ ) [ $^\circ$ ]	0	7.5	15	0	7.5 15
Waveform		Sine			Sine
Voltage ( $V_{pp}$ ) [kV]		40		20	+2.5 40
Carrier frequency ( $f_c$ ) [Hz]	200	+100	1300		1250
Pulse frequency ( $f_p$ ) [Hz]		0			0
Duty cycle (DC) [%]		100			100
Trailing-edge shapes:		Round		Half-round	Sharp
Actuation mode:		kutta		kutta	tab
		2push		tab	
		Npush		2push	

**Table 4.3:** Test matrix for the main force measurement experiments.

Parameter	Value		
Free stream velocity ( $U_0$ ) [m/s]	10	+5	35
Reynold number (Re) [ $*1e^+3$ ]	140	+70	490
Angle of attack ( $\alpha$ ) [ $^\circ$ ]	-2	+2	18
Waveform		Sine	
Voltage ( $V_{pp}$ ) [kV]		40	
Carrier frequency ( $f_c$ ) [Hz]		1250	
Pulse frequency ( $f_p$ ) [Hz]		0	
Duty cycle (DC) [%]		100	
Trailing-edge shapes:	Round	Half-round	Sharp
Actuation mode:	kutta	kutta	tab
	2push	tab	
	Npush	2push	

The aforementioned actuation modes are different positioning of the electrodes of DBD plasma actuator as shown in Figure 4.9. Actuation modes are designed so that the plasma blowing can either manipulate the kutta condition at trailing-edge (kutta mode), work as a virtual micro-tab (tab mode), work as a combined kutta and tab mode using double DBD plasma actuator (2push mode), or counteract the vortex shedding using double DBD plasma actuator (Npush).

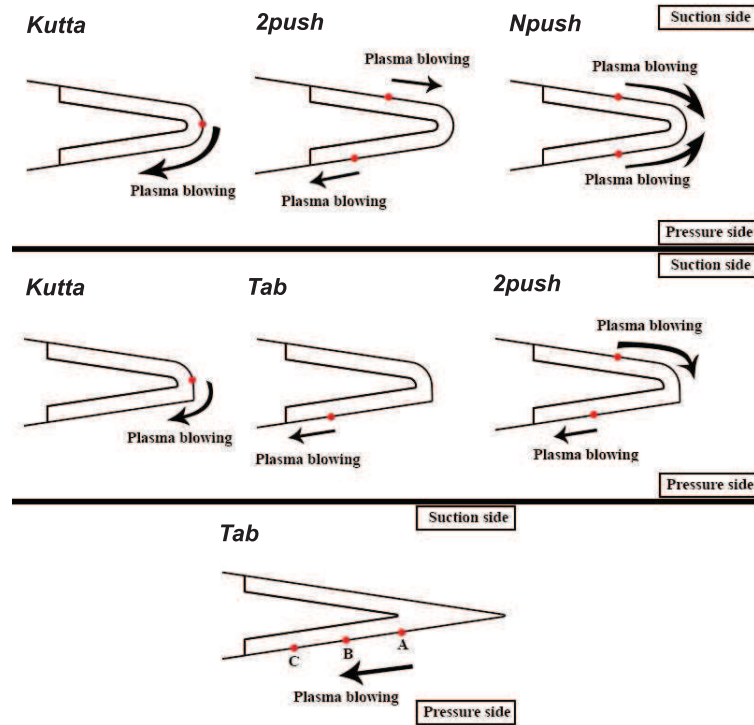


**Figure 4.9:** Actuation modes for different trailing-edge shapes. The position of the plasma onset is shown with a red circle. Three different positions (A,B and C) were investigated for the sharp trailing-edge.

The dimensions and positions of the DBD plasma actuator electrodes for the round (R), half-round (HR) and sharp (SH) are mentioned in Table 4.4-Table 4.6. The relevant parameters  $O_e$ ,  $W_e$ ,  $g$ ,  $pos$ ,  $W_c$ ,  $P/S$ ,  $t_d$ ,  $dir(up/dw)$  are exposed electrode offset from trailing-edge (TE), width of exposed electrode, gap between the electrodes, distance of plasma onset to TE, width of covered electrode, location of plasma actuator (pressure side/suction side), thickness of dielectric and direction of plasma blowing (upstream/downstream) respectively. The subscripts 1, 2 denote the first (positioned on suction side) and second (positioned on pressure side) electrode in case of double electrodes.

## 4.5 Particle Image Velocimetry (PIV)

PIV method is employed in order to study the flow field at the trailing-edge of the airfoil model. In this section, the author has solely described the experimental setup employed during the PIV experiments and for the sake of brevity and general information on PIV method can be studied extensively elsewhere [54, 59].

The flow field at the trailing-edge and the wake of the airfoil is characterized using two-component (planar) PIV. The length of the actuator and the span of the airfoil are chosen long enough to permit a two-dimensional assumption for the flow in the mid-span.

A dual-cavity, FL-pumped, Neodymium-doped yttrium aluminum garnet (Nd:YAG) laser (Quantel CFR PIV-200) with a beam of approximately 7mm diameter, divergence of  $< 3.5mrad$  and wavelength of 532nm

**Table 4.4:** Dimensions and positions of the electrodes for round trailing edge [mm].

TE	Mode	Oe	We	g	pos	Wc	P/S	dir	$t_d$
R	kutta	25	25	0	0	15	-	dw	3
R	2push	$Oe_1$ 25	$We_1$ 10	$g_1$ 0	$pos_1$ 15	$Wc_1$ 10	$P/S_1$ S	$dir_1$ dw	$t_{d1}$ 3
		$Oe_2$ 10	$We_2$ 10	$g_2$ 0	$pos_2$ 20	$Wc_2$ 10	$P/S_2$ P	$dir_2$ up	$t_{d2}$ 3
R	Npush	$Oe_1$ 17.5	$We_1$ 10	$g_1$ 0	$pos_1$ 17.5	$Wc_1$ 25	$P/S_1$ S	$dir_1$ dw	$t_{d1}$ 3
		$Oe_2$ 17.5	$We_2$ 10	$g_2$ 0	$pos_2$ 17.5	$Wc_2$ 25	$P/S_2$ P	$dir_2$ dw	$t_{d2}$ 3

**Table 4.5:** Dimensions and positions of the electrodes for half-round trailing edge [mm].

Shape	Mode	Oe	We	g	pos	Wc	P/S	dir	$t_d$
HR	kutta	29	25	0	4	15	-	dw	3
HR	tab	0	25	0	25	15	P	up	3
HR	2push	$Oe_1$ 31	$We_1$ 10	$g_1$ 0	$pos_1$ 21	$Wc_1$ 15	$P/S_1$ S	$dir_1$ dw	$t_{d1}$ 3
		$Oe_2$ 9	$We_2$ 10	$g_2$ 0	$pos_2$ 19	$Wc_2$ 10	$P/S_2$ P	$dir_2$ up	$t_{d2}$ 3

**Table 4.6:** Dimensions and positions of the electrodes for sharp trailing edge [mm].

	Shape	Mode	Oe	We	g	pos	Wc	P/S	dir	$t_d$
A	SH	tab	0	25	0	25	15	P	up	3
B	SH	tab	5	25	0	30	15	P	up	3
C	SH	tab	10	25	0	35	15	P	up	3

is used to make laser sheet of  $2\text{mm}$  thickness, having the beam passed through three optical lenses, i.e. Spherical divergent, Spherical convergent and Cylindrical convergent with focal-lengths  $-50\text{mm}$ ,  $+80\text{mm}$  and  $+60\text{mm}$  respectively. The maximum pulse energy of the laser is  $200\text{mJ}$  at  $25\text{Hz}$  with a pulse width of  $9\text{ns}$  at  $180\text{mJ}$ .

A LaVision GmbH Image Intenser camera with a 12-bit sensor of  $1376 \times 1040$  pixels and a pixel size of  $6.45\mu\text{m}$  is used to record images at a frame repetition rate of  $4.6\text{Hz}$  in double-frame mode using a programmable timing unit (PTU).

A Nikon lens with a focal length of  $60\text{mm}$  and  $f\#$  of 5.6 is employed and the magnification ratios are 0.08 and 0.045 for the two acquired fields of view (FOV). The FOVs are  $11\text{cm} \times 8\text{cm}$  and  $23\text{cm} \times 18\text{cm}$  with details in Table 4.7.

The time delays between the two frames are  $100\mu\text{s}$  and  $200\mu\text{s}$  for freestream velocities of 10 and  $20\text{m/s}$  respectively. Each dataset consists of 300 double-frame images which corresponds to  $65.2\text{s}$  recording time.

**Table 4.7:** FOV of the camera for different trailing-edge shapes.

Trailing-edge		FOV	
Round	$11\text{cm} \times 8\text{cm}$	$0.87 \leq x/c \leq 1.33$	$-0.12 \leq y/c \leq 0.21$
Half-round	$11\text{cm} \times 8\text{cm}$	$0.83 \leq x/c \leq 1.29$	$-0.17 \leq y/c \leq 0.17$
Sharp	$11\text{cm} \times 8\text{cm}$	$0.79 \leq x/c \leq 1.25$	$-0.15 \leq y/c \leq 0.19$
Sharp	$23\text{cm} \times 18\text{cm}$	$0.48 \leq x/c \leq 1.43$	$-0.42 \leq y/c \leq 0.33$

The equipment used for PIV include fox generator, laser, cameras, programmable timing unit (PTU) and the optical lenses which are described in Table 4.8. The laser and optics are adjusted to ensure that the thickness of the laser sheet is approximately  $2\text{mm}$  and the intensity of the laser beam in FOV is adequate. The schematic showing the arrangement of the laser and the laser is shown in Figure 4.10.

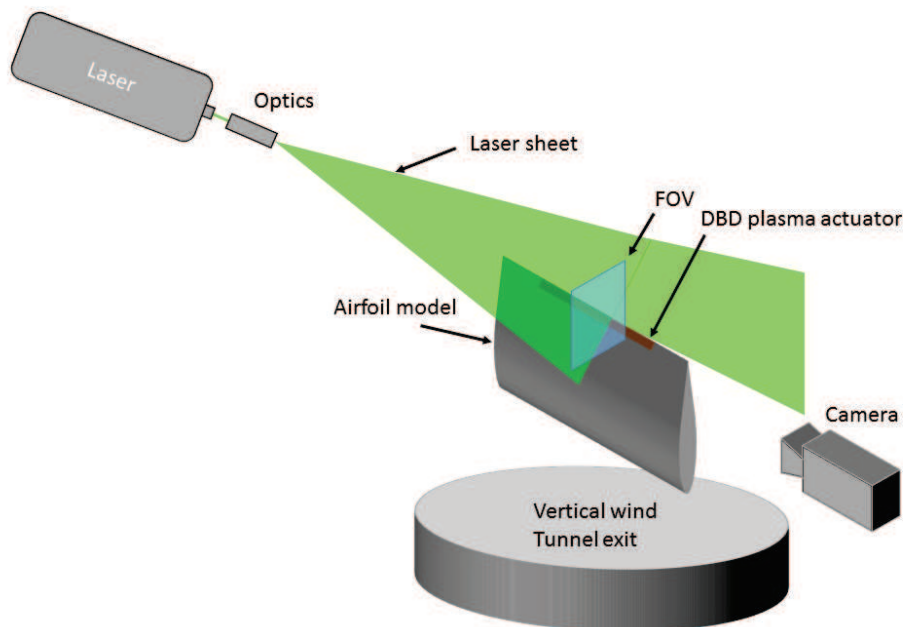


**Figure 4.10:** Illustration of arrangement of laser, camera and optics for the PIV experiments.

The software employed for the processing of PIV image pairs is 'DAVIS 8' from 'LaVision GmbH'. The

**Table 4.8:** PIV hardware employed in the tests.

Hardware 1	Fox generator
Model	SAFEX Fog 2010+
Tracer particles	non-toxic dyethylene-glycol/water based
Droplet size	1 $\mu$ m
Power	1650 W
Hardware 2	Laser
Model	Quantel CFR PIV-200
Type	Nd:YAG FL-pumped dual-cavity
Beam wavelength	532nm
Max energy per pulse	200mJ
Max pulse frequency	25Hz
Pulse width at 180mJ	9ns
Beam diameter	7mm
Beam divergence	$\pm$ 3.5mrad
Hardware 3	Camera
Model	LaVision Image Intenser
Sensor	1376x1040, 12bit
Pixel size	6.45x6.45 $\mu$ m
Max double-frame rate	5 Hz
Hardware 4	Programmable timing unit (PTU)
Model	LaVision
Hardware 5	Optical lenses
Model	Dantec
Lens 1	Spherical divergent: -50 mm
Lens 2	Spherical convergent: +80 mm
Lens 3	Cylindrical convergent: +60 mm

method used for vector field computation is the iterative multi-grid image deformation technique (Scarano and Riethmuller). The size of the interrogation window employed is  $16 \times 16$  with 50% overlap resulting in a spatial vector resolution of 0.8 vector/mm. The spatial vector resolution for wide FOVs is 0.4 vector/mm.

### 4.5.1 Test matrix

The PIV experiments include a series of tests for selected actuation modes and angles of attack for the three trailing-edge shapes. The test matrix for PIV experiments and the parameters of the PIV setup are described in Table 4.9 and Table 4.10.

**Table 4.9:** Test matrix for the PIV experiments.

Parameter	Value		
Free stream velocity ( $U_0$ )	10	20	
Reynold number ( $*1e + 3$ )	140	280	
Waveform	Sine		
Voltage ( $V_{pp}$ ) [kV]	40		
Carrier frequency ( $f_c$ ) [Hz]	1250		
Pulse frequency ( $f_p$ ) [Hz]	0		
Duty cycle (DC) [%]	100		
Trailing-edge shapes	Round	Half-round	Sharp
Actuation mode	kutta	kutta	tab
		tab	(position A)
		2push	

**Table 4.10:** PIV setup parameters for the experiments.

Parameter	Value	
FOV [mm x mm]	$110 \times 80$	$230 \times 180$
Aperture f#	5.6	
Recording rate [Hz]	4.6	
Recording time [s]	65.2	
Method	Double-frame	
Pulse delay [s]	100	200
Digital resolution [pix/mm]	12.5	5.98
Magnification (M)	0.08	0.045
Interrogation window IW ( $x \times y$ )	$16 \times 16 \text{ pix}^2$	$1.27 \times 1.23 \text{ mm}^2$
		$2.67 \times 2.76 \text{ mm}^2$
IW Overlap	75%	
Vector per field	$86 \times 65$	
Vector per mm	0.78	0.35

## 4.6 Power measurement

In order to find a practical flow control application for DBD plasma actuators on any aerodynamic device, it is important to measure the power consumption of the actuator. Due to the fact that the actuator's low-amplitude low-frequency discharge is composed of many high-amplitude high-frequency micro-discharges, therefore it is practically difficult to measure the power directly with a reasonable precision. The method utilized to measure this parameter is described in this section.

### 4.6.1 Integrated capacitor method

This method is developed by [3] in order to find the time-averaged power consumption of a DBD plasma actuator ( $\overline{P}_a$ ). It is based on placing a capacitor with a known capacitance ( $C_m$ ) in series between the actuator covered electrode and ground cable to the amplifier (shown in Figure 4.11) and measuring the voltage applied on the capacitor ( $V_m$ ).

The capacitance is chosen high enough compared to capacitance of DBD plasma actuator without plasma discharge ('cold' capacitance) so that the capacitor voltage is within  $\pm 10V$  and easily readable by an oscilloscope. Typical values from the literature [3] are  $10 - 330nF$ . In this work, a capacitance of  $150nF$  gave satisfactory results and was utilized in all tests.

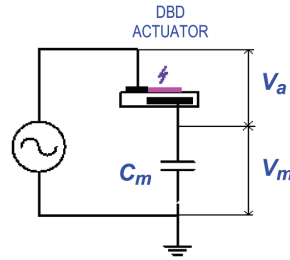


Figure 4.11: Schematic of the electric circuit of the integrated capacitor method [3].

Knowing  $V_m$  and  $C_m$ , the charge on the capacitor ( $Q_m$ ) and current through the capacitor ( $I_m$ ) is known from Equation 4.10-Equation 4.11.

$$Q_m(t) = C_m \cdot V_m(t) \quad (4.10)$$

$$I_m(t) = C_m \frac{dV_m(t)}{dt} \quad (4.11)$$

As capacitor is in series with the actuator, current passing through the capacitor is equal to the current passing through the actuator ( $I_m = I_a$ ). Therefore, the instantaneous power consumption will be Equation 4.12 and the average power consumption over a time period of  $T$  will be Equation 4.13.

$$P_a(t) = V_a(t) \cdot I_a(t) = V_a(t) \cdot C_m \frac{dV_m(t)}{dt} \quad (4.12)$$

$$\overline{P}_a = \frac{1}{T} \int_0^T V_a(t) \cdot C_m \frac{dV_m(t)}{dt} dt = \frac{1}{T} \int V_a \cdot C_m dV_m = \oint_n V_a dQ_m \quad (4.13)$$

where  $t$  is the time and  $n$  is the number of AC cycles. Typically, setting  $n = 1$  will result in the power consumption averaged over 1 AC cycle of the actuator.

Plotting the instantaneous capacitor charge ( $Q_m$ ) versus actuator applied voltage ( $V_a$ ) yields to a so-called 'Lissajous curve' ( $Q_m - V_a$ ) and from the Equation 4.13 it is known that the area inside this curve divided by the AC cycle period will result in  $\overline{P}_a$ .

In this work, in order to measure power consumption with better accuracy, 10,000 cycles are plotted in the Lissajous curve and using a 'least-square fit' method, a curve is fitted over all data points and  $\overline{P}_a$  is calculated based on the fitted line.

### 4.6.2 Test matrix

A series of power measurements were carried out using the integrated capacitor method for a wide range of applied voltage and frequency and for 3 different dielectric thicknesses as described in Table 4.11.

**Table 4.11:** *The test matrix for the power measurement experiments.*

Parameter	Value		
Free stream velocity ( $U_0$ )	0		
Waveform	Sine		
Voltage ( $V_{pp}$ ) [kV]	20	+2.5	40
Carrier frequency ( $f_c$ ) [Hz]	100	+100	2000
Pulse frequency ( $f_p$ ) [Hz]	0		
Duty cycle (DC) [%]	100		
Dielectric thickness [mm]	1	2	3
Exposed electrode width [mm]	25		
Covered electrode width [mm]	15		



# Results and discussion

This chapter provides the results and discussion for three set of experiments which together are aimed to provide an understanding on how and to what extent DBD plasma actuator can control the aerodynamic loads.

The first set of experiments is aimed to identify the electromechanical performance of the actuator, i.e. the reaction force and consumed electrical power for the actuator in quiescent flow conditions.

The second series investigates the potential of the actuator for load control through the aerodynamic force measurements for three different trailing-edge shapes and several modes of actuation.

The final set of experiments studies the flow topology for selected cases (from force measurements) where the load control has been promising in order to provide an insight on how the actuator is changing the flow behavior.

### 5.1 Quiescent-flow force measurements

The first set of experiments include high-precision reaction force measurement in quiescent flow conditions where the plasma actuator is mounted on a flat plate and the flat plate is mounted on a high-precision force sensor inside an isolation plate on plasma table as described in subsection 4.3.2.

The experiments were intended to measure the total body force produced by the DBD plasma actuator for various applied voltage, carrier frequency and dielectric thicknesses. The results were to be used to calculate the momentum coefficient ( $c_\mu$ ) of the actuator in addition to calibrate a plasma model aimed to calculate the body force distribution of the actuator. The plasma model is to be developed as an extra objective of this thesis in case time allows.

Equation 5.1 shows the equation for the actuator momentum coefficient where  $J$  is the total momentum of the induced jet of the actuator in quiescent flow,  $q_\infty$  is the dynamic pressure of the freestream flow and  $c$  is airfoil chord.

$$c_\mu = \frac{J}{q_\infty c} \quad (5.1)$$

$J$  can either be calculated from velocity measurements employing the integral of wall-normal plasma jet profile (Equation 5.2) or from the direct force measurements of the actuator where  $J$  will be the force of the actuator. The latter method is used in the current research.

$$J = \int_0^{\infty} \rho u^2 dy \quad (5.2)$$

The variations of actuator force with carrier frequency is shown in Figure 5.1. Two important points which is inferred from the figure are: 1) actuator force linearly increases with carrier frequency up to a point; 2) there is an optimum frequency where the force is the highest.

Increasing the frequency simply means higher number of discharges per unit time. As force is averaged over time, therefore increasing the frequency results in larger averaged force. The optimum frequency is a function of dielectric properties and has a direction relation with dielectric constant ( $\epsilon$ ) and inverse relation with dielectric thickness ( $t_d$ ). It is seen in Figure 5.1 that the optimum frequency reduces with  $t_d$ . The same trend is repeatedly observed in the literature [39, 18, 49, 32]

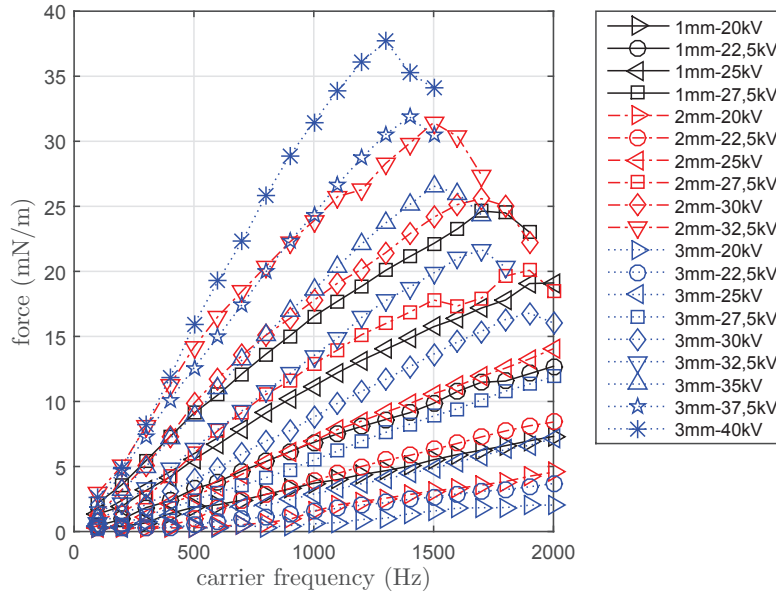


**Figure 5.1:** Variations of force with carrier frequency for various applied voltages and dielectric thicknesses.

[22] found that the actuator force increases with  $V_{AC}^{3.5}$ . The same trend is also observed in Figure 5.2 where the actuator force as a function of the applied voltage is shown. It is worth noting that the applied voltage is peak-to-peak and is two times the  $V_{AC}$ . The increase in the actuator force with applied voltage is due to higher potential, larger electric field and higher degree of ionization.

The actuator force can be expressed as Equation 5.3 [33] where  $\rho_c$  is charge density in  $C \cdot m^{-3}$  in three-dimensional,  $E$  is total electric field in  $N \cdot C^{-1}$  as a result of electrode potential and local plasma charge and  $f$  is force per unit volume in  $N \cdot m^{-3}$ .

$$f = \rho_c \cdot E \quad (5.3)$$

The effect of dielectric material on actuator force is shown in Figure 5.3. It is seen that the actuator force decreases with increasing the dielectric thickness. This is because increasing the dielectric thickness will result in larger distance between the exposed and covered electrodes and consequently weaker electric field and lower force.

The actuator force measurements are used to calculate the momentum coefficient using Equation 5.1 for the actuator at different freestream velocities and the variations of  $c_\mu$  as a function of carrier frequency and

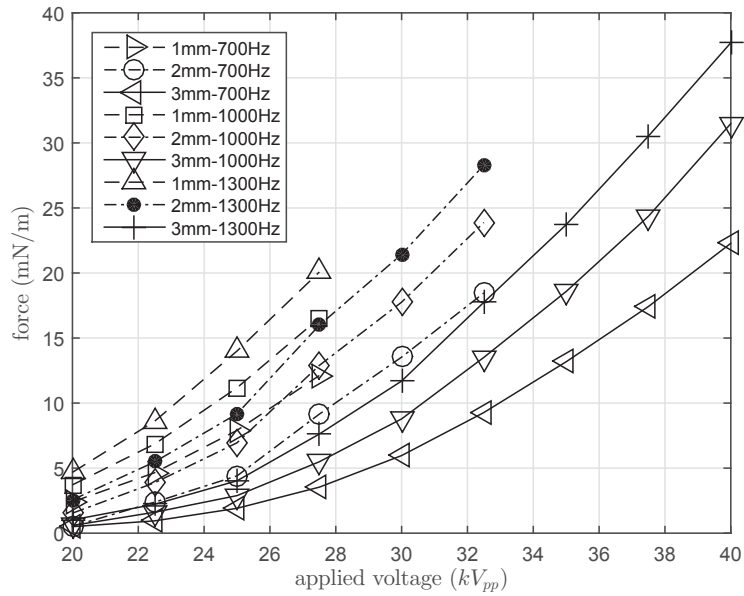


Figure 5.2: Variations of force with applied voltage for various carrier frequencies and dielectric thicknesses.

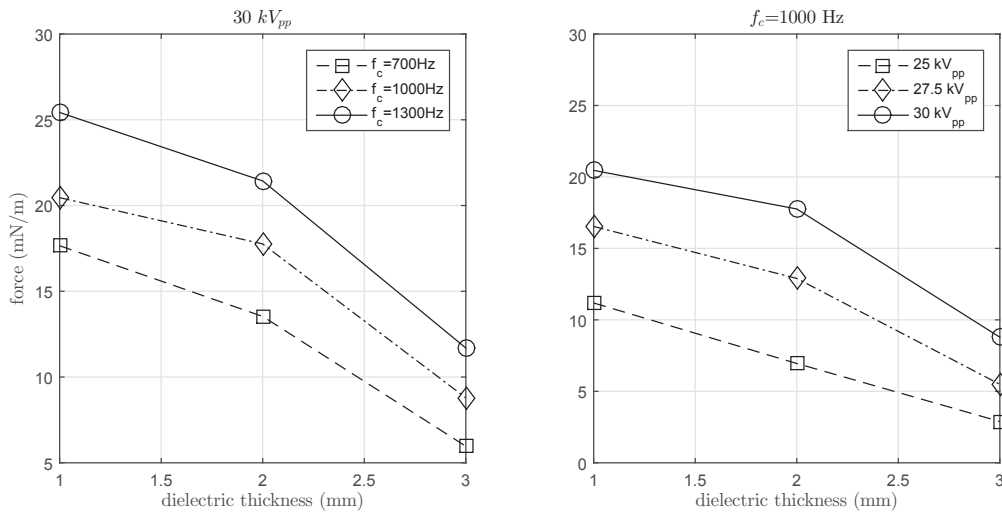
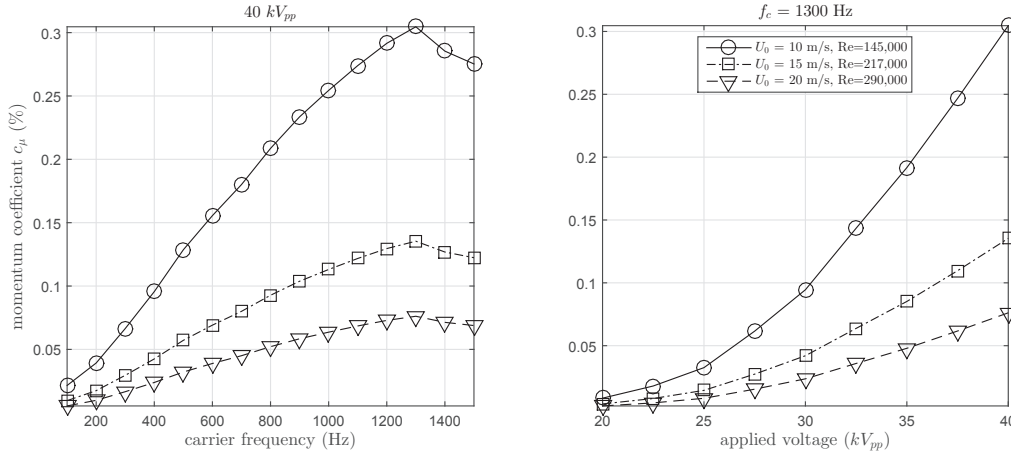
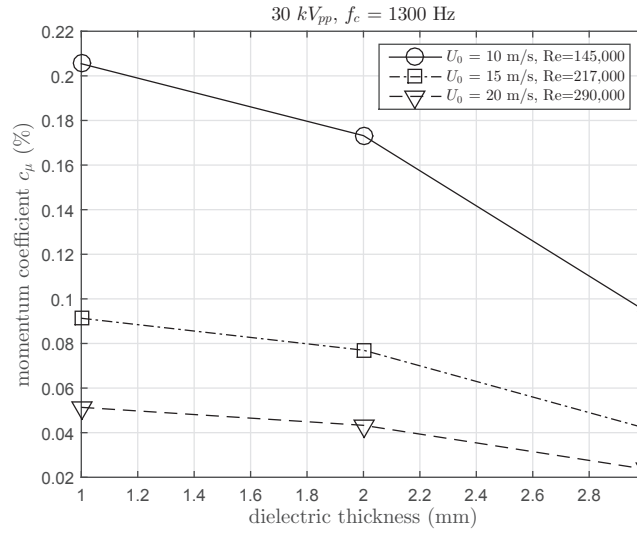


Figure 5.3: Variations of force with dielectric thickness for various applied voltages and carrier frequency.

applied voltage are shown in Figure 5.4 and as a function of dielectric thickness is shown in Figure 5.5. The same trend as the force is observed for  $c_\mu$  as expected from the equation.



**Figure 5.4:** Momentum coefficient ( $c_\mu$ ) as a function of applied voltages and carrier frequency.



**Figure 5.5:** Momentum coefficient ( $c_\mu$ ) as a function of dielectric thickness.

## 5.2 Aerodynamic loads and PIV flow field measurements

The second and third set of experiments include wind tunnel force measurements and PIV study for three different trailing-edge shapes with various actuation modes. The experiments are intended to investigate the potential of the actuator for aerodynamic load control via circulation control and study how the actuator is changing the flow pattern and wake topology.

The aerodynamic forces and pitching moment for the airfoil model are measured using the force balance described in section 4.4. The studies conducted are on variations of coefficients of lift, drag and pitching moment as a function of actuator settings (i.e. carrier frequency, applied voltage, pulsation frequency and

duty cycle), angle of attack, freestream velocity (Reynolds number), trailing-edge shape and actuation mode which are each described in this section.

The PIV flow measurements were carried out using the setup explained in section 4.5 for a selection of cases from promising force measurement results.

### 5.2.1 $c_l$ as a function of actuator settings

The first set of wind tunnel experiments investigated the variations of lift coefficient for the three geometries as a function of the actuator settings, i.e. applied voltage, carrier frequency, pulsation frequency and duty cycle, in order to choose the optimum settings for the load control experiments.

#### 5.2.1.1 Carrier frequency and applied voltage

The effect of carrier frequency and applied voltage on  $\Delta c_l$  for the round, half-round and sharp trailing-edges, angles of attack and freestream velocities are shown in Figure 5.6, Figure 5.7 and Figure 5.8.

As discussed in section 5.1, it is expected that the actuator force and consequently the amount of change in lift coefficient produced by the actuator will increase with both carrier frequency and applied voltage, however, there are two points to mention: 1) the effect of applied voltage is much stronger than the carrier frequency; 2) there will be an optimum for the carrier frequency when the highest force is produced. This trend is visible for the three trailing-edge shapes.

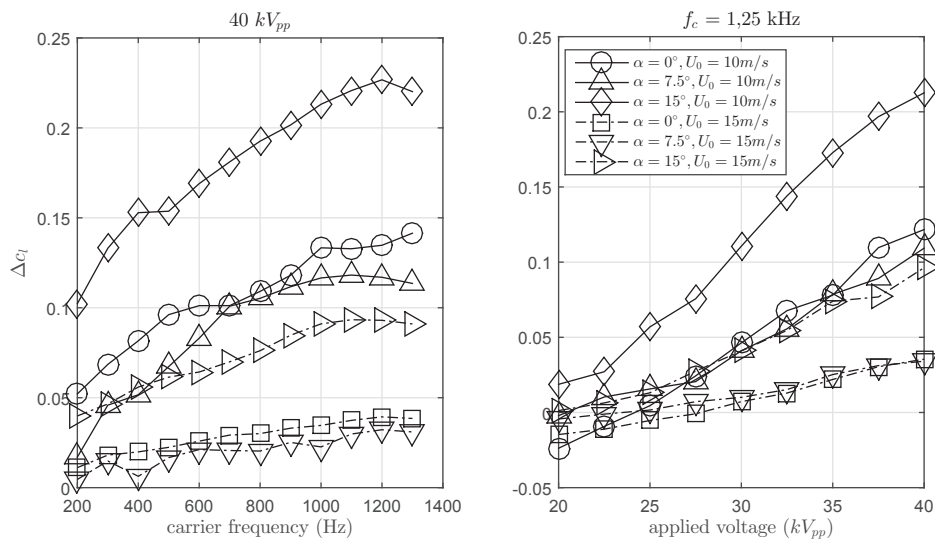


**Figure 5.6:** Variations of lift coefficient (per unit length of the actuator) as a function of carrier frequency (left) and applied voltage (right) for the round trailing edge. The actuator is positioned at centerline of the trailing-edge (Kutta mode).

The actuator effect reduces as the freestream velocity increases from 10 to 15 m/s. This can be justified by the reduction in momentum coefficient of the actuator from 0.3 to 0.13.

Based on these series of test, the applied voltage and carrier frequency of 40 kV<sub>pp</sub> and 1250 Hz has been used for all the load control experiments unless mentioned.

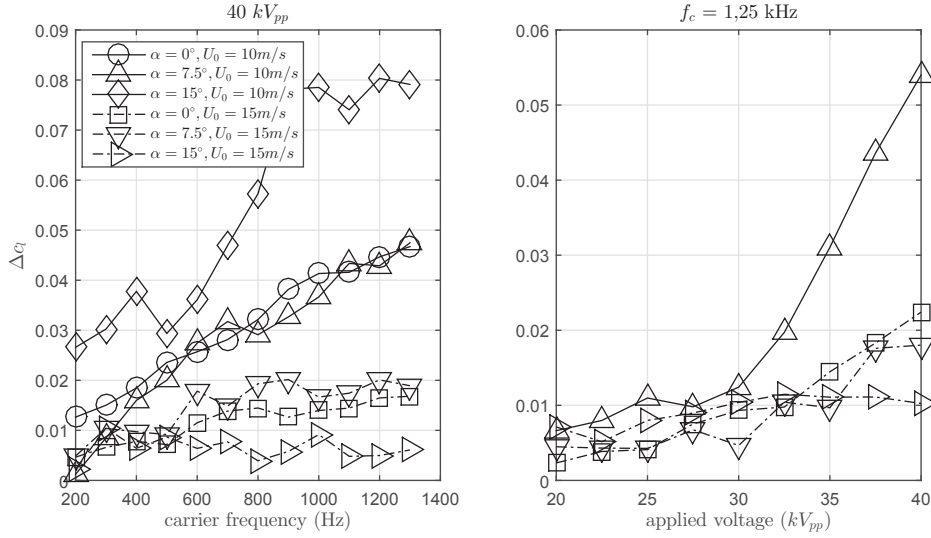


**Figure 5.7:** Variations of lift coefficient (per unit length of the actuator) as a function of carrier frequency (left) and applied voltage (right) for the half-round trailing edge. The actuator is positioned at centerline of the trailing-edge (Kutta mode).

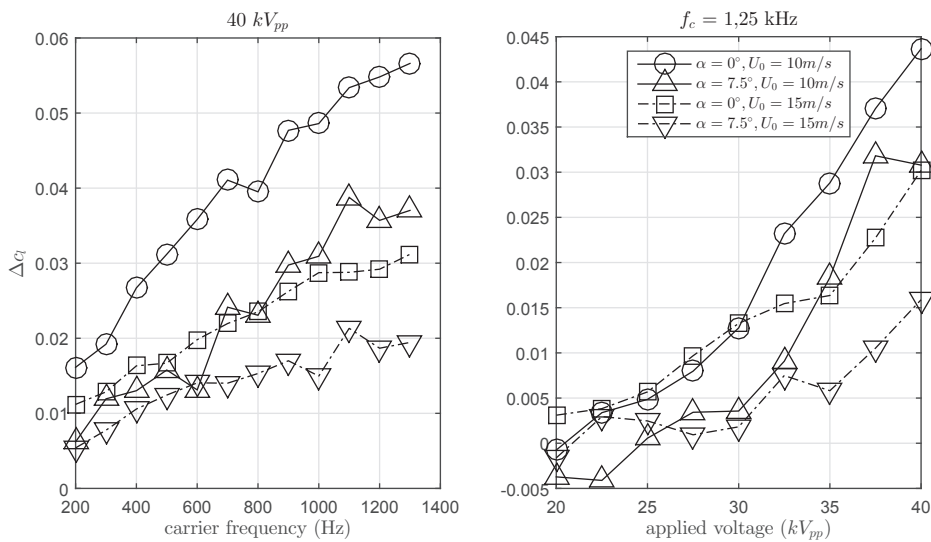


**Figure 5.8:** Variations of lift coefficient (per unit length of the actuator) as a function of carrier frequency (left) and applied voltage (right) for the sharp trailing edge. The actuator is positioned as a tab (position A).

### 5.2.1.2 Pulsation frequency and duty cycle

Generally the force of the actuator oscillated with carrier frequency of the actuator. Moreover, using a modulated operation with a pulsation frequency applied, the produced force can be forced to oscillate with another frequency as well. A study was conducted in order to find any correlation between the pulsation (modulation) frequency and the  $\Delta c_l$ . However, the results could not show any effect as shown in Figure 5.9-top.

On the other hand, variations of duty cycle of the actuator can expectedly change the force magnitude and  $\Delta c_l$  ( Figure 5.9-bottom). This is simply because lower duty cycle means the actuator is operating less portion of time during each cycle and therefore, produces less total force in unit time.

This is also the reason that the modulated actuator operating at 50% duty cycle produces less force than the actuator with no pulsation and 100% duty cycle (dashed line in Figure 5.9-top).

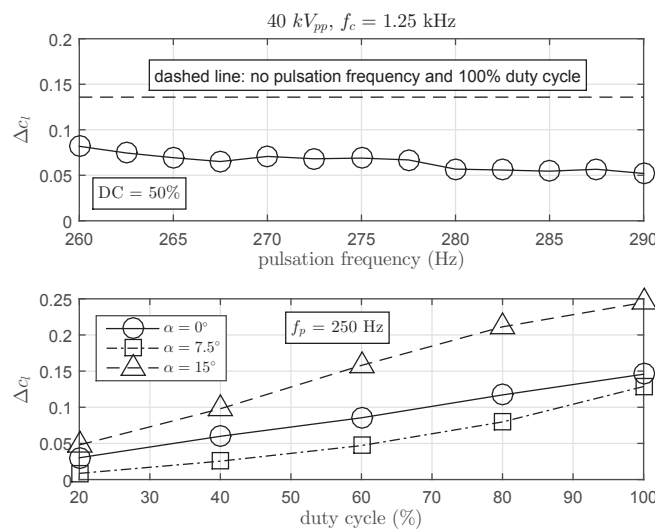


**Figure 5.9:** Variations of lift coefficient (per unit length of the actuator) as a function of pulsation frequency (top) and duty cycle (bottom) for the round trailing edge. The actuator is positioned at centerline of the trailing-edge (Kutta mode).

## 5.2.2 Round trailing-edge

Round trailing-edge airfoil is the first model for the experiments. The main reason for this selection is that this shape has a blunt trailing-edge, therefore, there will be significant vortex shedding at the trailing-edge. This enables the actuation system to have the potential to manipulate the vortical structure, manipulates the Kutta condition and change the position of the trailing-edge stagnation point and consequently the circulation around the airfoil.

The actuators are installed on 3 different positions enabling 3 different actuation modes, i.e. Kutta, 2push and Npush. The first two modes are meant to control the airfoil circulation using one and two actuators respectively. The latter will use double actuators blowing downstream and in opposing configuration synchronized with vortex shedding frequency and meant to counteract the vortex shedding. The actuation modes are described in subsection 4.4.4.

### 5.2.2.1 Kutta mode

**Aerodynamic loads and moments:** Promising results from previous research [39, 52] for manipulation of Kutta condition at the round trailing-edge with the actuator setting of  $35 \text{ kV}_{pp}$  encouraged further research with the aid of a new high-voltage amplifier that could operate the actuator up to  $40 \text{ kV}_{pp}$ .

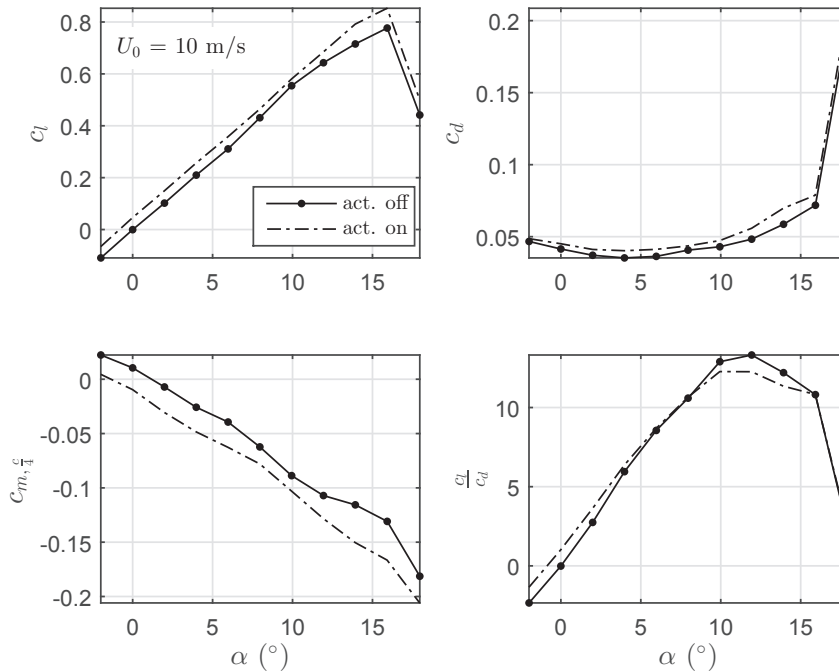
At this operation mode, the plasma is blowing at the centerline of the trailing-edge blowing towards either pressure side or suction side as specified in the results.

Figure 5.10 shows the polars for the round trailing-edge at freestream velocity of  $10 \text{ m/s}$  with and without the plasma actuation where plasma is blowing towards the pressure side. It is seen that the plasma blowing can effectively increase the lift over the whole range of angle of attack from  $-2.18^\circ$  where the effect is almost constant from  $-2.6^\circ$ , then reduces within the range from  $6.12^\circ$  and again increases to its maximum amount just before the  $c_{l,max}$ . The effect is negligible after stall where the flow is fully separated at the trailing-edge and plasma blowing will be ineffective.

The lift increase is due to change in Kutta condition and adding a virtual camber and consequently inducing higher circulation by the airfoil to the flow. This is observable from the mean velocity field from the PIV results presented later in this section.

Regarding the change in drag, the actuator induces almost a constant increase in drag where the value is slightly higher just before the  $c_{l,max}$ . This is due to introduction of the additional camber as a result of the blowing which will deflect the flow at the wake, therefore, introducing larger front area to the flow and increasing form drag.

The Kutta mode plasma blowing will improve aerodynamic efficiency of the airfoil within  $-2.6^\circ$  by increasing the  $c_l/c_d$ . However, it reduces onwards to stall.



**Figure 5.10:** Lift, drag and moment coefficient as a function of angle of attack for the round trailing edge. The actuator is positioned at centerline of the trailing-edge (Kutta mode). ( $c_\mu = 0.3\%$ ,  $Re = 145,000$ )

The same effect but to a lower magnitude is also seen at higher freestream velocities, however, for the sake of brevity the polars for all geometries and actuation modes are only presented for  $U_0 = 10 \text{ m/s}$  and instead

$\Delta c_l - \alpha$  plot which represents the change in loads as a result of plasma blowing is presented for all tested freestream velocities. It is believed to be informative enough. The  $\Delta c_l - \alpha$  plot for the current case is shown in Figure 5.11.

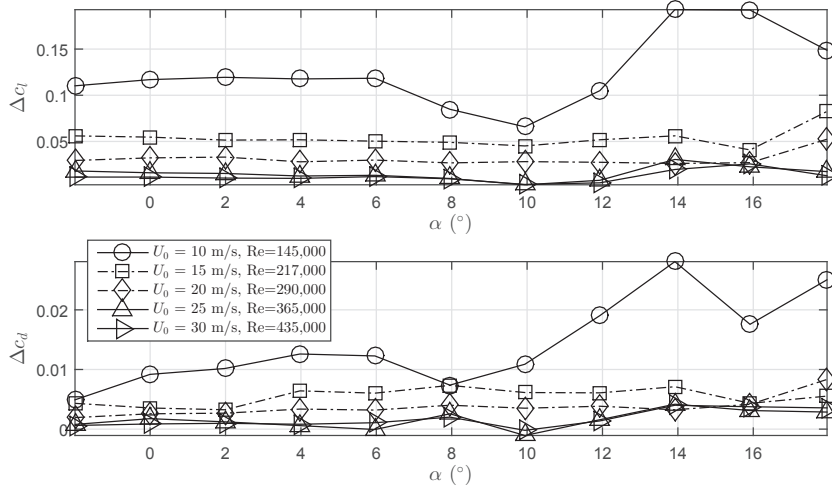


**Figure 5.11:** Variations of lift coefficient (per unit length of the actuator) relative to baseline as a function of freestream velocity and angle of attack for the round trailing-edge. The actuator is positioned at centerline of the trailing-edge blowing towards pressure side (Kutta mode).

It is seen that the actuator can guarantee a  $\Delta c_l$  of 0.12 for a wide range of angle of attack at freestream velocity of  $10\text{m/s}$  and Reynolds number of 145,000. This value reduces to 0.07 between  $6..12^\circ$  and jumps to 0.2 at  $14..16^\circ$  which is just before the  $c_{l,max}$ .

The same effect but to a lower magnitude is experienced by increasing the freestream velocity. It is a result of the reduction in the momentum coefficient of the actuator. The  $\Delta c_l$  of 0.06 and 0.03 are the average values for 15 and  $20\text{m/s}$  freestream velocities.

A very interesting finding is shown in Figure 5.12 where the lift coefficient can be controlled within 0.3 by changing the direction of plasma blowing from pressure side towards the suction side. Therefore, the Kutta mode can control the lift coefficient within  $\pm 0.15$  for opposite plasma blowing directions.

More interestingly, plasma blowing towards suction side can more effectively control the loads while it reduces the lift coefficient for 0.25 just before the  $c_{l,max}$ . This can be of great importance for load alleviation on stall-regulated wind turbines which operate at high angles of attack near stall and suffer from high loads in this range.

**Time average velocity field and streamlines:** In order to understand how the actuator is changing the flow pattern, time average velocity vector fields ( $U_0$ ) for plasma blowing to pressure side are shown in Figure 5.13. The left column corresponds to the actuator off and the right column corresponds to the actuator on. The plots correspond to angles of attack  $0^\circ, 5^\circ, 10^\circ, 14^\circ$  which are shown on each figure.

As a result of the blunt round trailing-edge of the airfoil, there is a notable wake behind the airfoil trailing-edge. This is most observed from the top-left contour corresponding to actuator off at  $0^\circ$ .

The most prominent effect of the plasma actuation in the flow is the downward-deflection of the wake. This is observed for all the tested angles of attack as shown in Figure 5.14. The angle of the downward-deflection (shown in Figure 5.15) caused by the actuator corresponds well with the magnitude of  $\Delta c_l$ . The highest deflection angle is observed at  $14^\circ$  where the highest  $\Delta c_l$  is also seen in Figure 5.11 and the lowest deflection angle is observed at  $10^\circ$  where the lowest  $\Delta c_l$  is observed in Figure 5.11.

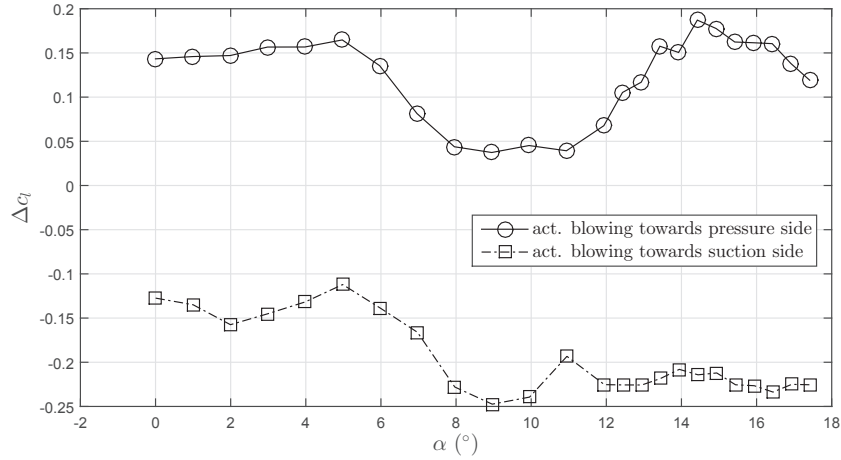


**Figure 5.12:** Variations of lift coefficient (per unit length of the actuator) relative to baseline as a function of freestream velocity and angle of attack for the round trailing-edge. The actuator is positioned at centerline of the trailing-edge blowing towards either pressure side or suction side.

Moreover, as a result of the plasma blowing there is a region of back flow towards the pressure-side. This effect becomes more prominent as the angle of attack increases.

In order to further clarify the flow topology under plasma actuation, the flow streamlines for  $U_0 = 10m/s$  are shown in Figure 5.16. From the images it is seen that the saddle point (defined as the point with minimum absolute velocity) moves with the plasma actuation.

The overall understanding of the velocity field confirms the change in position of the stagnation point at the trailing-edge and manipulates the Kutta condition.

Figure 5.17 shows the average velocity vector fields for plasma blowing to suction side for  $0^\circ, 5^\circ, 14^\circ, 16^\circ$ . The angles are shown in negative corresponding to having the suction side at the bottom for this image.

It is clearly seen that blowing towards the suction side reduces the lift coefficient by promoting the flow separation and creating a back flow region at the trailing-edge. This is also observed from the streamlines shown in Figure 5.18. At lower angles of attack, the trailing-edge vortical structure grows in length scale and correspondingly energy and at higher angles of attack a large separation bubble is created as a result of plasma blowing upstream.

**Mean turbulent kinetic energy:** As the actuator is intended for unsteady load control applications, in addition to the averaged field, fluctuations of the velocity under plasma actuation also need to be studied. Turbulent kinetic energy (TKE) is a measure of the energy of the vortical structures in the flow and can be used to investigate how the energy of the fluctuations in the wake is changed when plasma actuation is used. Additionally, higher TKE also represent higher turbulent mixing in the flow.

The contours of the TKE for the round trailing-edge are shown in Figure 5.19 and Figure 5.20. The position of the actuator gap (the plasma onset) is shown with a while circle. For both cases, the plasma is blowing from top to bottom of the image, making it towards pressure side for Figure 5.19 and towards suction side for Figure 5.20.

It is seen that when plasma is blowing to pressure side, it greatly enhances the energy of the vortical structures in the wake and the turbulent mixing near the trailing-edge. This is slightly seen at  $0^\circ$  angle of attack but is much more prominent at higher angle of attack, i.e.  $14^\circ$  as shown. Moreover, deflection of the wake as a result of the plasma blowing is also observed again.

When the plasma is blowing to suction side, it is seen that a separation region containing vortical structures with higher TKE is created which results in loss of lift observed in force measurements.

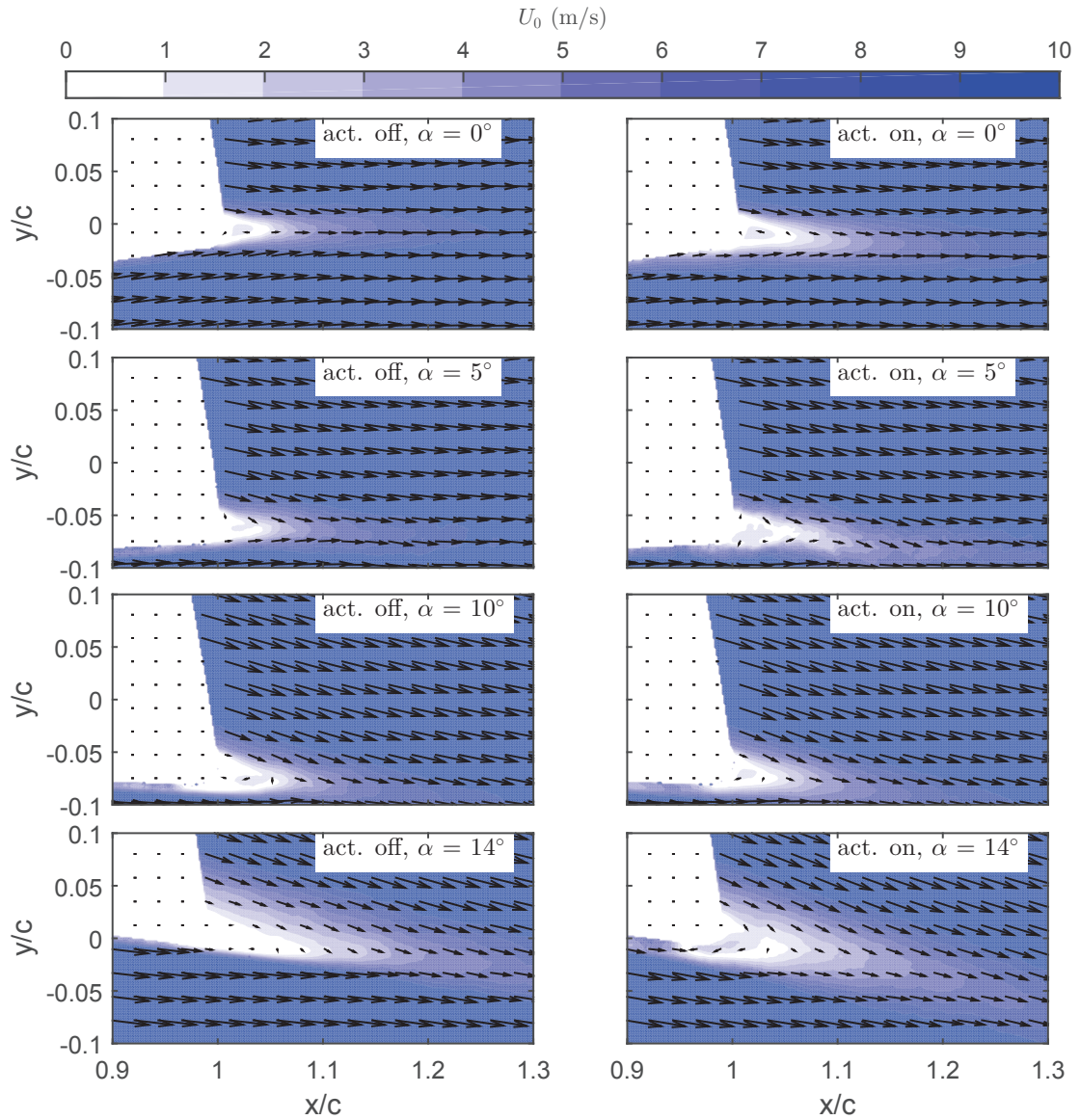


**Figure 5.13:** Time-averaged velocity vector field for the round trailing-edge. The actuator is positioned at centerline of the trailing-edge blowing towards pressure side (Kutta mode). ( $\alpha = 0^\circ$  &  $5^\circ$ ,  $c_\mu = 0.3\%$ ,  $U = 10\text{m/s}$ ,  $Re = 145,000$ )

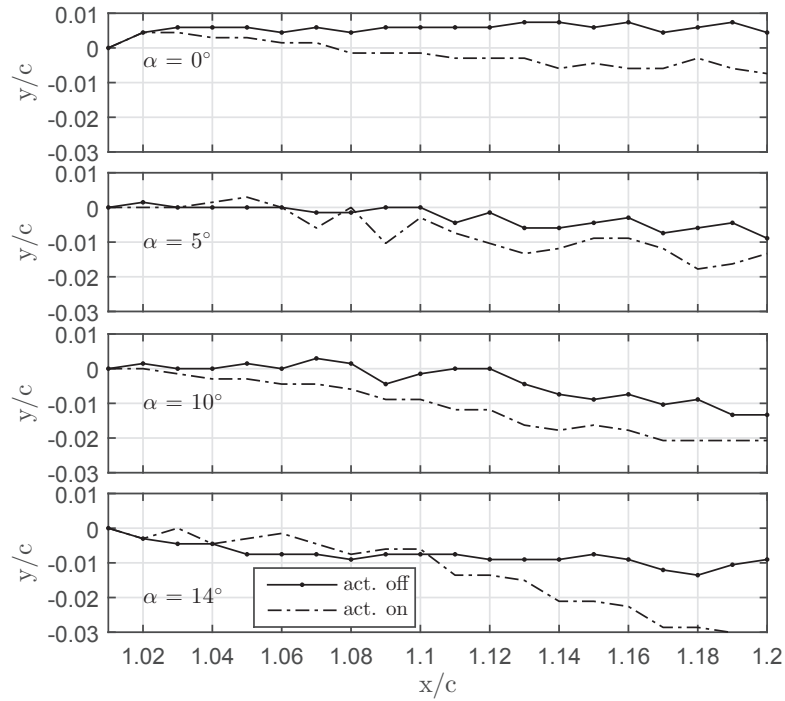


**Figure 5.14:** Location of the maximum streamwise velocity deficit in the wake for plasma 'off' and 'on' for the round trailing-edge. The actuator is positioned at centerline of the trailing-edge (Kutta mode). ( $c_\mu = 0.3\%$ ,  $U = 10\text{m/s}$ ,  $Re = 145,000$ )

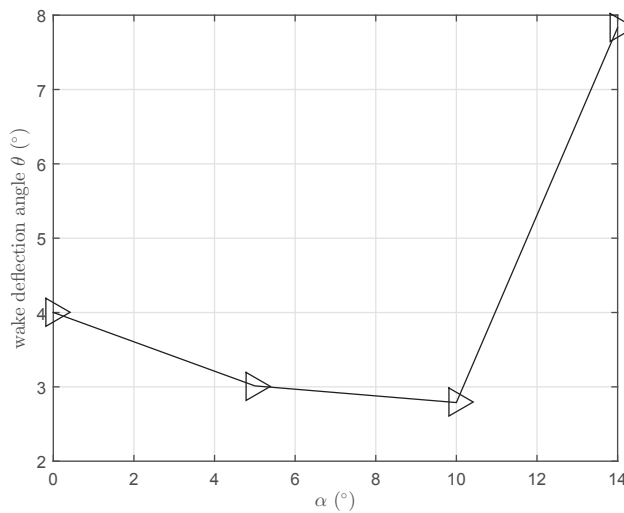


**Figure 5.15:** Wake deflection angle ( $\theta$ ) as a result of plasma actuation versus  $\alpha$  for the round trailing-edge. The actuator is positioned at centerline of the trailing-edge (Kutta mode). ( $c_\mu = 0.3\%$ ,  $U = 10\text{m/s}$ ,  $Re = 145,000$ )

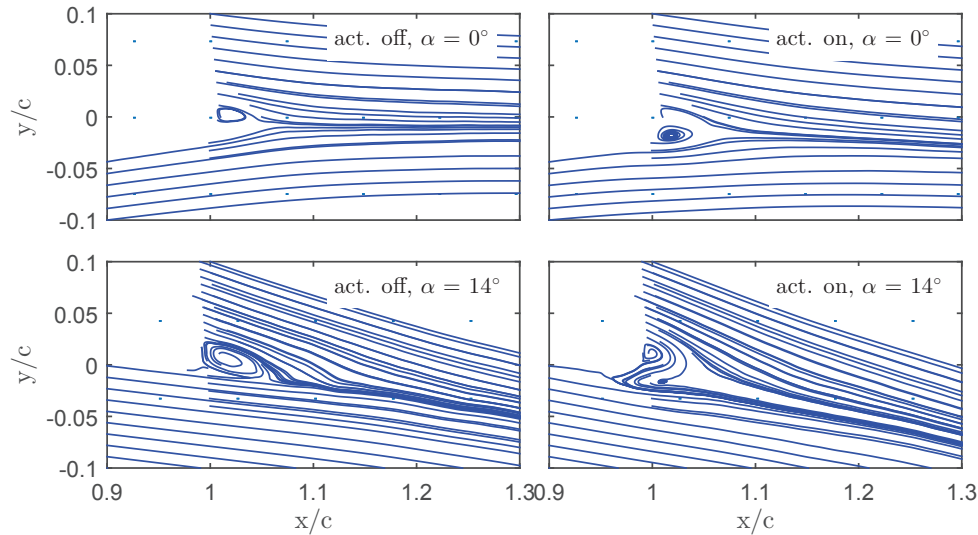


**Figure 5.16:** Flow streamlines for the round trailing-edge. The actuator is positioned at centerline of the trailing-edge blowing towards the pressure side (Kutta mode). ( $c_\mu = 0.3\%$ ,  $U = 10\text{m/s}$ ,  $Re = 145,000$ )

**POD of Vorticity field:** Additionally, POD (proper orthogonal decomposition) analysis is performed using the Sirovich method. A series of 300 image pairs of instantaneous velocity fields are used for the analysis.

The normalized non-dimensional vorticity fields of the first POD modes for the round trailing-edge are shown in Figure 5.21 and Figure 5.22. They correspond to the first vortex shedding mode.

Two effects of the actuation are visible in the POD modes of the vorticity field. The first effect is the increase in the length scale of the vortical structures of the wake. This is in good agreement with the understanding from TKE contours which showed an increase in the TKE as a result of the actuation. Basically higher energy vortices have a bigger length scale based on the turbulent energy spectrum. The second effect is the deflection of the wake as a result of the actuation which was also apparent in the mean velocity field and TKE plots. It is also observed that when the plasma is blowing to the suction side, at high angles of attack the actuator promotes the separation and disrupts the discrete vortex shedding pattern.

### 5.2.2.2 2push mode

**Aerodynamic loads and moments:** An investigation was done having one actuator working as Kutta mode at the centerline of the trailing-edge blowing towards the pressure side and one as a tab mode on the pressure side blowing upstream. The actuator setting for this test was  $30\text{ kV}_{pp}$  and  $1000\text{ Hz}$ . Due to arcing problems between the two actuators and their close distance, higher applied voltage could not be considered.

The results shown in (Figure 5.23 and Figure 5.24) imply a small increase in lift coefficient at lower angles of attack. Higher magnitude of increment is seen at higher angles of attack onwards to  $c_{l,max}$ .

Figure 5.23 and Figure 5.24 show the individual effect of actuator 1 (Kutta mode) and actuator 2 (tab mode) together with their mutual effect on the flow while both are on. From the total effect clearly a sum of both Kutta and tab modes is inferred.

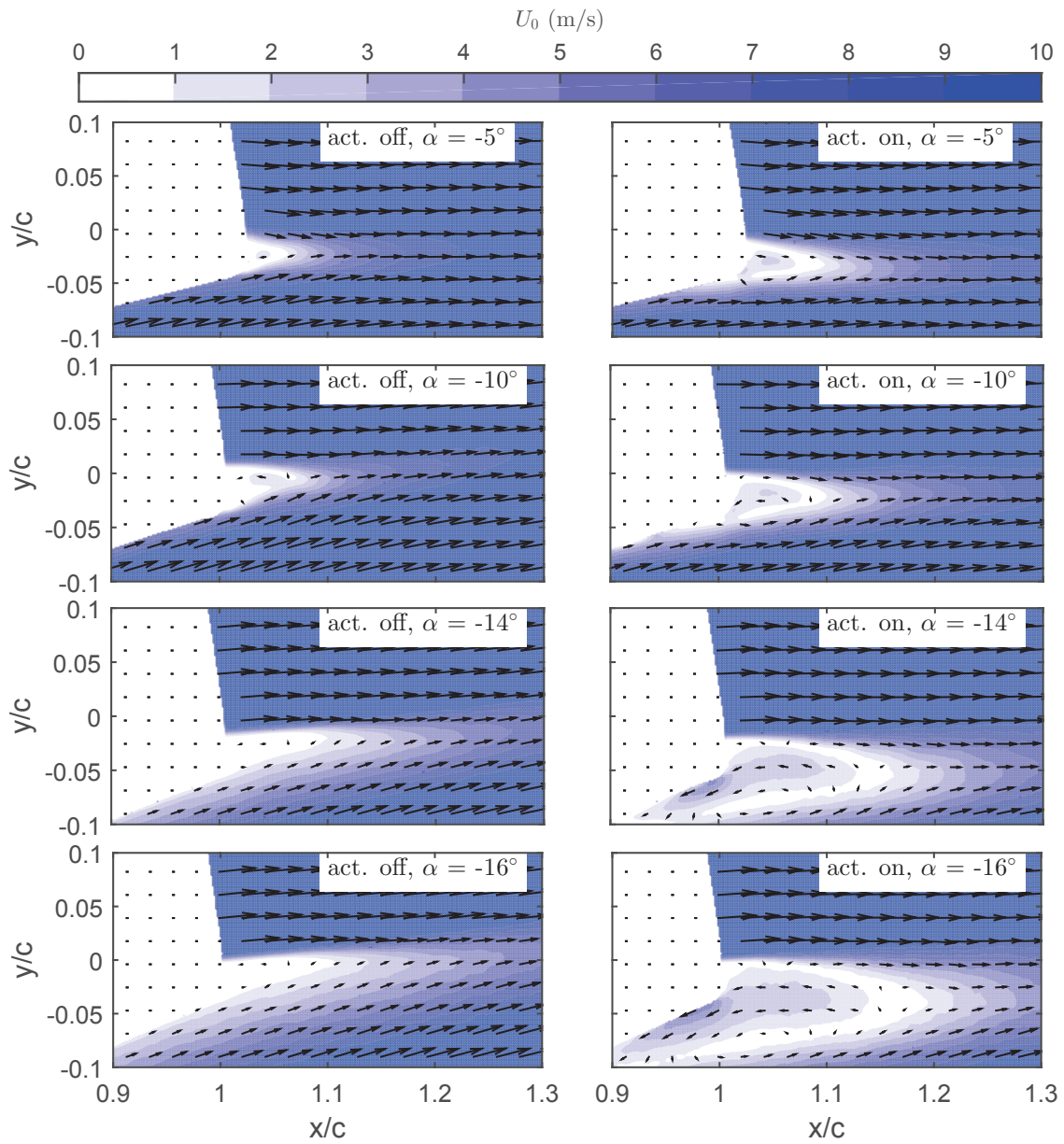


**Figure 5.17:** Time-averaged velocity vector field for the round trailing-edge. The actuator is positioned at centerline of the trailing-edge blowing towards suction side (Kutta mode). ( $\alpha = 10\&14^\circ$ ,  $c_\mu = 0.3\%$ ,  $U = 10\text{m/s}$ ,  $Re = 145,000$ )

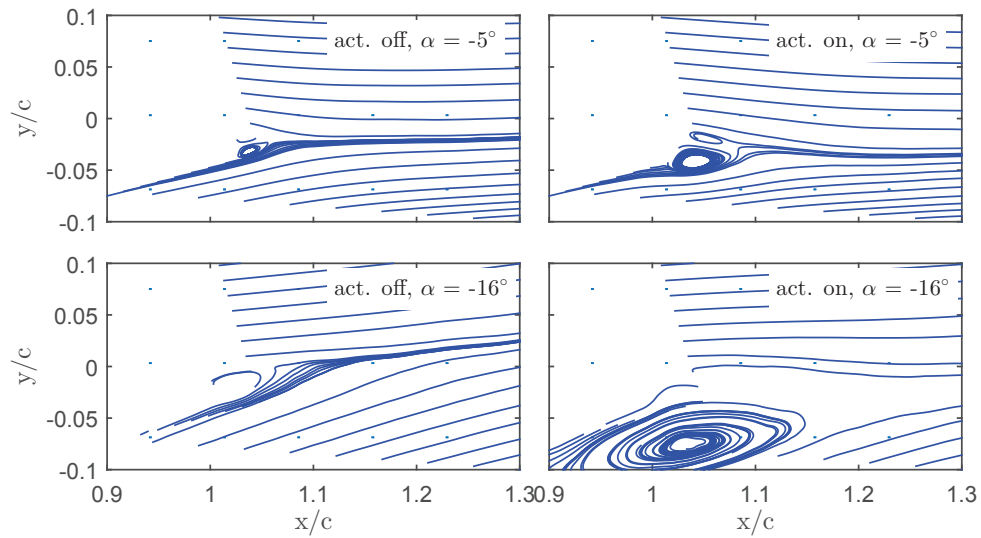


**Figure 5.18:** Flow streamlines for the round trailing-edge. The actuator is positioned at centerline of the trailing-edge blowing towards suction side (Kutta mode). ( $c_\mu = 0.3\%$ ,  $U = 10\text{m/s}$ ,  $Re = 145,000$ )

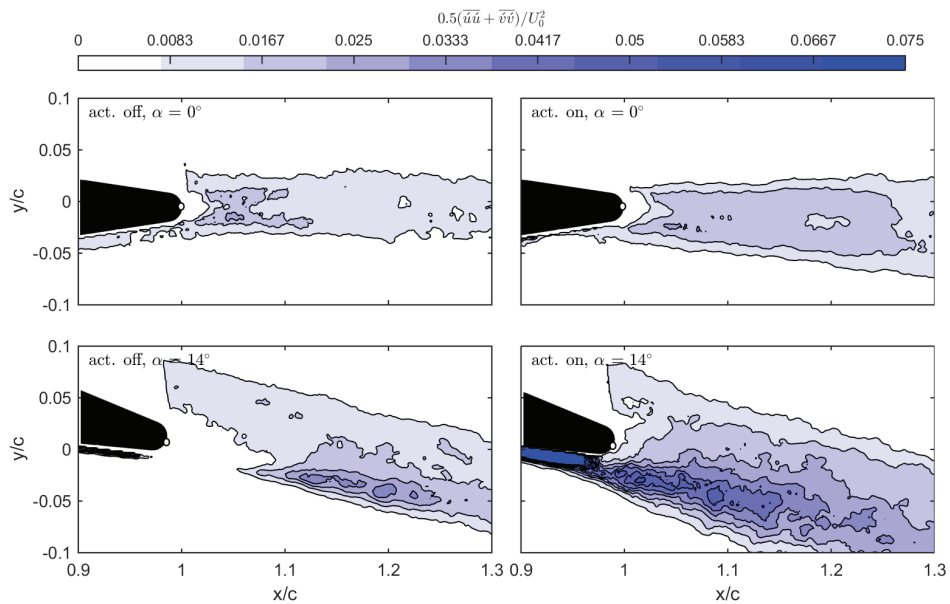


**Figure 5.19:** Turbulent kinetic energy for the round trailing-edge. The actuator is positioned at centerline of the trailing-edge (Kutta mode). ( $\alpha = 0\&5^\circ$ ,  $c_\mu = 0.3\%$ ,  $U = 10\text{m/s}$ ,  $Re = 145,000$ )

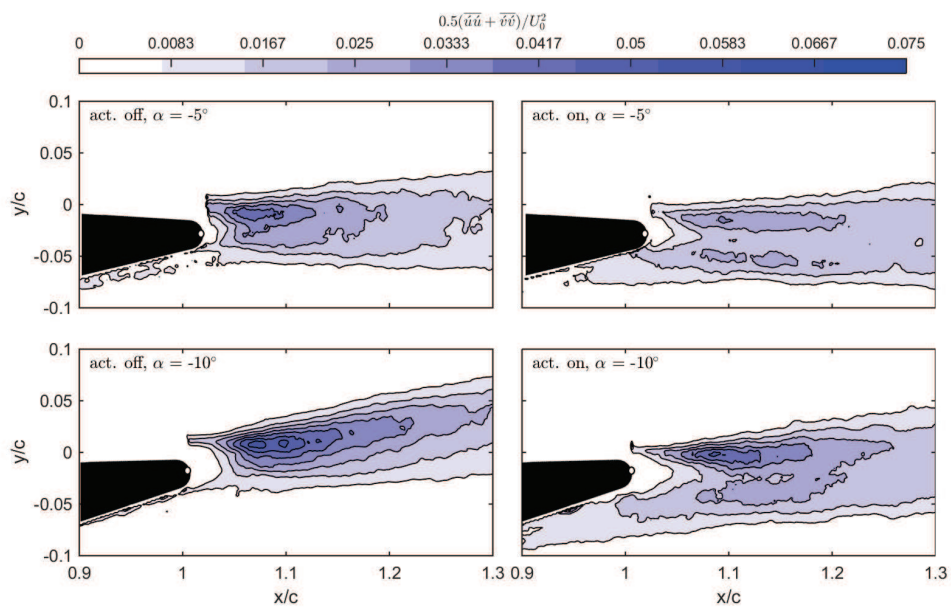


**Figure 5.20:** Turbulent kinetic energy for the round trailing-edge. The actuator is positioned at centerline of the trailing-edge (Kutta mode). ( $\alpha = 10\&14^\circ$ ,  $c_\mu = 0.3\%$ ,  $U = 10\text{m/s}$ ,  $Re = 145,000$ )

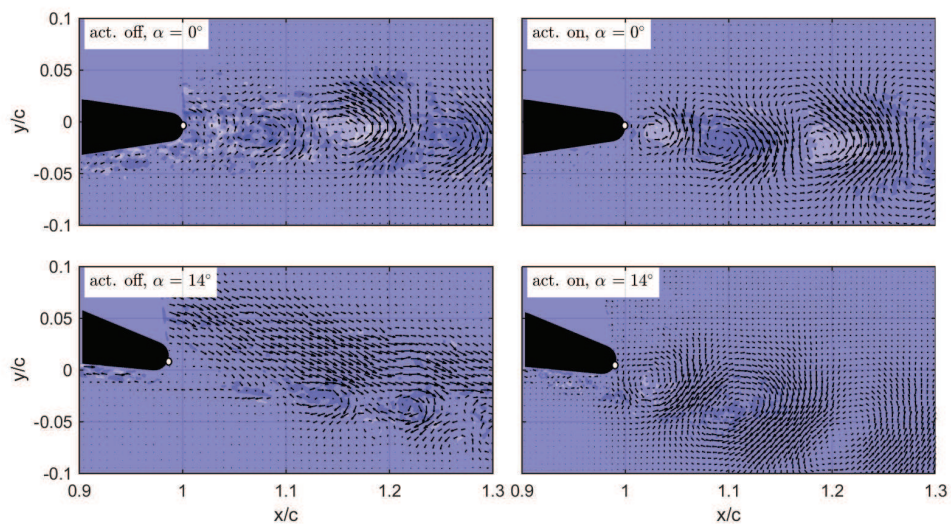


**Figure 5.21:** Normalized, non-dimensional vorticity fields of the first POD mode for the round trailing-edge. The actuator is positioned at centerline of the trailing-edge blowing to pressure side (Kutta mode). ( $\alpha = 0\&5^\circ$ ,  $c_\mu = 0.3\%$ ,  $U = 10\text{m/s}$ ,  $Re = 145,000$ )

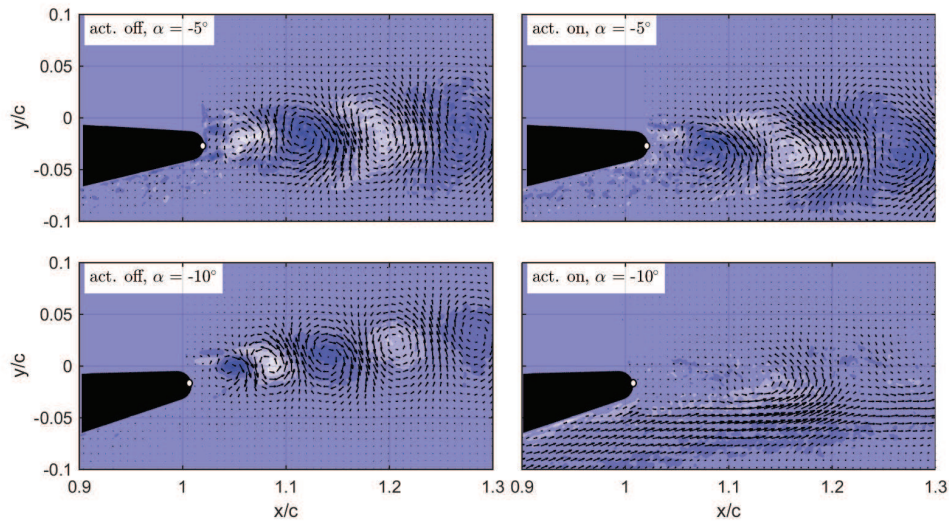


**Figure 5.22:** Normalized, non-dimensional vorticity fields of the first POD mode for the round trailing-edge. The actuator is positioned at centerline of the trailing-edge blowing to suction side (Kutta mode). ( $\alpha = 0\&5^\circ$ ,  $c_\mu = 0.3\%$ ,  $U = 10\text{m/s}$ ,  $Re = 145,000$ )

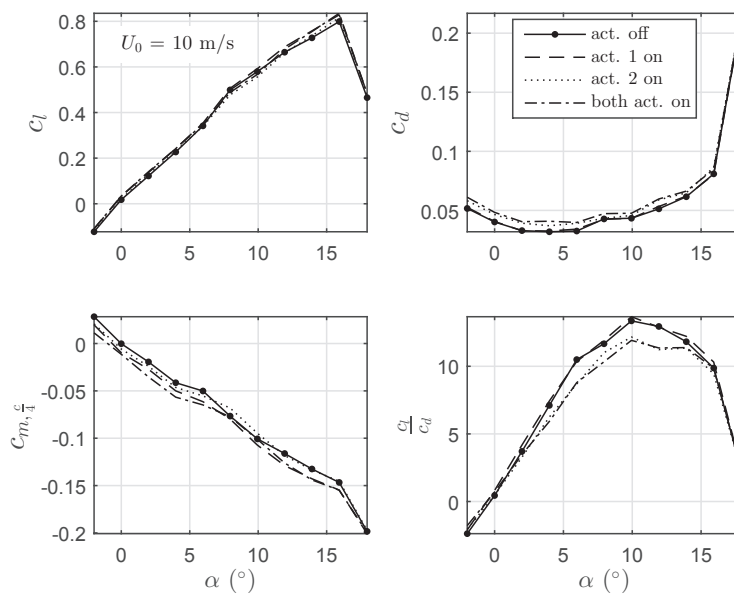


**Figure 5.23:** Lift, drag and moment coefficient as a function of angle of attack for the round trailing edge. One actuator is positioned at centerline of the trailing-edge (Kutta mode) and the second one on the pressure side blowing upstream (tab mode).

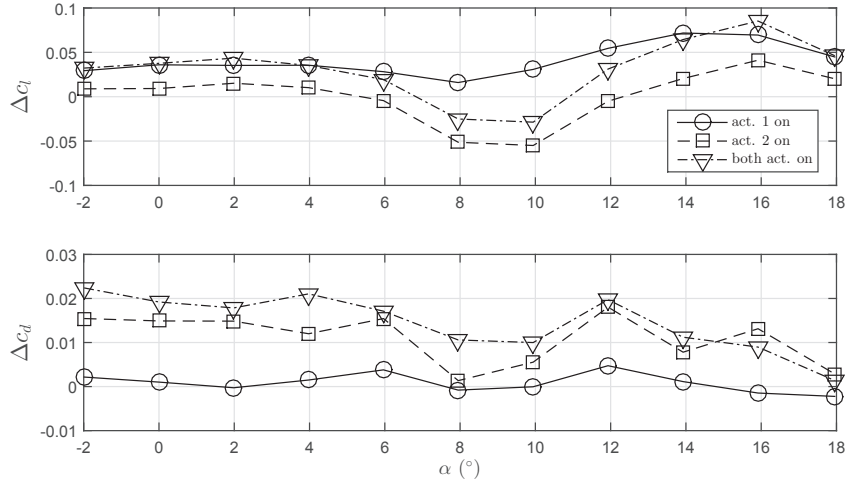


**Figure 5.24:** Variations of lift coefficient (per unit length of the actuator) relative to baseline as a function of freestream velocity and angle of attack for the round trailing-edge. One actuator is positioned at centerline of the trailing-edge (Kutta mode) and the second one on the pressure side blowing upstream (tab mode).

### 5.2.2.3 Npush mode

**Aerodynamic loads and moments:** This mode is designed to investigate the effect of plasma blowing interfering with the vortex shedding on aerodynamic loads of the airfoil. The actuators are installed to counteract the vortex shedding at the trailing-edge of the model. Each actuator is pulsating at half of the frequency of vortex shedding. The actuator setting for this test was  $30 kV_{pp}$  and  $1000Hz$ . Due to arcing problems between the two actuators and their close distance, higher applied voltage could not be considered.

The results shown in Figure 5.25 declares no significant effect of the actuator pulsation frequency on  $\Delta c_l$  at freestream velocities of  $10$  and  $20m/s$ . This study no correlation between the actuator pulsation frequency, vortex shedding frequency and  $\Delta c_l$ .

However, it is believed that the current arrangement of the electrodes is a 2D arrangement and consequently interferes the flow in a 2D manner. This is while the vortex shedding frequency is intrinsically a 3D pattern. Therefore, a 3D mechanism is required to be able to manipulate it.

A staggered arrangement of the electrodes can create a 3D manipulation of the vortex shedding structure and can be considered for future research on the topic.

The range of the actuator pulsation frequency was chosen around the vortex shedding frequency of the model. The vortex shedding frequency of the model which is shown with a vertical dashed green line on Figure 5.25 is measured using hot-wire anemometry installed at  $1.2\frac{x}{c}$  from leading edge.

**Vortex shedding frequency:** The vortex shedding frequency for the two trailing edge shapes (round and half-round) as a function of angle of attack and freestream velocity is shown in Figure 5.26.

### 5.2.3 Sharp trailing-edge

The effect of plasma actuation for load control is studied for the sharp trailing edge having the actuator positioned on the pressure side near the trailing-edge blowing upstream. This will principally work similar to a Gurney flap and a micro-tab while offering advantages of simplicity and high response-time over the two.

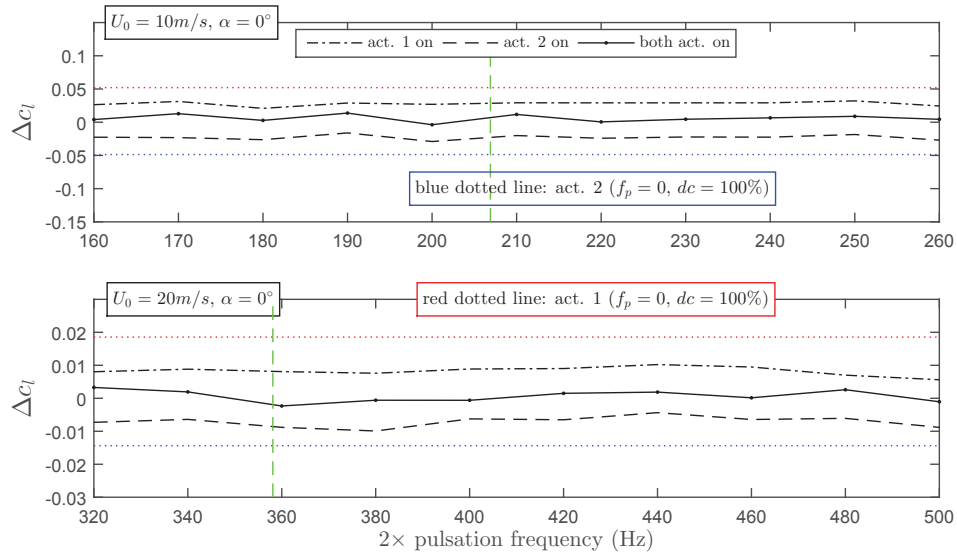


Figure 5.25: Variations of lift coefficient as a function of pulsation frequency for the round trailing-edge. The actuator is operating as Npush mode.

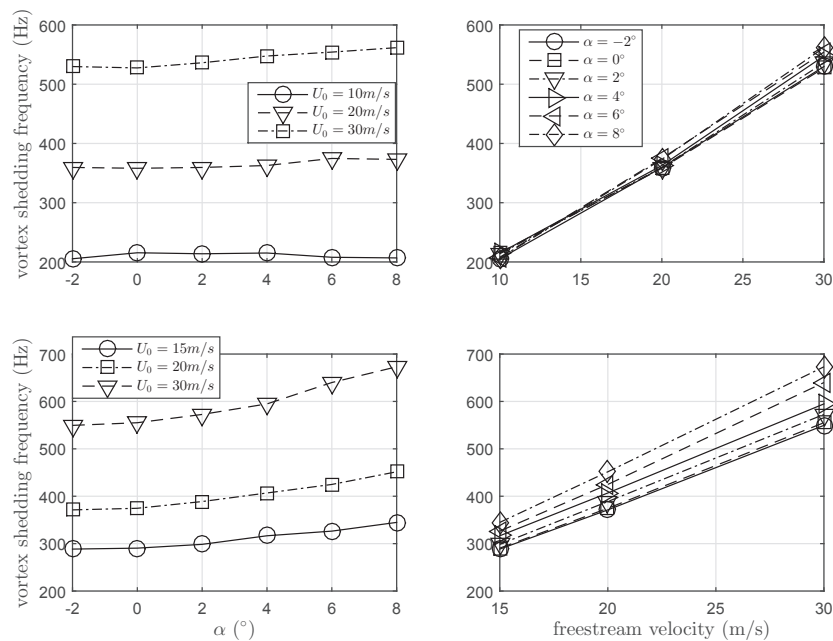


Figure 5.26: Variations of vortex shedding frequency as a function of freestream velocity and angle of attack for the round (top) and half-round (bottom) trailing-edges.

### 5.2.3.1 Tab mode

**Aerodynamic loads and moments:** The polar of aerodynamic force and moment coefficients for the plasma off and on cases are shown in Figure 5.27. It is seen that plasma blowing can increase the lift coefficient within  $-2..10^\circ$ .

This is believed to be a result of virtually increasing the camber of the airfoil by upstream plasma blowing and consequently inducing higher circulation around the airfoil. This is also confirmed by addition in drag coefficient due to introduction of a larger frontal area of the model to the flow.

From  $10^\circ$  onward to  $c_{l,max}$ , the actuator seems to decrease the lift coefficient. This is a result of the fact that the actuator promotes flow separation at higher angles of attack.

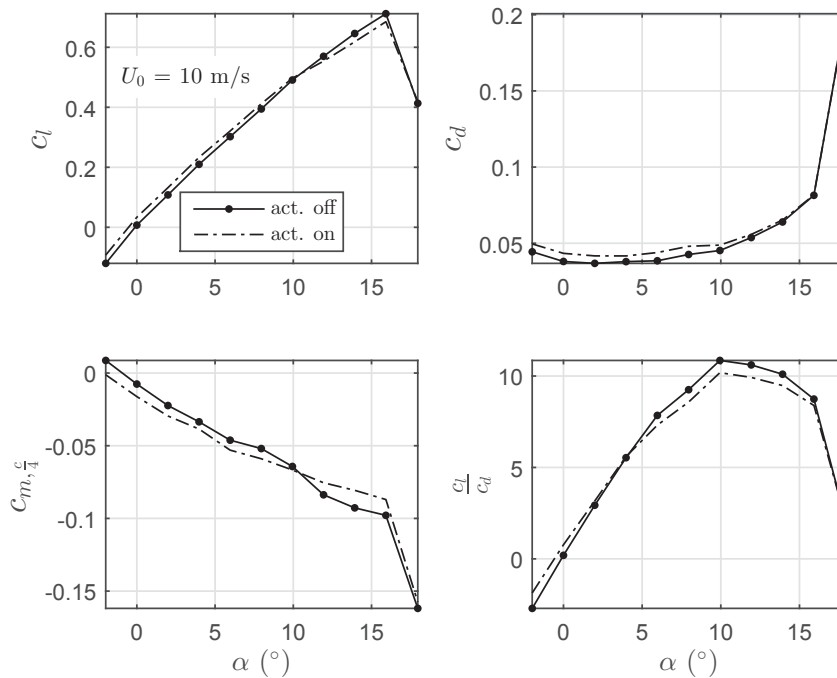


**Figure 5.27:** Lift, drag and moment coefficient as a function of angle of attack for the sharp trailing edge. The actuator is positioned on the pressure side blowing upstream (tab mode - pos A).

The highest increase in lift coefficient for the sharp trailing-edge (Figure 5.28 is slightly less than  $\Delta c_l = +0.1$  at  $0^\circ$  while the actuator decreases the lift to the same amount ( $\Delta c_l = -0.1$ ) at  $14 - 16$  degrees.

In another experiment the actuator is mounted on the suction side and the effect of upstream blowing on load control is studied and shown in Figure 5.29.

It is seen that this type of actuation results in a constant shift of  $\Delta c_l = -0.06$  for  $\alpha = 0..12^\circ$ . This has the same absolute magnitude as having the actuator on pressure side for the same range of angle of attack. The effect becomes stronger onwards to  $c_{l,max}$  where  $\Delta c_l = -0.24$  can be achieved. This is a significant reduction in loads near  $c_{l,max}$ . These values correspond to tests at  $10 \text{ m/s}$ . Such a great magnitude of load reduction can be very effective for load alleviation for wind turbines. The effect is weaker at  $20 \text{ m/s}$  as shown in Figure 5.29.

Furthermore, the effect of location of the plasma blowing on the pressure side is also studied with 3 different positions (Figure 5.30), A, B and C as described in the previous chapter. The result shows that although the effects are very close, however, the actuator blowing closest to the trailing-edge has the strongest effect.

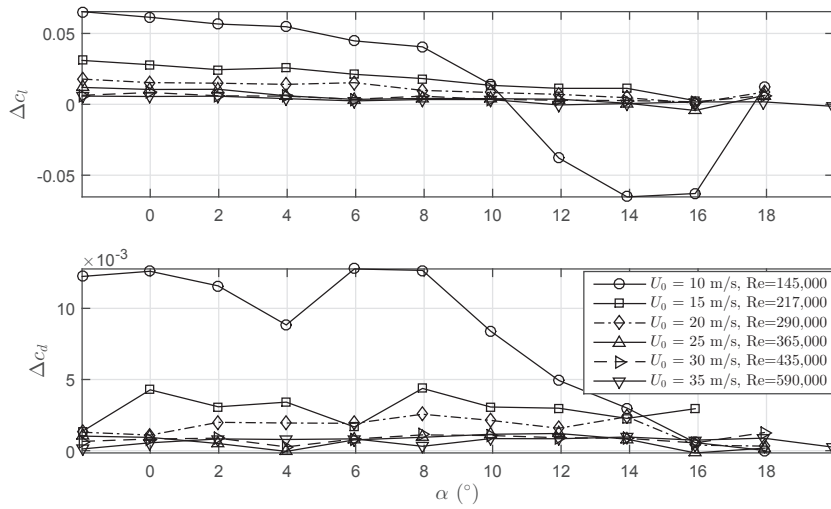


**Figure 5.28:** Variations of lift coefficient (per unit length of the actuator) relative to baseline as a function of freestream velocity and angle of attack for the sharp trailing-edge. The actuator is positioned on the pressure side blowing upstream (tab mode - pos A).

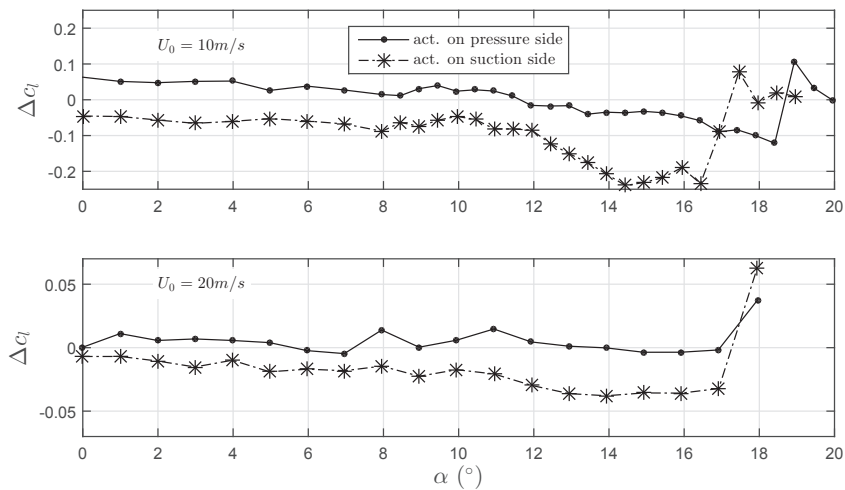


**Figure 5.29:** Variations of lift coefficient (per unit length of the actuator) relative to baseline as a function of freestream velocity and angle of attack for the sharp trailing-edge. The actuator is positioned either on the pressure or suction side blowing upstream at position A.

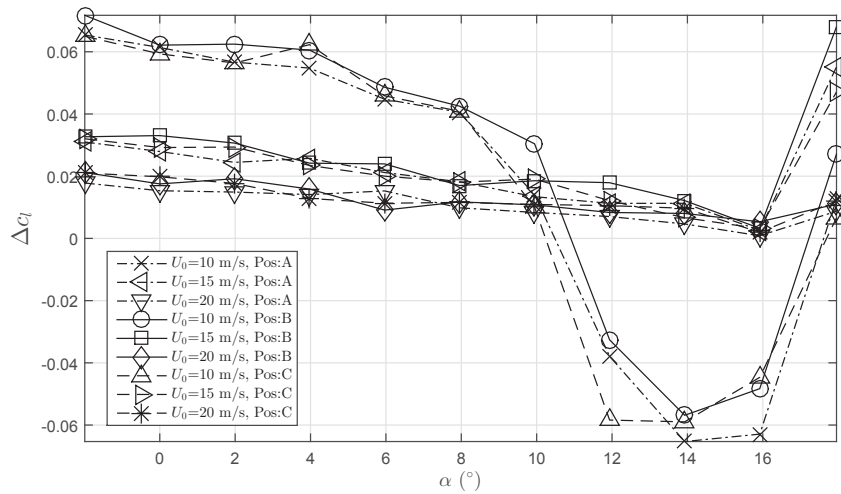


**Figure 5.30:** Variations of lift coefficient (per unit length of the actuator) relative to baseline as a function of freestream velocity and angle of attack for the sharp trailing-edge and different positioning of the virtual plasma tab. The actuator is positioned on the pressure side blowing upstream (tab mode - pos A, B and C).

**Time average velocity field and streamlines:** In order to investigate the change in flow pattern due to plasma blowing, time average velocity fields for the actuator on pressure side and suction side are shown in Figure 5.31 and Figure 5.33

The effect of plasma blowing on pressure side is creating a region with lower speed and resulting in a deficit in flow which virtually adds to the camber and induces higher circulation around the airfoil. This effect becomes weaker as the angle of attack increases until ends in flow separation and notable drop in lift.

In order to study the effect of the actuation in boundary layer scale, the time average velocity profile for the plasma off and on cases at  $\alpha = 14^\circ$  is shown in Figure 5.32. The position of the plasma onset is shown with a black circle.

A clear effect of the actuation seen by comparing the upper and lower images is a significant increment in boundary layer thickness just upstream the plasma onset. This explains the deficit in flow. As a result of the plasma blowing and the increment in boundary layer thickness upstream, a low pressure region is formed which results in deflection of particles with higher velocity from outside boundary layer into the boundary layer and creation of a region of higher velocity inside the boundary layer just downstream of the plasma blowing.

The thickness of the boundary layer decreases gradually downstream of the plasma onset, however, stays more than the case with no plasma actuation.

When the plasma blowing is on suction side, the local result in velocity reduction is much stronger and leads and decreases the circulation around the airfoil and reduces the drag.

**Mean turbulent kinetic energy:** In order to understand how the wake dynamics and turbulent kinetic energy of vortical structures are changed with plasma blowing, Figure 5.34 and Figure 5.35 are presented for the cases with plasma actuator on pressure and suction side correspondingly.

It is seen that in both cases, TKE which is a representation of turbulent mixing in the flow is increased as a result of plasma blowing. The effect is to a larger amount at higher angles of attack.

Additionally, when the actuator is blowing on pressure side the effect is seen as a small thicker layer of higher TKE near the model walls, i.e. increment in thickness of boundary layer. However, when the actuator is blowing on the suction side the effect is mostly seen as a large area of separated flow over the suction side

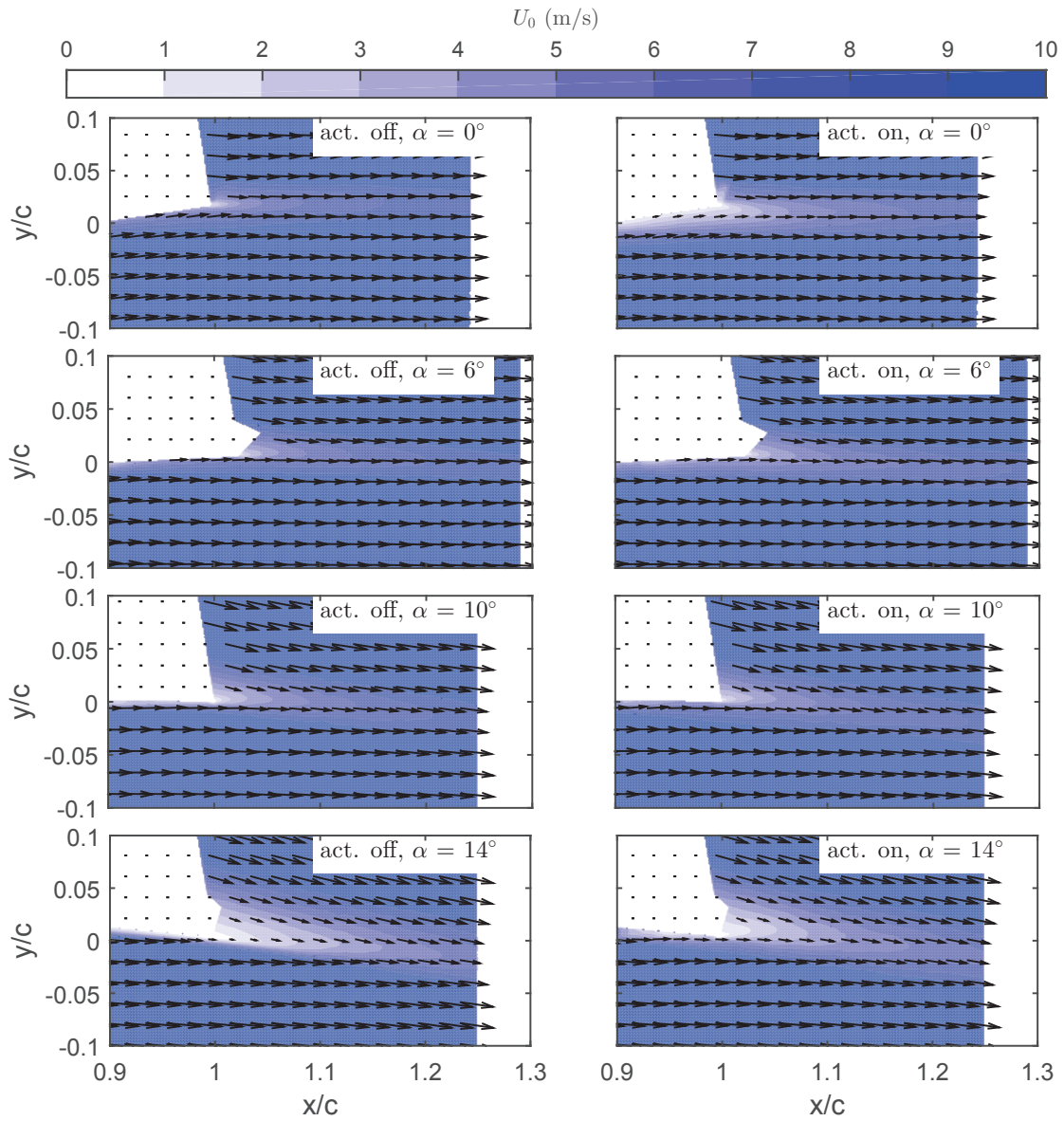


**Figure 5.31:** Time-averaged velocity vector field for the sharp trailing-edge. The actuator is positioned on the pressure side blowing upstream (tab mode - pos A). ( $\alpha = 0\&5^\circ$ ,  $c_\mu = 0.3\%$ ,  $U = 10\text{m/s}$ ,  $Re = 145,000$ )

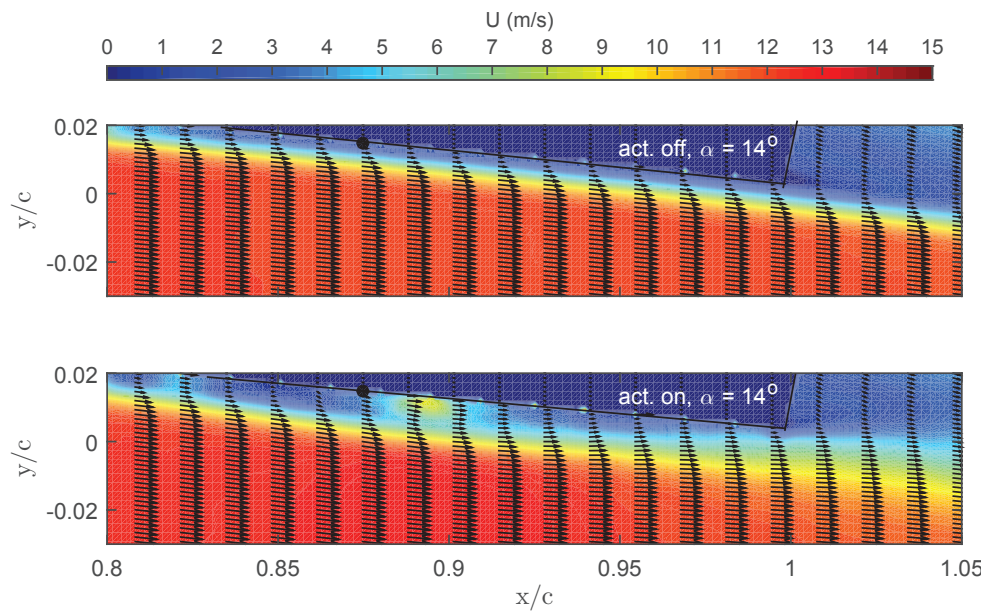


**Figure 5.32:** Time-averaged velocity vector field of the boundary layer for the sharp trailing-edge. The actuator is positioned on the pressure side blowing upstream (tab mode - pos A). The position of the plasma onset is shown with a black circle. ( $\alpha = 0\&5^\circ$ ,  $c_\mu = 0.3\%$ ,  $U = 10\text{m/s}$ ,  $Re = 145,000$ )

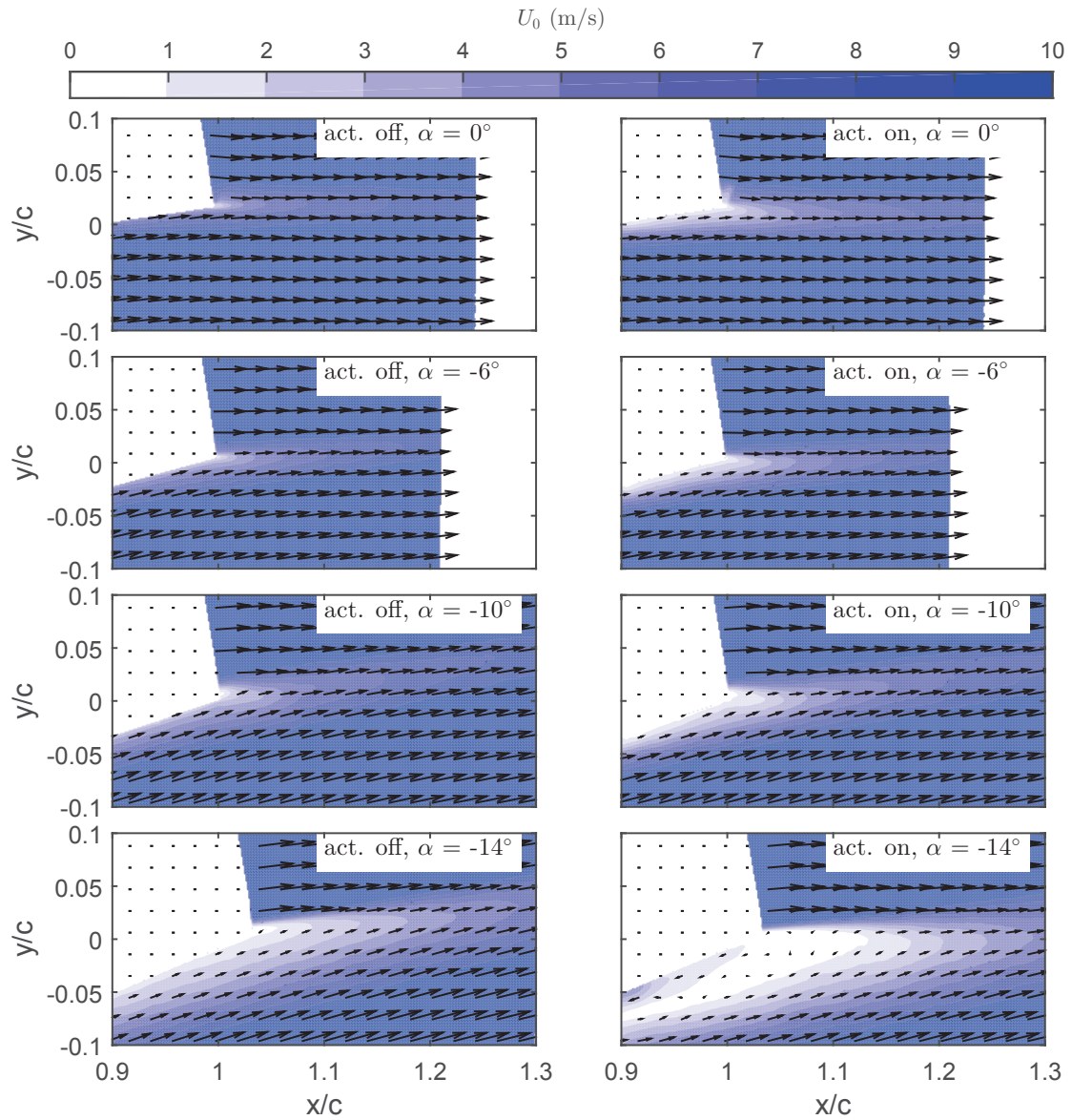


**Figure 5.33:** Time-averaged velocity vector field for the sharp trailing-edge. The actuator is positioned on the pressure side blowing upstream (tab mode - pos A). ( $\alpha = 0^\circ, 5^\circ, c_\mu = 0.3\%, U = 10\text{m/s}, Re = 145,000$ )

with higher TKE. The comparison shows that at the same angle of attack, the increase in TKE affects a larger region when the blowing occurs on the suction side.

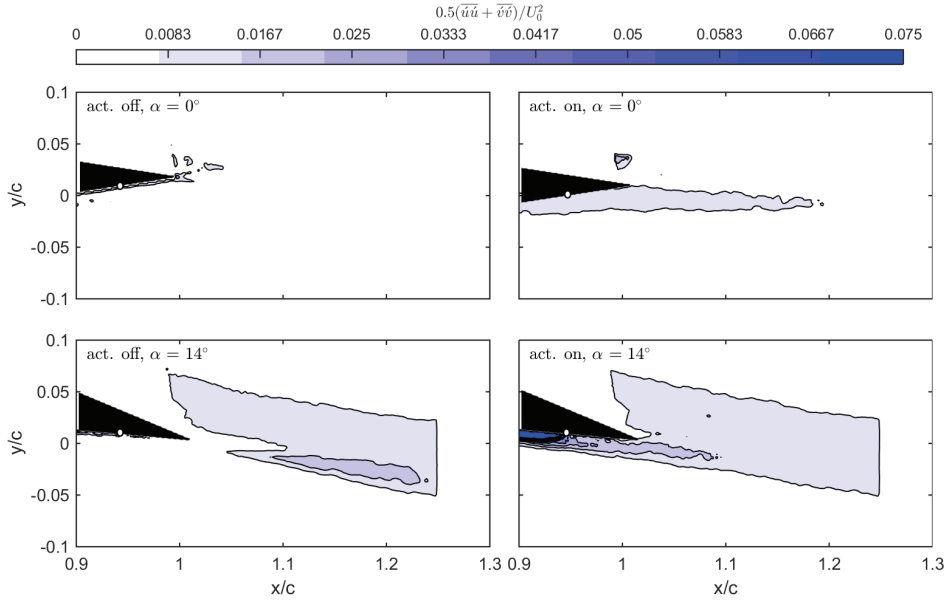


**Figure 5.34:** Turbulent kinetic energy for the sharp trailing-edge. The actuator is positioned on the pressure side blowing upstream (tab mode - pos A). ( $\alpha = 0$  &  $5^\circ$ ,  $c_\mu = 0.3\%$ ,  $U = 10\text{m/s}$ ,  $Re = 145,000$ )

**POD of Vorticity field:** The normalized non-dimensional vorticity fields of the first POD mode corresponding to the first vortex shedding mode for the sharp trailing-edge with the actuator positioned on the suction side is shown in Figure 5.36.

It is seen that at low angles of attack, there is no visible vortex shedding when the actuator is off. However, the plasma actuation results in a weak vortex shedding. This is visible both from the POD (Figure 5.36) and the energy of the fluctuations shown in (Figure 5.37).

As angles of attack increases this effect strengthens until stall happens. At higher angles of attack before stall when there is a limited separation at trailing-edge, vortex shedding is observed for the plasma off. The actuation of plasma blowing results in extension of the separation and there is a significant increase in the length scale of the vortical structures. This is also observed from the increase in the energy of the fluctuating energy budget of the first mode.

When stall happens, the flow is fully separated and as the energy budget shows, the actuation loses its effectiveness.

## 5.2.4 Half-round trailing-edge

### 5.2.4.1 Kutta mode

**Aerodynamic loads and moments:** The polars and the  $\Delta c_l - \alpha$  plot for the half-round trailing-edge are shown in Figure 5.38 and Figure 5.39. A similar behavior with the round trailing-edge with an almost

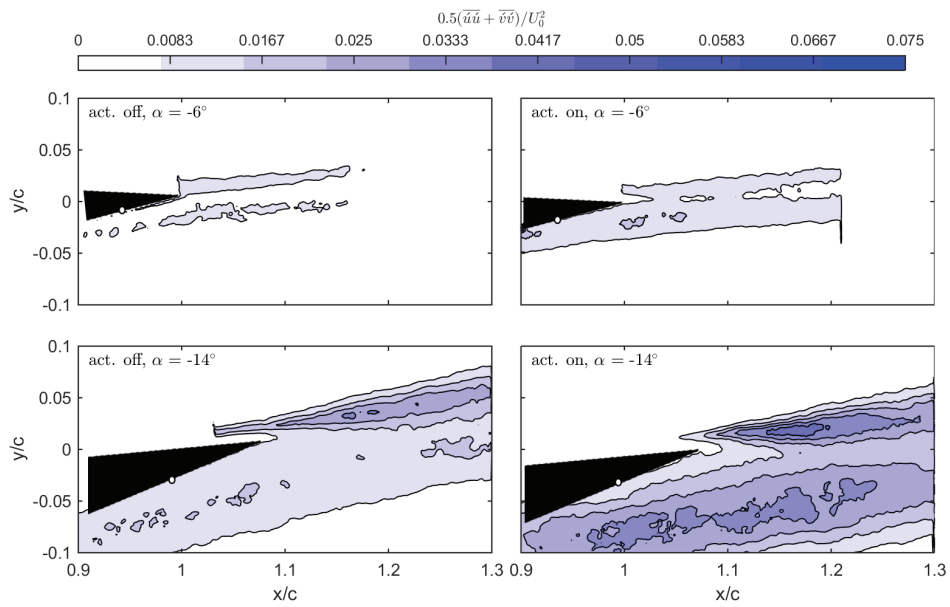


**Figure 5.35:** Turbulent kinetic energy for the sharp trailing-edge. The actuator is positioned on the pressure side blowing upstream (tab mode - pos A). ( $\alpha = 0\&5^\circ$ ,  $c_\mu = 0.3\%$ ,  $U = 10\text{m/s}$ ,  $Re = 145,000$ )

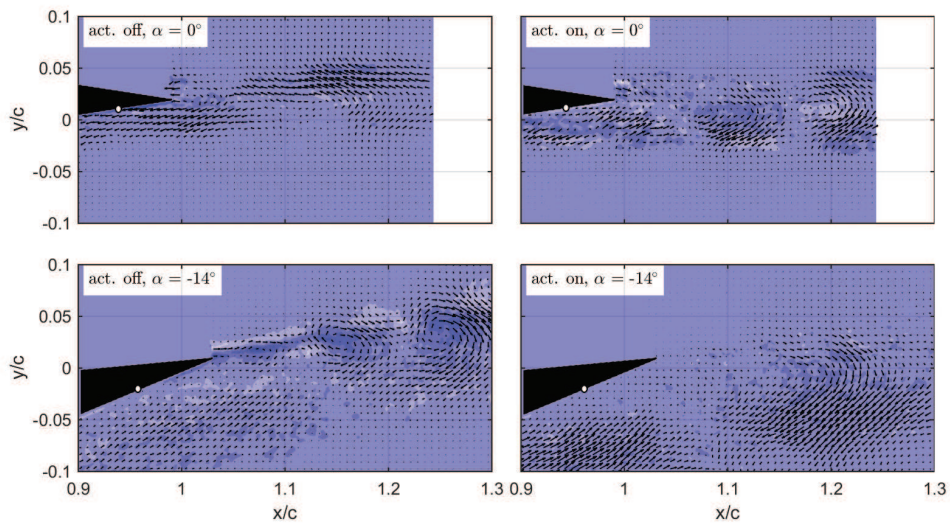


**Figure 5.36:** Normalized, non-dimensional vorticity fields of the first POD mode for the sharp trailing-edge. The actuator is positioned on the suction side blowing upstream (tab mode - pos A). ( $\alpha = 0\&5^\circ$ ,  $c_\mu = 0.3\%$ ,  $U = 10\text{m/s}$ ,  $Re = 145,000$ )

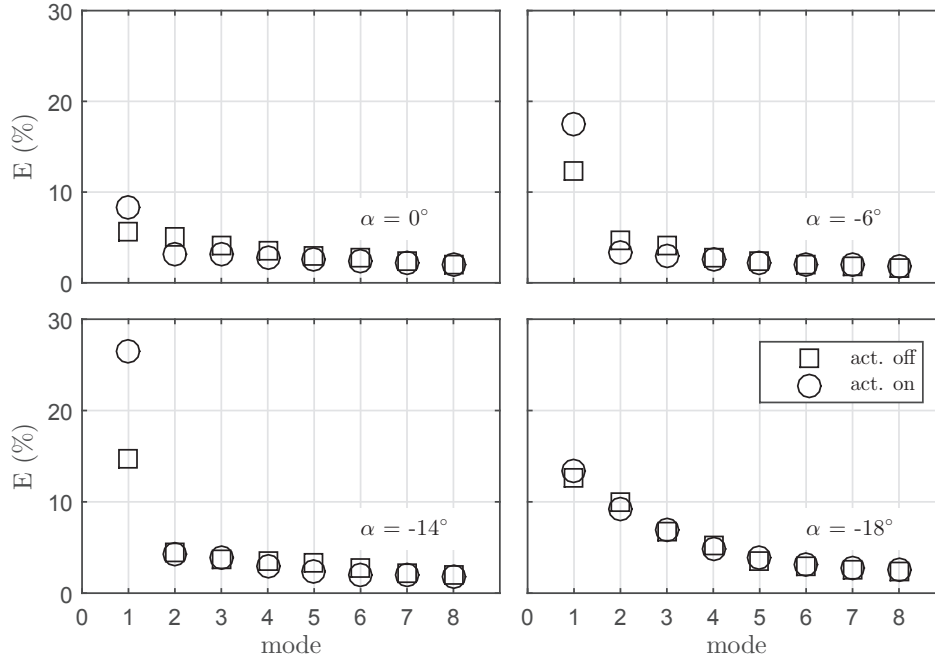


**Figure 5.37:** Fluctuating energy budget of first 8 POD modes for the sharp trailing-edge. The actuator is positioned on the pressure side blowing upstream (tab mode - pos A). ( $\alpha = 0$  &  $5^\circ$ ,  $c_\mu = 0.3\%$ ,  $U = 10\text{m/s}$ ,  $Re = 145,000$ )

50% lower magnitude was observed for the half-round trailing-edge. The lower magnitude is believed to be a result of the fact that this trailing-edge is half-sharp and half-round and therefore the stagnation point at the trailing-edge is tend to become fixed by the sharp half on one side. Thus the Kutta condition is less controllable compared to the round trailing-edge.

This is also confirmed when less wake deflection is seen with the actuator 'on' test for the half-round compared to round trailing-edge.

**Time average velocity field and streamlines:** In order to understand how the actuator is changing the aerodynamic loads, the time-averaged velocity field is investigated for cases without and with plasma actuation.

Figure 5.40 shows the time average velocity field for the half-round trailing-edge. It is seen that this trailing-edge has a thinner wake compared to the round one. This is due to the fact that the half-round has a sharp side where the flow leaves the trailing-edge attached up to higher angle of attack. Therefore, the wake is a result of only the round side.

Similar effect of the plasma actuation is also observed for the half-round trailing-edge as shown in Figure 5.40. However, the effect is to a smaller magnitude. This is in good agreement with the force measurements where the change in lift coefficient was almost half of the round trailing-edge.

The effect of the plasma actuation in downward-deflection of the wake for different angles of attack as shown in Figure 5.41. The angle of the downward-deflection (shown in Figure 5.42) caused by the actuator corresponds well with the magnitude of  $\Delta c_l$  for the angles of attack  $0^\circ$ ,  $5^\circ$  and  $14^\circ$  but it does not correlate for  $10^\circ$  where a reduction in the force but increase in the angle of deflection is observed. This is believed to be an outlier resulted from the method used for finding the angle of deflection. Apart from that, the correlation between the angle of deflection and the magnitude of  $\Delta c_l$  is confirmed from the results of round and half-round trailing-edge tests.

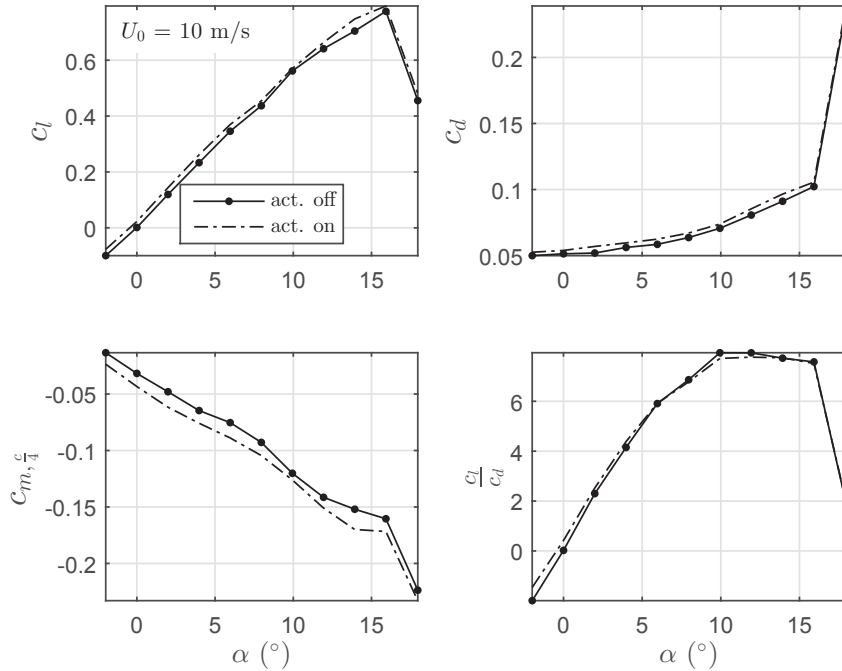


Figure 5.38: Lift, drag and moment coefficient as a function of angle of attack for the half-round trailing edge. The actuator is positioned at centerline of the trailing-edge (Kutta mode).

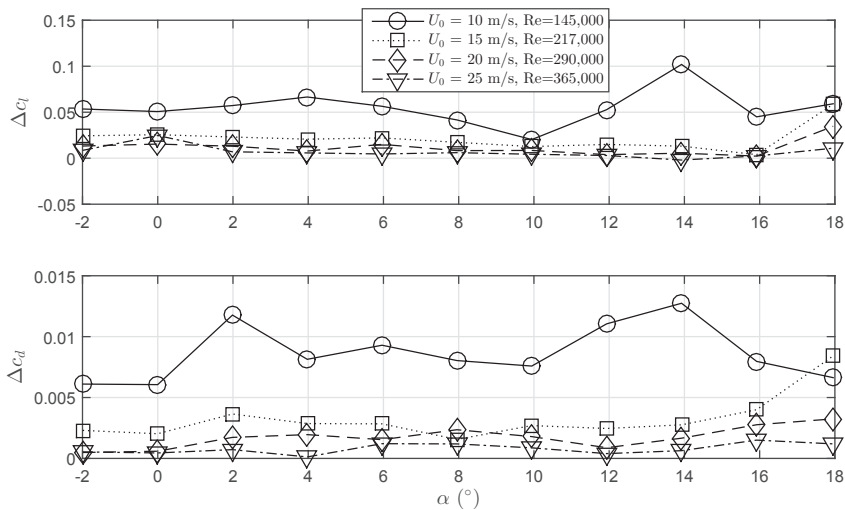
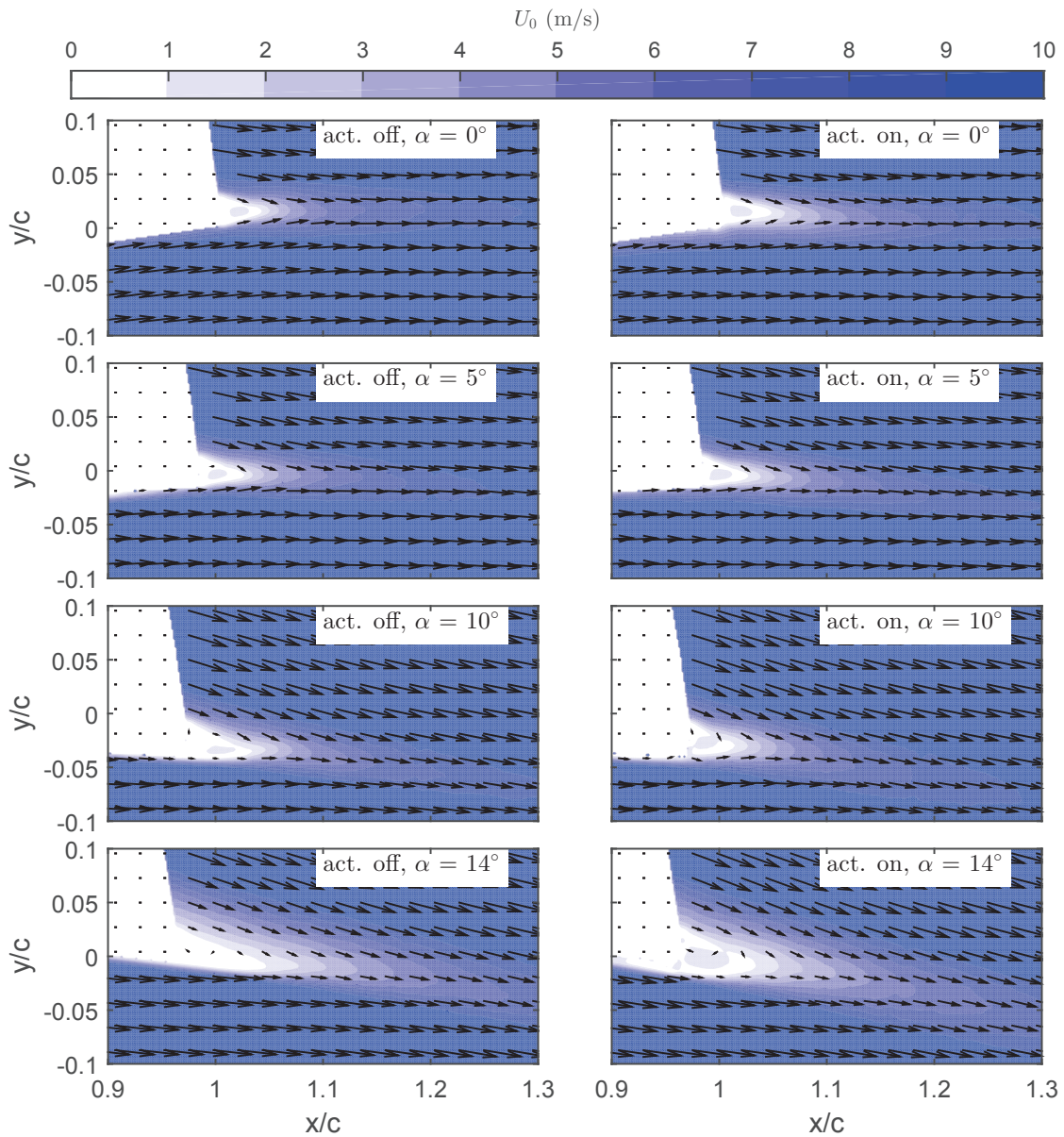
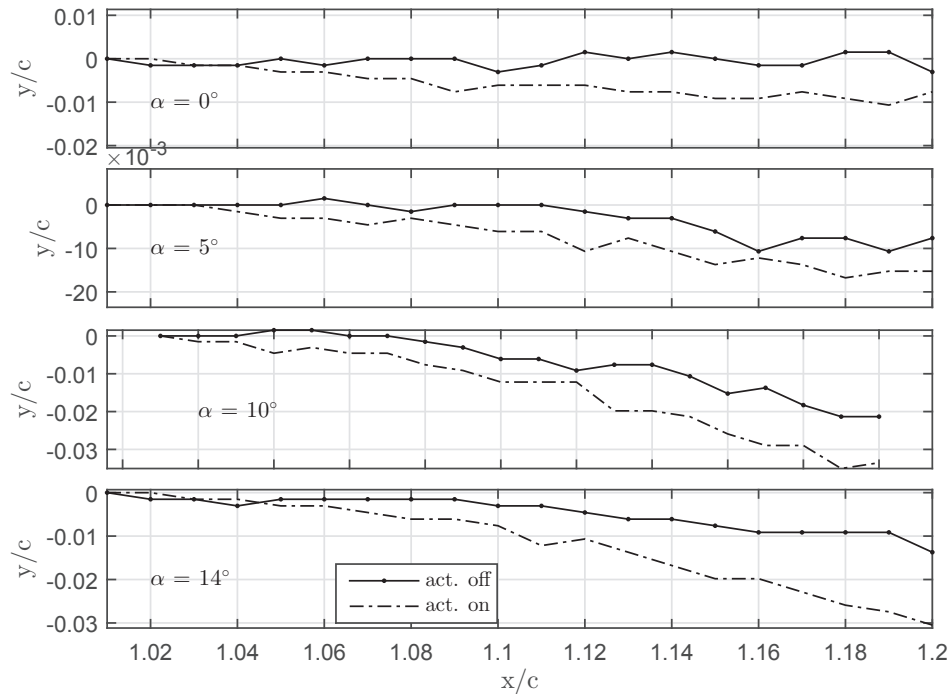


Figure 5.39: Variations of lift coefficient (per unit length of the actuator) relative to baseline as a function of freestream velocity and angle of attack for the half-round trailing-edge. The actuator is positioned at centerline of the trailing-edge (Kutta mode).



**Figure 5.40:** Time-averaged velocity vector field for the half-round trailing-edge. The actuator is positioned at centerline of the trailing-edge (Kutta mode). ( $\alpha = 0^\circ$  &  $5^\circ$ ,  $c_\mu = 0.3\%$ ,  $U = 10\text{m/s}$ ,  $Re = 145,000$ )



**Figure 5.41:** Location of the maximum streamwise velocity deficit in the wake for plasma 'off' and 'on' for the round trailing-edge. The actuator is positioned at centerline of the trailing-edge (Kutta mode). ( $c_\mu = 0.3\%$ ,  $U = 10\text{m/s}$ ,  $Re = 145,000$ )

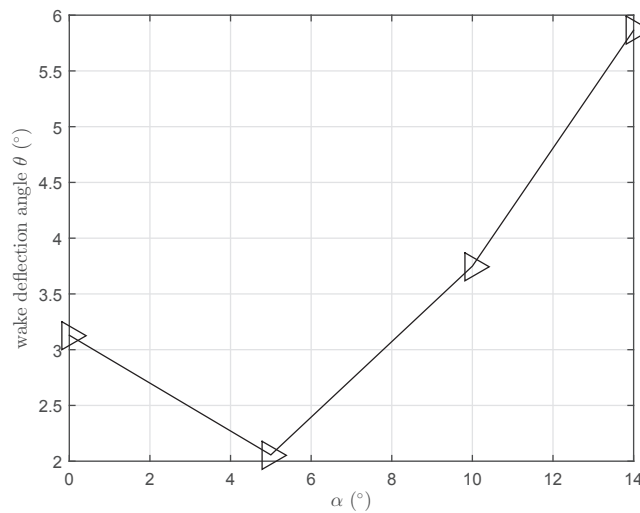


**Figure 5.42:** Wake deflection angle ( $\theta$ ) as a result of plasma actuation versus  $\alpha$  for the round trailing-edge. The actuator is positioned at centerline of the trailing-edge (Kutta mode). ( $c_\mu = 0.3\%$ ,  $U = 10\text{m/s}$ ,  $Re = 145,000$ )

**Mean turbulent kinetic energy:** Similarly to the round trailing-edge, the TKE in the wake behind is studied for the half-round model and it is seen that the actuator enhances the energy of the vortical structures near the trailing-edge and increases the turbulent mixing. However, the increment is smaller compared to the round trailing-edge.

This well correlates with the amount of change in lift coefficient and deflection in the mean speed where higher values were experienced for the round model.

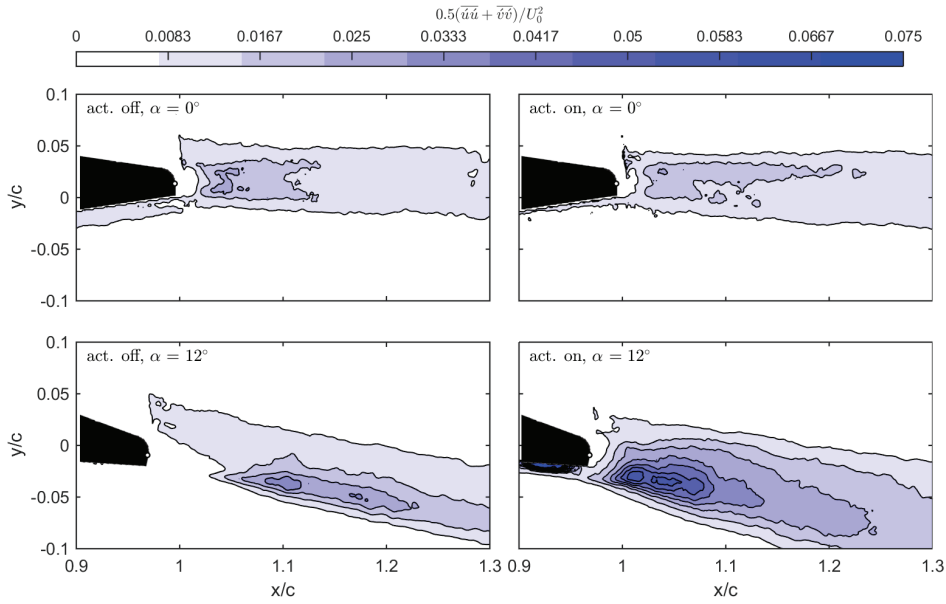


**Figure 5.43:** Turbulent kinetic energy for the half-round trailing-edge. The actuator is positioned at centerline of the trailing-edge (Kutta mode). ( $\alpha = 0$  &  $5^\circ$ ,  $c_\mu = 0.3\%$ ,  $U = 10\text{m/s}$ ,  $Re = 145,000$ )

**POD of Vorticity field:** Similar effect to the round trailing-edge, it is also observed for the half-round trailing-edge (Figure 5.44) that the length scale of the vortical structures are increased and the wake is deflected downwards as a result of plasma actuation.

The increment in length scale of the vortical structures is found to be smaller for lower angles of attack and larger for higher angles of attack.

This is the most important effect of the plasma actuation in Kutta mode on the wake dynamics. This is confirmed when observing the fluctuating energy budget of the first 8 POD modes for the model.

The energy budget implies that plasma actuation increases the energy of the first 2 modes which correspond to the vortex shedding modes. This is in good agreement with the increment in the size of the vortical structures as bigger vortices contain higher energy based on the turbulence energy spectrum.

The level of energy increment is seen to be low for  $5^\circ$  and  $10^\circ$  and higher for  $0^\circ$  and  $12^\circ$ . Higher increment for higher angles of attack is in agreement with higher increase in length scale of vortical structures and higher wake deflection angle observed for higher angles of attack.

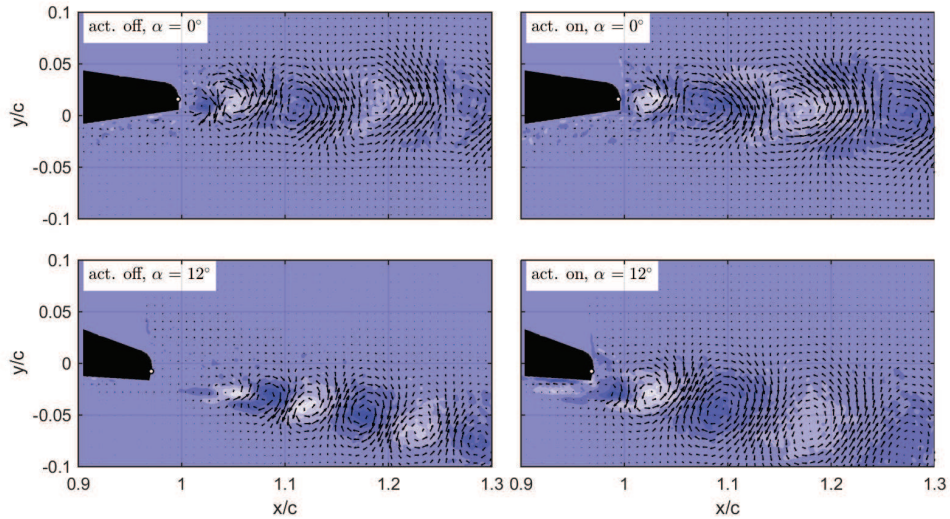


**Figure 5.44:** Normalized, non-dimensional vorticity fields of the first POD mode for the half-round trailing-edge. The actuator is positioned at centerline of the trailing-edge (Kutta mode). ( $\alpha = 0\&5^\circ$ ,  $c_\mu = 0.3\%$ ,  $U = 10\text{m/s}$ ,  $Re = 145,000$ )

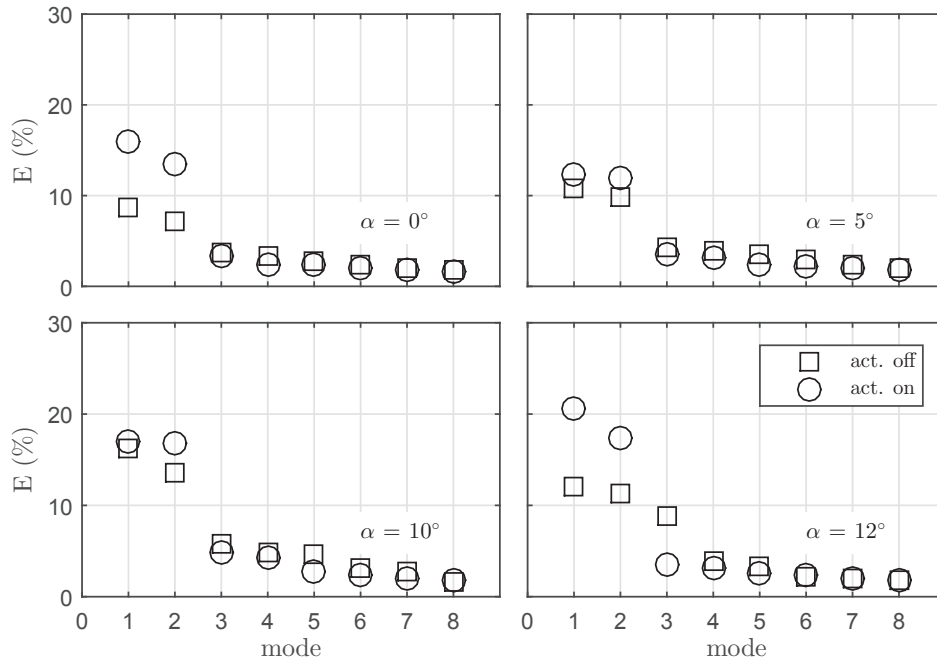


**Figure 5.45:** Fluctuating energy budget of first 8 POD modes for the half-round trailing-edge. The actuator is positioned on the centerline of the trailing-edge (Kutta mode). ( $c_\mu = 0.3\%$ ,  $U = 10\text{m/s}$ ,  $Re = 145,000$ )

### 5.2.4.2 Tab mode

**Aerodynamic loads and moments:** A similar effect to the sharp trailing-edge model is observed for the half-round trailing-edge (Figure 5.46) when the actuator is positioned on the pressure side and blowing upstream. Except that even at higher angle of attack, an increment in lift is observed. The lift coefficient is increased up to about  $10^\circ$  while it reduces later on to  $c_{l,max}$ .

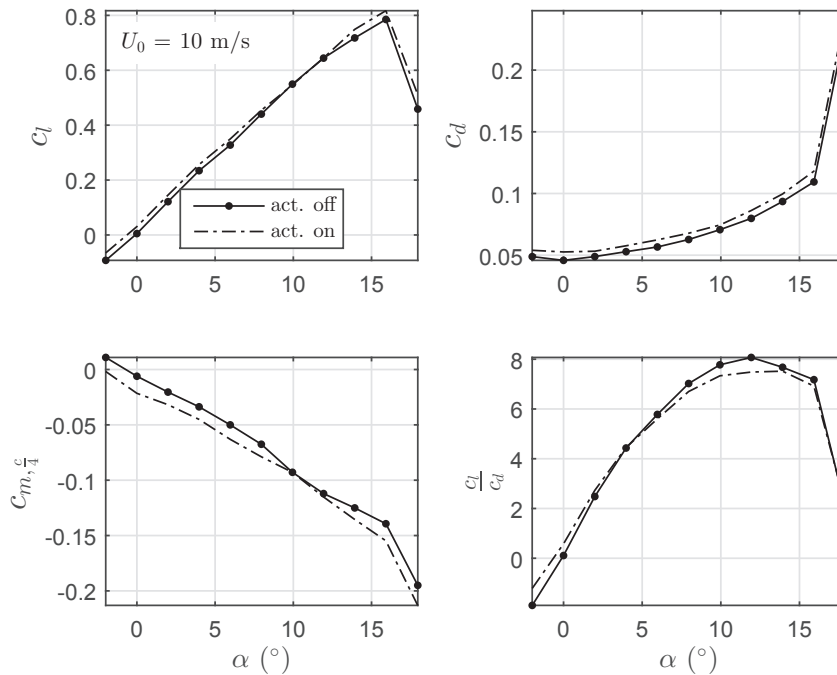


**Figure 5.46:** Lift, drag and moment coefficient as a function of angle of attack for the half-round trailing edge. The actuator is positioned on the pressure side blowing upstream (tab mode).

The amount of change in lift coefficient, however, is smaller compared to the sharp trailing-edge (Figure 5.47).

**Time average velocity field:** The effect of plasma blowing as a tab for the half-round trailing-edge is found to be similar to the sharp trailing-edge. The effect as seen in Figure 5.48 is increasing the boundary layer thickness just upstream the plasma onset and an increase in the velocity of boundary layer just downstream the plasma onset. Moreover, the boundary layer thickness gradually decreases downstream of the plasma blowing.

**TKE and POD of vorticity field:** The studies for the wake dynamics found similar results to the previous models described. Therefore, for brevity the plots are not presented here.

### 5.2.4.3 2push mode

**Aerodynamic loads and moments:** An investigation was done having one actuator working as Kutta mode and one as a tab mode. The result shows that (Figure 5.23 and Figure 5.24) a small increase in lift coefficient is observed at lower angles of attack while more increase is seen at higher angles of attack to stall. The effect seems like an approximate sum effect of both Kutta and tab modes.

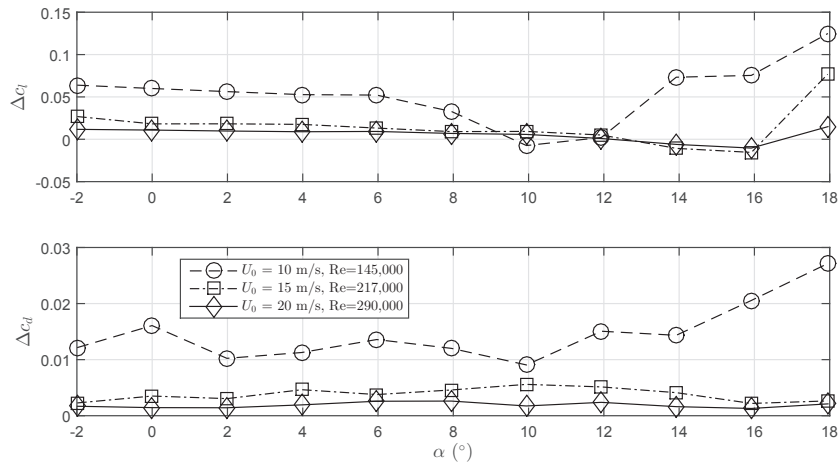


**Figure 5.47:** Variations of lift coefficient (per unit length of the actuator) relative to baseline as a function of freestream velocity and angle of attack for the half-round trailing-edge. The actuator is positioned on the pressure side blowing upstream (tab mode).

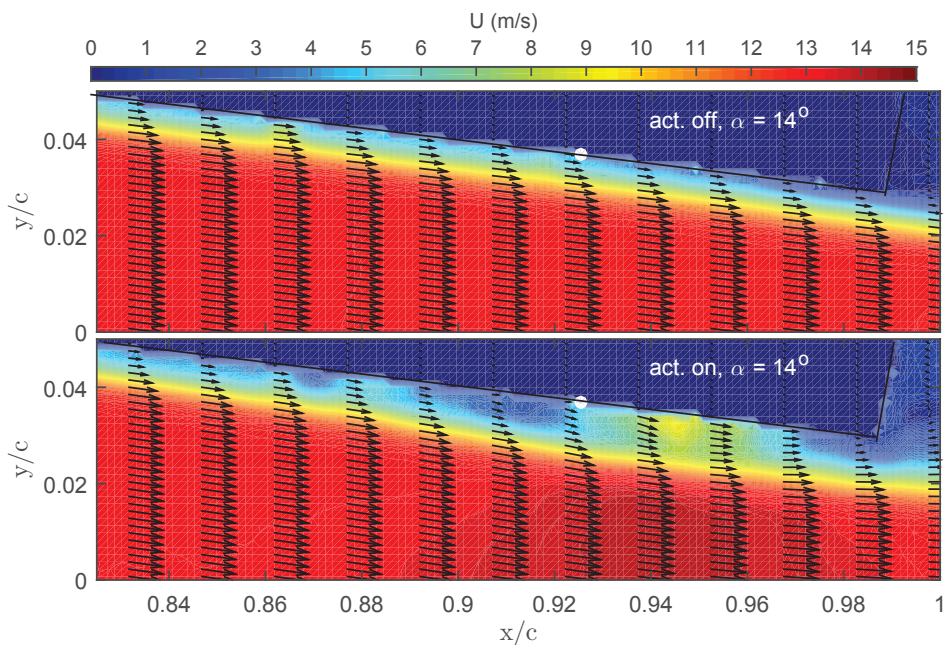


**Figure 5.48:** Time-averaged velocity vector field of the boundary layer for the half-round trailing-edge. The actuator is positioned on the pressure side blowing upstream (tab mode). The position of the plasma onset is shown with a white circle. ( $c_\mu = 0.3\%$ ,  $U = 10$  m/s,  $Re = 145,000$ )

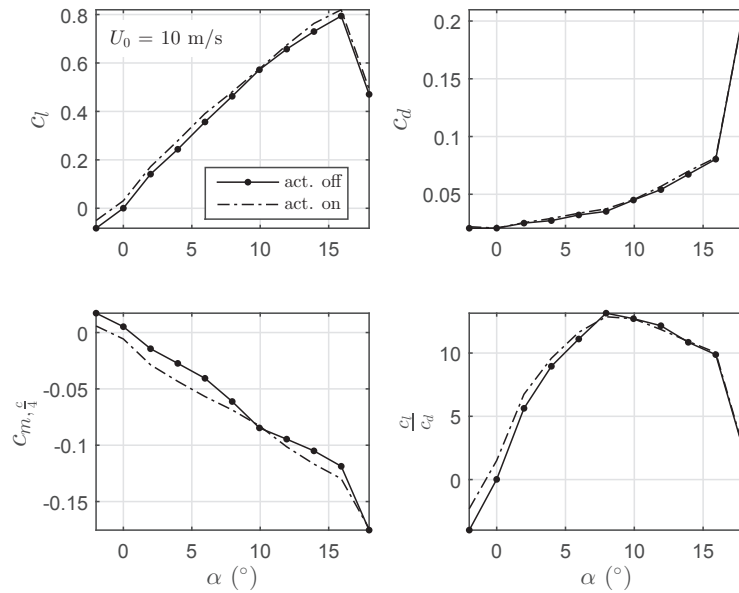


**Figure 5.49:** Lift, drag and moment coefficient as a function of angle of attack for the half-round trailing edge. One actuator is positioned at centerline of the trailing-edge (Kutta mode) and the second one on the pressure side blowing upstream (tab mode).

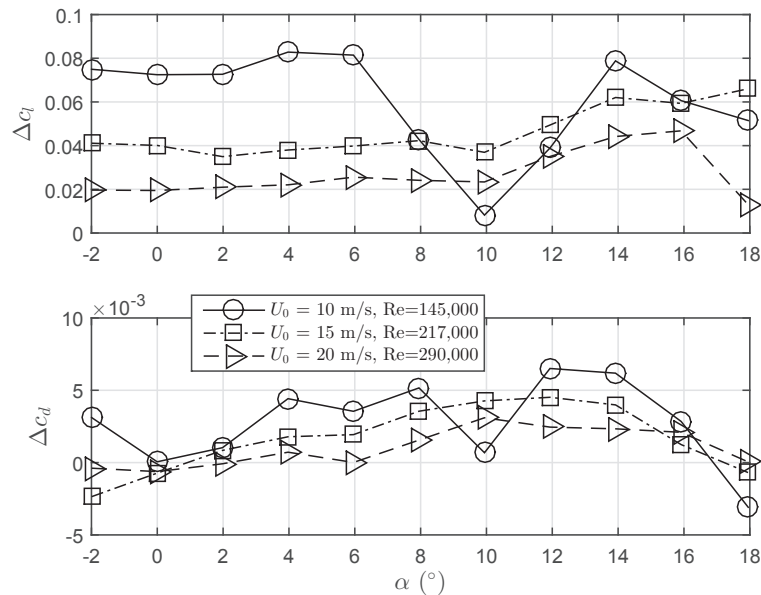


**Figure 5.50:** Variations of lift coefficient (per unit length of the actuator) relative to baseline as a function of freestream velocity and angle of attack for the half-round trailing-edge. One actuator is positioned at centerline of the trailing-edge (Kutta mode) and the second one on the pressure side blowing upstream (tab mode).

## 5.2.4.4 Comparison of modes

Figure 5.51 shows the variations of  $\Delta c_l$  as a function of  $\alpha$  for 3 different actuation modes. The result shows that double actuator operating mode (2push) which has 1-Kutta and 1-tab actuator is an approximate sum of the two other individual modes. Although the interference effects between the electrodes mounted close to each other slightly reduces the efficiency of double actuation as a result of creation of plasma in opposite direction.

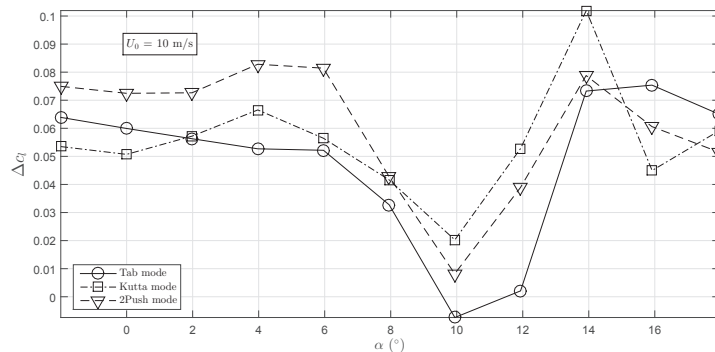


**Figure 5.51:** Variations of lift coefficient (per unit length of the actuator) relative to baseline as a function of freestream velocity and angle of attack for the half-round trailing-edge for different actuation modes (Kutta, tab and 2push modes).

## 5.3 Electrical consumed power measurements

Power measurements were done using the integrated capacitor method as explained in subsection 4.6.1. In these experiments, a wide range of applied voltage from  $20kV_{pp}$  to  $40kV_{pp}$  with steps of  $2.5kV_{pp}$  and carrier frequencies from  $100Hz$  to  $2000Hz$  with steps of  $100Hz$  were investigated for three different dielectric thicknesses of 1, 2 and  $3mm$ . The applied and capacitor voltage and the Lissajous curve for the case with  $40kV_{pp}$ ,  $f_c = 1000Hz$  and  $t_d = 3mm$  is shown in Figure 5.52. As already discussed, the area inside this curve equals the electrical consumed power of the actuator.

The same procedure has been done for all test cases and the electrical consumed power is plotted as a function of carrier frequency Figure 5.53-left. The results show a linear increase for the consumed power with carrier frequency where it saturates at high frequencies. The increase in power with frequency is simply because higher number of discharges occur per unit time.

It is seen that the slope of the lines increases with applied voltage and decreases with dielectric thickness. Therefore, electrical consumed power is plotted as a function of applied voltage Figure 5.53-right and dielectric thickness Figure 5.54.

As expected, it is observed that power increases with the voltage simply because the consumed power has a direct relation with the applied voltage ( $P_a(t) = V_a(t) \cdot I_a(t)$ ). The reduction in consumed power with increase in dielectric thickness is a result of larger distance between the electrodes by the dielectric and consequently larger resistance and a weaker discharge.

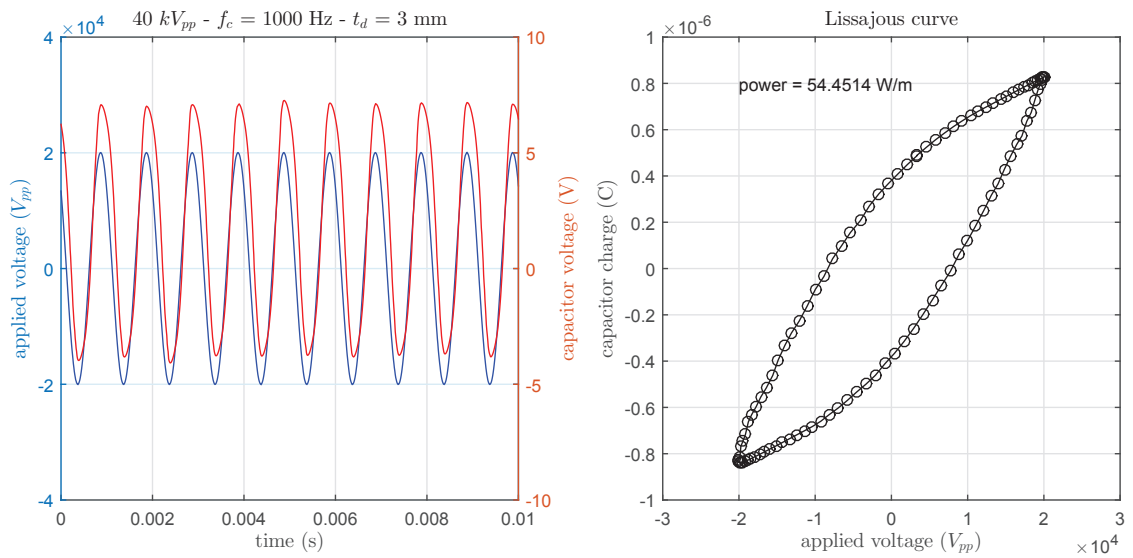


**Figure 5.52:** Applied and capacitor voltages (left) and Lissajous curve for one period (right) at  $40kV_{pp}$  and  $1000Hz$  carrier frequency. The dielectric thickness is  $3mm$ .

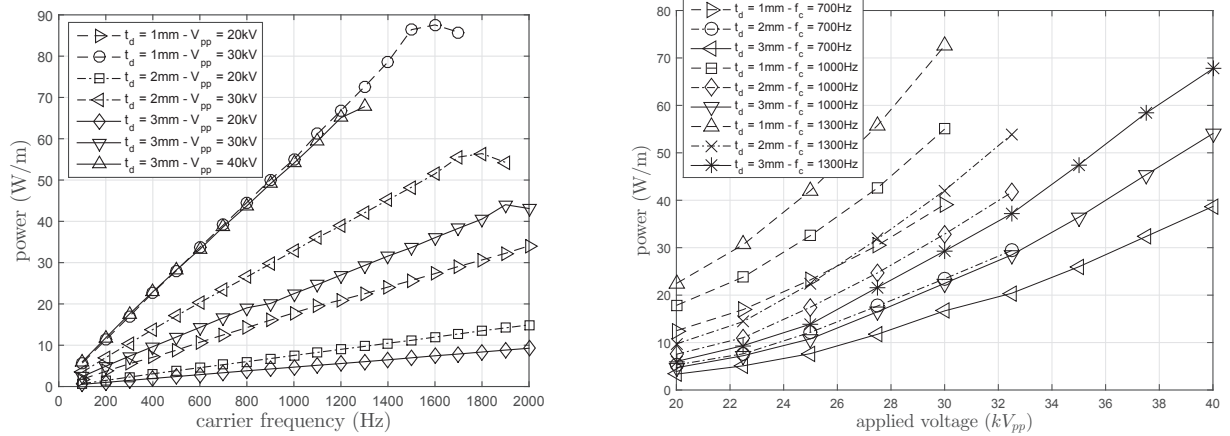


**Figure 5.53:** Electrical power consumption of the plasma actuator as a function of carrier frequency (left) and applied voltages (right).

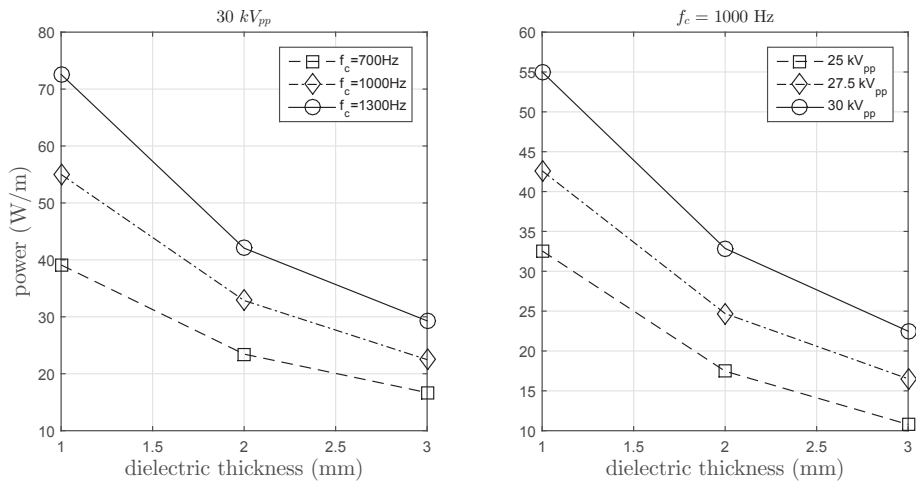


Figure 5.54: Electrical power consumption of the plasma actuator as a function of dielectric thickness.



# Conclusion

### 6.1 Concluding remarks

The first part of the thesis was focused on aeroelastic simulations using HAWC2 software in order to understand the amount of variations in lift coefficient under various operating scenarios. The main conclusion was that an average amount of 0.25 is a reasonable value over the span for the blades of a 10MW wind turbine. This amount is mainly a result of turbulence which can be from atmospheric boundary layer or wake of other turbines in a wind farm.

Another conclusion was that the main contributor to the flapwise lifetime equivalent fatigue loads is the turbulence while the dominant effect for the edgewise lifetime equivalent fatigue loads is the gravity. Controlling the unsteady loads due to turbulence will have a direct effect on reduction of the blade mass, therefore it directly decrease the flapwise and indirectly reduces the edgewise lifetime equivalent fatigue loads.

The first set of experiments was the quiescent flow experiments. It clarified the variations of the actuator force and momentum coefficient as a function of the applied voltage, carrier frequency and dielectric thickness of the actuator. It concluded a linear and a non-linear increase in force and momentum coefficient with frequency and applied voltage respectively where there is an optimum frequency. Force and momentum coefficient linearly decrease with dielectric thickness.

The second and third set of experiments were force and PIV measurements using the plasma actuator for the three different trailing-edges and various actuation modes. The conclusion was that the Kutta mode where the actuator is positioned at the center line of the trailing-edge can effectively change the position of stagnation point and manipulate the Kutta condition for the round and half-round trailing-edges where the effect is much more prominent for the round trailing-edge. This is believed to be the result of the sharp side of the half-round trailing-edge that limits the ability to change the Kutta condition.

The PIV results clarified that change in force is due to the deflection of the wake downwards by the actuator.

The experiments using the tab mode where the actuator is positioned on the pressure side blowing upstream showed the ability to change the lift coefficient within less than  $\pm 0.1$ . This is due to introduction of virtual camber to the airfoil by the actuator blowing.

The combined Kutta and tab mode using 2 actuators was not two times more effective as the actuators could not be installed very close to each other to have an interlinked effect because of arcing problems.

The study on the correlation between the carrier/pulsation frequency, change in lift coefficient and force variations did not show any interesting potential.

## 6.2 Future recommendations

Based on the experiences of the author in this thesis, the following recommendations can be given for future research:

- Upstream blowing on suction-side can be more promising for load alleviation rather than on the pressure side. However, the position of plasma blowing on pressure side needs to be further investigated as the current research only studied one position for the actuator. However, the close to the trailing-edge seems to have stronger effect in magnitude but having the effect in a narrower range of  $\alpha$  as the separated region will sooner cover the actuator.
- A combination of upstream blowing on pressure side and suction side can bring a wide range of control over lift coefficient which needs to be investigated for unsteady load control.
- Three-dimensional (staggered) electrode configuration at the trailing edge will create a 3D interference with the vortex shedding. This is believed to be able to work effectively to manipulate the 3D vortical structure in the wake and be able to affect the wake dynamics. Therefore, correlation between pulsation/carrier frequency, vortex shedding frequency and  $\Delta c_l$  needs to be studied with a 3D arrangement of electrodes at the trailing-edge.
- The transient (off-on-off) effect of plasma actuation on unsteady loads and wake dynamics using high-frequency force measurements and high-speed PIV needs to be further investigated.
- Experiments with multi-DBDs in this research was limited by the diameter of the trailing edge due to arcing problems and reverse-plasma-creation when electrodes were installed close to each other. However, still improvements over single DBD was achieved. Therefore, investigations on a bigger geometry where these problems can be avoided seems to be promising.

---

## References

- [1] Ambient ionization, 2014. URL [http://en.wikipedia.org/wiki/Ambient\\_ionization](http://en.wikipedia.org/wiki/Ambient_ionization).
- [2] Peter Bjoern Andersen, Lars Henriksen, Mac Gaunaa, Christian Bak, and Thomas Buhl. Deformable trailing edge flaps for modern megawatt wind turbine controllers using strain gauge sensors. *Wind Energy*, 13(2-3):193–206, 2010. ISSN 10954244 10991824. doi: 10.1002/we.371.
- [3] David E. Ashpis, Matthew C. Laun, and Elmer L. Griebeler. Progress toward accurate measurements of power consumptions of dbd plasma actuators. In *50th Aerospace Sciences Meeting*, Nashville, Tennessee, 2012.
- [4] F. Bacchi and A. Scarabino. Aerodynamic loads on a fixed wind turbine blade with gurney flap, 2014.
- [5] A. B. Bach, M. Lennie, G. Pechlivanoglou, C. N. Nayeri, and C. O. Paschereit. Finite micro-tab system for load control on a wind turbine. *Journal of Physics: Conference Series*, 524:012082, 2014.
- [6] P. Bak. *Unsteady Flow Modeling and Experimental Verification of Active Flow Control Concepts for Wind Turbine Blades*. Thesis, 2011.
- [7] A. K. Barlas. *Active aerodynamic load control on wind turbines: Aeroservoelastic modeling and wind tunnel*. Thesis, 2011.
- [8] T. K. Barlas and G. A. M. van Kuik. Review of state of the art in smart rotor control research for wind turbines. *Progress in Aerospace Sciences*, 46(1):1–27, 2010. ISSN 03760421. doi: 10.1016/j.paerosci.2009.08.002.
- [9] Rae W.H. Barlow, J.B. and A. Pope. *Low-Speed Wind Tunnel Testing, 3rd edition*. John Wiley, 1999.
- [10] L. Bergami. *Smart Rotor Modeling: Aero-Servo-Elastic Modeling of a Smart Rotor with Adaptive Trailing Edge Flaps*. Springer, 2014.
- [11] Jos A Bittencourt. *Fundamentals of plasma physics*. Springer, 2004. ISBN 0387209751.
- [12] T.F. Brooks and M.A. Marcolini. Airfoil trailing edge flow measurements and comparison with theory incorporating open wind tunnel corrections. In *AIAA/NASA 9th Aeroacoustics Conference*, Williamsburg, Virginia, 1984.
- [13] M. Caduff, M. A. Huijbregts, H. J. Althaus, A. Koehler, and S. Hellweg. Wind power electricity: the bigger the turbine, the greener the electricity. *Environmental Science and Technology*, 46(9):4725–33, 2012. doi: 10.1021/es204108n.
- [14] D. Caruana. Flow control by plasma in plasmaero project, 2011.
- [15] Louis N. Cattafesta and Mark Sheplak. Actuators for active flow control. *Annual Review of Fluid Mechanics*, 43(1):247–272, 2011. ISSN 0066-4189 1545-4479. doi: 10.1146/annurev-fluid-122109-160634.
- [16] M.A. Cavanaugh, P. Robertson, and W.H. Mason. Wind tunnel test of gurney flaps and t-strips on an naca 23012 wing, 2007.
- [17] R. Chow and C. P. Van Dam. Computational investigations of deploying load control microtabs on a wind turbine airfoil. In *Proceedings of the 45th AIAA/ASME*, 2007.
- [18] Thomas C. Corke, Martiqua L. Post, and Dmitry M. Orlov. Sdbd plasma enhanced aerodynamics: concepts, optimization and applications. *Progress in Aerospace Sciences*, 43(7-8):193–217, 2007.

- [19] Gael de Oliveira. Wind turbine airfoils with boundary layer suction: A novel design approach. Master's thesis, 2011.
- [20] A. Dialoupis. Active flow control using plasma actuators: Application on wind turbines. Thesis, 2014.
- [21] DTU-Riso. Material for 'hawc2 online course'. Report, 2014.
- [22] C. Lon Enloe, Thomas E. McLaughlin, Robert D. Van Dyken, K. D. Kachner, Eric J. Jumper, Thomas C. Corke, M. Post, and O. Haddad. Mechanisms and responses of a dielectric barrier plasma actuator: Geometric effects. *AIAA Journal*, 42(3):595–604, 2004.
- [23] CL Enloe, MG McHarg, GI Font, and Th E McLaughlin. Plasma-induced force and self-induced drag in the dielectric barrier discharge aerodynamic plasma actuator. *AIAA Paper*, 1622:2009, 2009.
- [24] Zoran Falkenstein and John J Coogan. Microdischarge behaviour in the silent discharge of nitrogen-oxygen and water-air mixtures. *Journal of Physics D: Applied Physics*, 30(5):817, 1997. ISSN 0022-3727.
- [25] Maxime Forte, Jerome Jolibois, J Pons, E Moreau, G Touchard, and M Cazalens. Optimization of a dielectric barrier discharge actuator by stationary and non-stationary measurements of the induced flow velocity: application to airflow control. *Experiments in Fluids*, 43(6):917–928, 2007. ISSN 0723-4864.
- [26] Mohamed Gad-el Hak. *Flow Control: passive, active, and reactive flow management*. Cambridge University Press, 2000.
- [27] M. Gaunaa and J. Johansen. Determination of the maximum aerodynamic efficiency of wind turbine rotors with winglets. *Journal of Physics: Conference Series*, 75, 2007. doi: 10.1088/1742-6596/75/1/012006.
- [28] A. Gross and H. F. Fasel. Flow control for nrel s822 wind turbine airfoil. *AIAA Journal*, 50(12):2779–2790, 2012.
- [29] G.W. Gyatt. Development and testing of vortex generators for small horizontal axis wind turbines. Report DOE/NASA/0367-1, NASA/DOE, 1987.
- [30] M.H. Hansen, M. Gaunaa, and H.A. Madsen. A beddoes-leishman type dynamic stall model in state-space and indicial formulations. Report, Riso-DTU, 2004.
- [31] International Electrotechnical Commission (IEC). Iec 61400-1 edition 3 - wind turbines - part 1: Design requirements, 2005.
- [32] Muhammad O Iqbal, Alexey Kozlov, David Schatzman, Hesham Othman, Flint Thomas, and Thomas Corke. Parametric optimization of single dielectric barrier discharge (sdbd) plasma actuators. In *59th Annual Meeting of the APS Division of Fluid Dynamics*, Tampa Bay, Florida, 2006.
- [33] Balaji Jayaraman and Wei Shyy. Modeling of dielectric barrier discharge-induced fluid dynamics and heat transfer. *Progress in Aerospace Sciences*, 44(3):139–191, 2008. ISSN 03760421. doi: 10.1016/j.paerosci.2007.10.004.
- [34] J.L. Jimenez. Ionization techniques - part 1. Report, 2006.
- [35] Scott J. Johnson, Jonathon P. Baker, C. P. van Dam, and Dale Berg. An overview of active load control techniques for wind turbines with an emphasis on microtabs. *Wind Energy*, 13(2-3):239–253, 2010. ISSN 10954244 10991824. doi: 10.1002/we.356.
- [36] J. Jonkman, S. Butterfield, W. Musial, and G. Scott. Definition of a 5-mw reference wind turbine for offshore system development. Report, NREL, 2009.
- [37] Ulrich Kogelschatz. Filamentary, patterned, and diffuse barrier discharges. *Plasma Science, IEEE Transactions on*, 30(4):1400–1408, 2002. ISSN 0093-3813.
- [38] M. Kotsonis and S. Ghaemi. Forcing mechanisms of dielectric barrier discharge plasma actuators at carrier frequency of 625 hz. *Journal of Applied Physics*, 110(11):113301, 2011. ISSN 00218979. doi: 10.1063/1.3664695.
- [39] Marios Kotsonis, Robin Pul, and Leo Veldhuis. Influence of circulation on a rounded-trailing-edge airfoil using plasma actuators. *Experiments in Fluids*, 55(7), 2014.
- [40] Erich E Kunhardt. Electrical breakdown of gases: The prebreakdown stage. *Plasma Science, IEEE Transactions on*, 8(3):130–138, 1980. ISSN 0093-3813.
- [41] J. Kweder, C.C. Panther, and J.E. Smith. Applications of circulation control, yesterday and today. *International Journal of Engineering*, 4(5):411–429, 2008.
- [42] Matthew A. Lackner and Gijs van Kuik. A comparison of smart rotor control approaches using trailing edge flaps and individual pitch control. *Wind Energy*, 13(2-3):117–134, 2010. ISSN 10954244 10991824. doi: 10.1002/we.353.
- [43] T. J. Larsen and A.M. Hansen. How 2 hawc2, the user's manual (ris-r-1597 ver. 4-5 ). Report, Ris

- National Laboratory, DTU, 2014.
- [44] S. Lee, M. Churchfield, P. Moriarty, J. Jonkman, and J. Michalakes. Atmospheric and wake turbulence impacts on wind turbine fatigue loading, 2012.
- [45] J.G. Leishman and T.S. Beddoes. A semi-empirical model for dynamic stall. *Journal of the American Helicopter Society*, 34(3):3–17, 1989.
- [46] Victor Maldonado, John Farnsworth, William Gressick, and Michael Amitay. Active control of flow separation and structural vibrations of wind turbine blades. *Wind Energy*, 13(2-3):221–237, 2010.
- [47] Helen Markou, Peter Bjrnr Andersen, and Gunner Chr Larsen. Potential load reductions on megawatt turbines exposed to wakes using individual-pitch wake compensator and trailing-edge flaps. *Wind Energy*, 14(7):841–857, 2011. doi: 10.1002/we.431.
- [48] R. C. Nelson, T. C. Corke, H. Othman, M. P. Patel, S. vasudevan, and T. Ng. A smart wind turbine blade using distributed plasma actuators for improved performance, 2008.
- [49] D.M. Orlov. *Modelling And Simulation Of Single Dielectric Barrier Discharge Plasma Actuators*. Thesis, 2006.
- [50] G. Pechlivanoglou. *Passive and active flow control solutions for wind turbine blades*. Thesis, 2013.
- [51] K. Pierce and A. C. Hansen. Prediction of wind turbine rotor loads using the beddoes-leishman model for dynamic stall. *Journal of Solar Energy Engineering*, 117(3):200–204, 1995. ISSN 0199-6231.
- [52] Robin Pul. Dielectric barrier discharge plasma actuators for unsteady aerodynamic load control. Master’s thesis, 2013.
- [53] Yong-Xing Qiu, Xiao-Dong Wang, Shun Kang, Ming Zhao, and Jun-Yu Liang. Predictions of unsteady hawt aerodynamics in yawing and pitching using the free vortex method. *Renewable Energy*, 70:93–106, 2014. ISSN 09601481. doi: 10.1016/j.renene.2014.03.071.
- [54] M. Raffel. *Particle Image Velocimetry A Practical Guide*. Experimental Fluid Mechanics. Springer, Dordrecht, 2007.
- [55] JR Roth. Industrial plasma engineering. *IOP, Bristol and Philadelphia*, 1995.
- [56] D. V. Roupasov, A. A. Nikipelov, M. M. Nudnova, and A. Yu Starikovskii. Flow separation control by plasma actuator with nanosecond pulsed-periodic discharge. *AIAA Journal*, 47(1):168–185, 2009.
- [57] S. Salcedo, F. Monge, F. Palacios, F. Gandia, A. Rodriguez, and M. Baarcala. Gurney flaps and trailing edge devices for wind turbines, 2006.
- [58] F. Scarano and M. L. Riethmuller. Iterative multigrid approach in piv image processing with discrete window offset. *Experiments in Fluids*, 26(6):513–523, 1999. ISSN 0723-4864. doi: 10.1007/s003480050318. URL <http://dx.doi.org/10.1007/s003480050318>.
- [59] Andreas Schroder. *Particle Image Velocimetry New Developments and Recent Applications*. Topics in Applied Physics, Volume 112. Springer, Dordrecht, 2008.
- [60] S. Shun and N. A. Ahmed. Wind turbine performance improvements using active flow control techniques. *Procedia Engineering*, 49:83–91, 2012.
- [61] L. Sirovich. Turbulence and the dynamics of coherent structures. *Quarterly Of Applied Mathematics*, 45:561–571, 1987.
- [62] A. Yu Starikovskii, A. A. Nikipelov, M. M. Nudnova, and D. V. Roupasov. Sdbd plasma actuator with nanosecond pulse-periodic discharge. *Plasma Sources Science and Technology*, 18(3):034015, 2009.
- [63] Bruce L. Storms and Cory S. Jang. Lift enhancement of an airfoil using a gurney flap and vortex generators. *Journal of Aircraft*, 31(3):542–547, 1994. ISSN 0021-8669 1533-3868. doi: 10.2514/3.46528.
- [64] H.J. Sutherland. On the fatigue analysis of wind turbines. Report, Sandia National Laboratories, 1999.
- [65] Flint O Thomas, Thomas C Corke, Muhammad Iqbal, Alexey Kozlov, and David Schatzman. Optimization of dielectric barrier discharge plasma actuators for active aerodynamic flow control. *AIAA journal*, 47(9):2169–2178, 2009. ISSN 0001-1452.
- [66] Chanin Tongchitpakdee, Sarun Benjanirat, and Lakshmi N. Sankar. Numerical studies of the effects of active and passive circulation enhancement concepts on wind turbine performance. *Journal of Solar Energy Engineering*, 128(4):432, 2006. ISSN 0199-6231.
- [67] TUDelft. Course material for ‘introduction to wind energy’ at tu delft. Report, 2014.
- [68] UpWind. Design limits and solutions for very large wind turbines. Report, EWEA, 2011.
- [69] UpWind. Design and verification of an airfoil with trailing-edge flap and unsteady wind-tunnel tests. Technical Report UPWIND WP1B3, UpWind, 2011.
- [70] Guannan Wang, Jakub Walczak, Basman Elhadidi, Mark Glauser, and Hiroshi Higuchi. Preliminary

- investigation of the active flow control benefits on wind turbine blades. 2011.
- [71] Jay P. Wilhelm, Emily D. Pertl, Franz A. Pertl, and James E. Smith. Performance predictions of a circulation controlled-vertical axis wind turbine with solidity control. *Proceedings of the ASME 3rd International Conference on Energy Sustainability 2009, ES2009*, 2:1001–1007, 2009. ISSN 9780791848906.
  - [72] T. Wolff, B. Ernst, and J. R. Seume. Aerodynamic behavior of an airfoil with morphing trailing edge for wind turbine applications. *Journal of Physics: Conference Series*, 524:012018, 2014. ISSN 1742-6596. doi: 10.1088/1742-6596/524/1/012018.
  - [73] P. Zhang, B. Yan, A. B. Liu, and J. J. Wang. Numerical simulation on plasma circulation control airfoil. *AIAA Journal*, 48(10):2213–2226, 2010.
  - [74] Wan Li Zhao and Xiao Lei Zheng. Numerical simulation on the flow control by mounting indented gurney flaps for a wind turbine. *Advanced Materials Research*, 512-515:623–627, 2012. ISSN 1662-8985. doi: 10.4028/www.scientific.net/AMR.512-515.623.
  - [75] L. Zwang. Boundary layer suction on a horizontal axis wind turbine: An aerodynamic design of a thick airfoil for application. Master’s thesis, 2009.

---

## Appendix A

---

# Appendix A: Correction for the ratio between the actuator length and airfoil span

In order to declare the load control of the plasma actuator regardless of the actuator length, the change in lift coefficient by the actuator needs to be expressed per unit meter of the actuator. However, due to arcing problems electrodes are installed in the center of the airfoil span, therefore, their induced change in lift coefficient is dependent on the ratio between the actuator length and airfoil span. Having said that, in order understand this effect an analytical solution is presented.

Assuming an airfoil with unity span ( $span = 1m$ ),  $0.217m$  chord having  $6N$  lift in a flow with  $60Pa$  dynamic pressure  $q_\infty$ . This will lead to Equation A.1,

$$c_l = \frac{L}{q_\infty \cdot S} = 0.4608 \quad (A.1)$$

where  $S$  is area equal to  $S = chord \cdot span$ . Now assuming plasma actuators with electrode lengths  $0.05 - 1m$  generating lift of  $0.1 - 1.2N$  are installed on the airfoil. The new lift coefficient with actuator on can be calculated from Equation A.2,

$$c_{l,on} = \frac{L + L_{act.}}{q_\infty \cdot S} \quad (A.2)$$

where  $c_{l,on}$  is the lift coefficient with actuator on and  $c_l$  is the lift produced by the actuator. Therefore, the change in lift coefficient by the actuator is calculated from Equation A.3.

$$\Delta c_l = c_{l,on} - c_l \quad (A.3)$$

Based on this calculation, the change in lift coefficient by the actuator per unit length of the actuator versus the ratio between the actuator length and airfoil span is shown in Figure A.1-top.

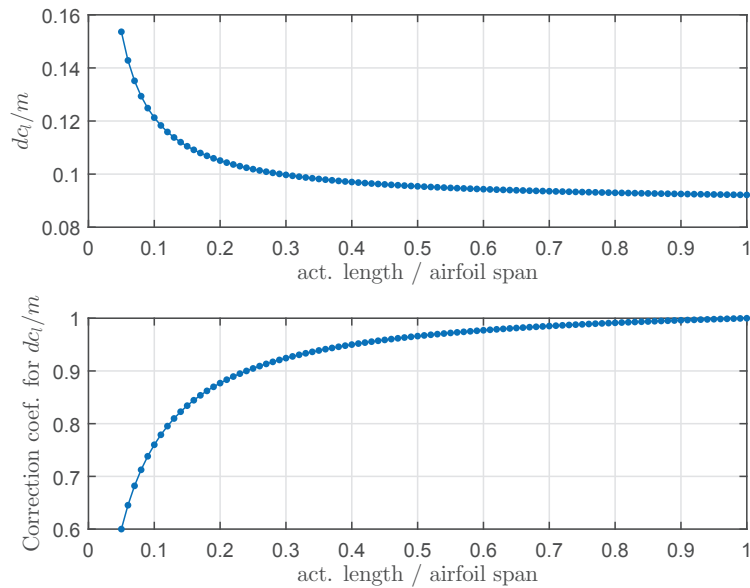


**Figure A.1:** Change in lift coefficient by the actuator per unit length of the actuator (top) and correction factor for force coefficient (bottom) versus the ratio between the actuator length and airfoil span.

Based on this calculation and considering the correct value for  $\Delta C_l$  to be when the actuator has the electrodes the same size as the airfoil span, a correction factor for force coefficient can be defined which is shown versus the ratio between the actuator length and airfoil span (Figure A.1-bottom).

This correction coefficient needs to be multiplied to measured lift coefficient per unit length of the actuator in order to correct for the ratio between the actuator length and airfoil span.

From Figure A.1, it is inferred that as the ratio between the electrode length and airfoil span becomes more than 0.5, i.e. the actuator electrode is half of the airfoil span or more, the correction factor is very small and gradually approaches unity. However, for smaller ratios the correction factor is notable.

---

## Appendix B

---

# Appendix B: Plasma model for prediction of body force spatial distribution

Within the work of this thesis, a plasma model is developed to predict the plasma actuator body force spatial distribution based on charge density  $\rho_c$  of the plasma and its electric field  $E$  based on Equation B.1 where charge density is in  $C/m^3$ , electric field is in  $N/C$  or  $C/m$  and the force density or force per unit volume ( $f$ ) is in  $N/m^3$ . [33] The force density distribution times the effective volume where contains the plasma results in body force spatial distribution.

$$f = E \cdot \rho_c \tag{B.1}$$

The charge density is assumed to be equal to plasma light intensity times a coefficient which needs to be identified through an iterative process. This assumption lies on the fact that light emission occurs when an electron jumps from an outer orbit to an inner orbit of an ion. Therefore, a simple assumption is wherever there is more light, therefore there is more electrons going into inner orbits, consequently there are more charge carriers (i.e. ions and electrons). This simply means charge density is higher in that region. But this can not conclude that regions with the same light have exactly the same light intensity as it might be from different ions with different charge. Moreover, no conclusion can be made on the composition of the plasma emitting light or its energetic state as the light emission is highly complex dependency on the energetic states of the ions, their spontaneous emission rates, the density and the excitation temperature. This maybe known using emission spectroscopy or probably wisely selected bandpass filters if the composition allows some bandpass to be dominant by one species only.

The plasma light intensity is measured using imaging using a high-sensitivity high quantum efficiency SensiCam. The light intensity for a plasma actuator with  $3mm$  thickness dielectric operating at  $40kV_{pp}$  and  $1300Hz$  is shown in Figure B.1.

As the plasma actuator emission is the plasma created from air is dominant mainly by Nitrogen ions and then Oxygen ions. The emission from Nitrogen is much intenser and in bluish color compared to emission from Oxygen which is whitish and much less intense. Therefore, the total emission is far dominated by Nitrogen ions. However, the role of Oxygen ions in the actuator body force can not be neglected.

Bandpass filter of  $394nm$  and  $694nm$  with pass width of  $10nm$  were used to only allow the emission of Nitrogen and Oxygen, respectively to get to camera sensor. But as the emission was so much restricted by the filters, much higher exposure time was needed in order to have enough light. However, the camera

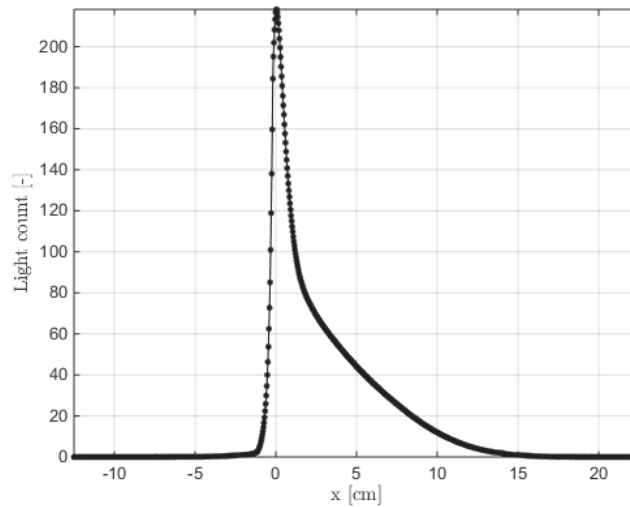


*Figure B.1: Light intensity of plasma actuator using Sensicam. Plasma onset is at about  $x = 0$ .*

exposure time was limited to 1sec. This failed the tests with 694nm filter and the distribution of Oxygen ions were not know. However, the results for the 394nm filter representing the distribution of Nitrogen ions is shown in Figure B.2.

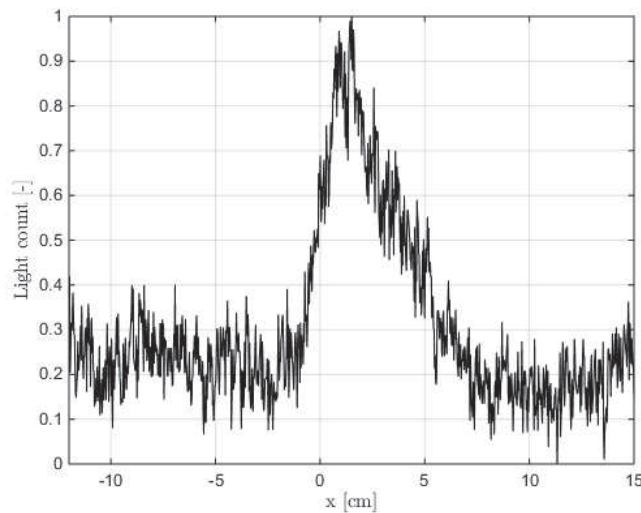


*Figure B.2: Light intensity of plasma actuator using Sensicam and a 394nm bandpass filter which only allows emission from some energetic states of Nitrogen. Plasma onset is at about  $x = 0$ .*

As already discussed, the total emission is dominant by Nitrogen, therefore, the filtered emission of Nitrogen looks similar to total emission shown in Figure B.1.

Based on the results of imaging, an exponential fit is selected to be representative of charge density distribution along the x axis. The normal distribution of charge density along the y axis is also assumed to be exponential, higher near the surface and reducing as getting farther from the surface.

The electric field is composed of the field created by the potential between the exposed and covered electrode plus the charge induced electric field. The When charge density is know, the electric field can be calculated

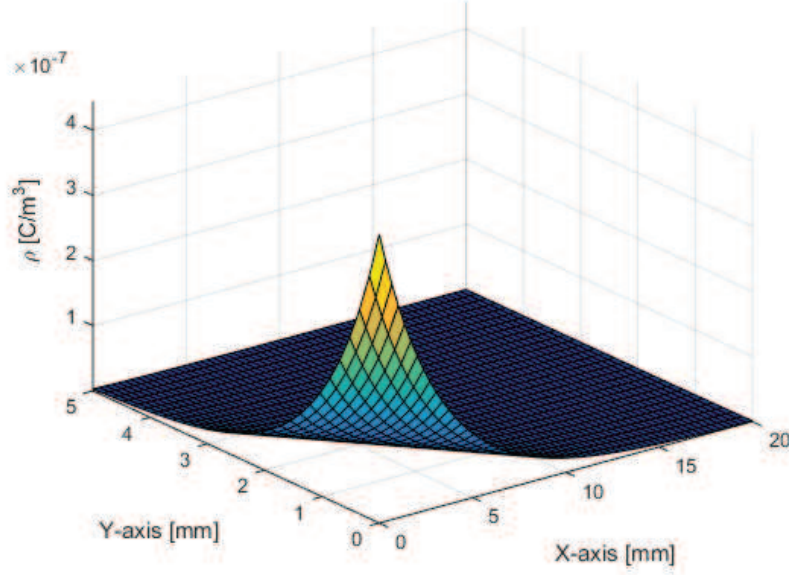


*Figure B.3: Defined spatial distribution for charge density based on plasma emission.*

by solving the Poisson equation as below:

$$\nabla \cdot \vec{E} = \frac{\rho_c}{\epsilon_0} \quad (\text{B.2})$$

$$E = -\nabla V \quad (\text{B.3})$$

$$\nabla^2 V = -\frac{\rho_c}{\epsilon_0} \quad (\text{B.4})$$

This equation is solved using *MATLAB pde tool* for the plasma actuator with 25mm exposed electrode, 15mm covered electrode and 3mm thickness dielectric with dielectric constant  $\epsilon = 3.2$ . In order to solve the equation, the geometry is created and meshed using unstructured adaptive meshing algorithm which refines the mesh where the gradients are higher during the solution iterations. The results then are interpolated into a structured grid for post processing as shown Figure B.4. In the geometry a rectangular region over the covered electrode is defined as the region containing the plasma. This region is defined large enough to contain all the plasma created.

The electric potential calculated and interpolated to structured grid are shown in Figure B.5 and Figure B.6 and the electric field is shown in Figure B.7 and Figure B.8.

Having solved the Poisson equation, now we have the charge density and electric field. By point by point multiplication, we will have the spatial distribution of the body force as shown in Figure B.9 and Figure B.10. The surface under the force plot results in the total force of the actuator.

At this initial stage, it is seen that due to first-guess setting of the calibration coefficient for the charge density, there is a region of very high charge-induced electric field near the plasma onset which results in negative force in that region which seems not matching the physics. This is where the iterative process starts to change the calibration coefficient for the charge density and solve the equations to calculate the integral

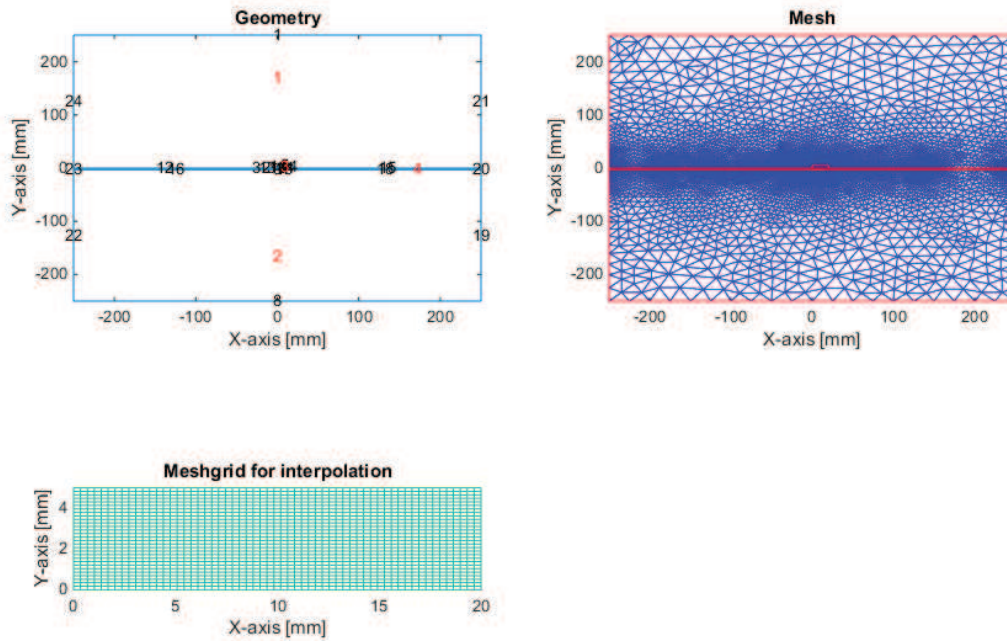


Figure B.4: Geometry, unstructured and structured grid created to solve the Poisson equation in MATLAB pdetool.

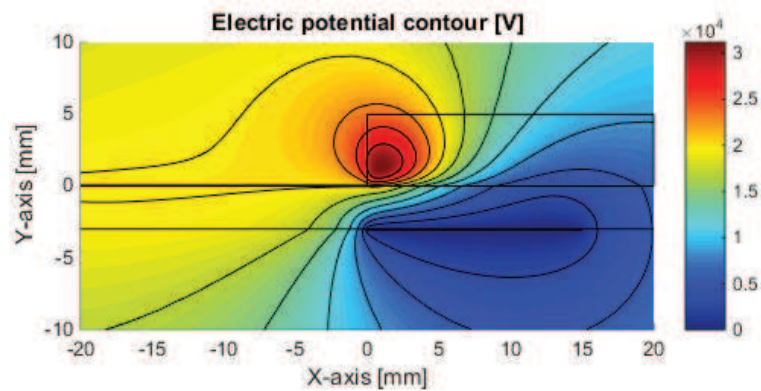


Figure B.5: Electric potential calculated for the plasma actuator in MATLAB pdetool. The upper rectangular region represents the plasma containing region.

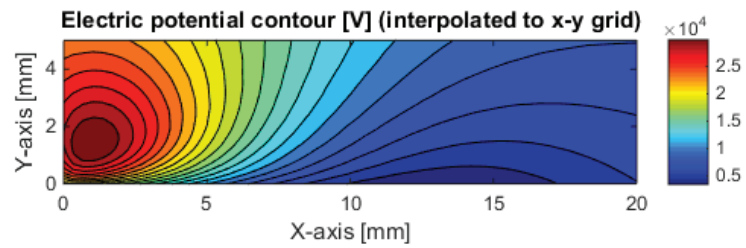


Figure B.6: Electric potential calculated for the plasma actuator in MATLAB pde tool interpolated to structured grid.

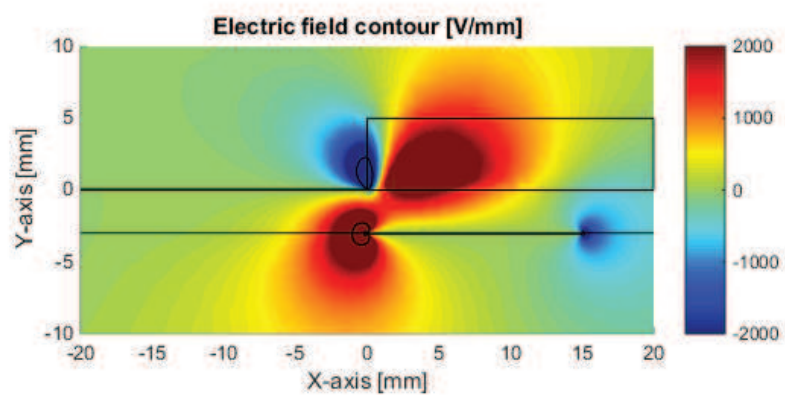


Figure B.7: Electric field calculated for the plasma actuator in MATLAB pde tool.

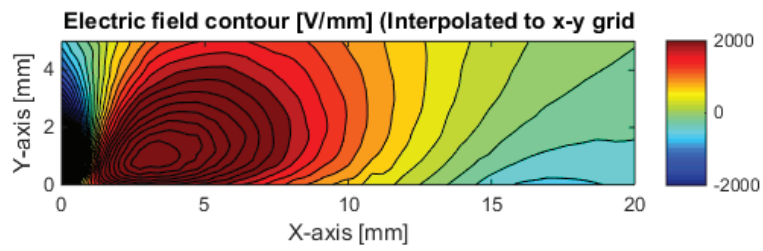


Figure B.8: Electric field calculated for the plasma actuator in MATLAB pdetool interpolated to structured grid.

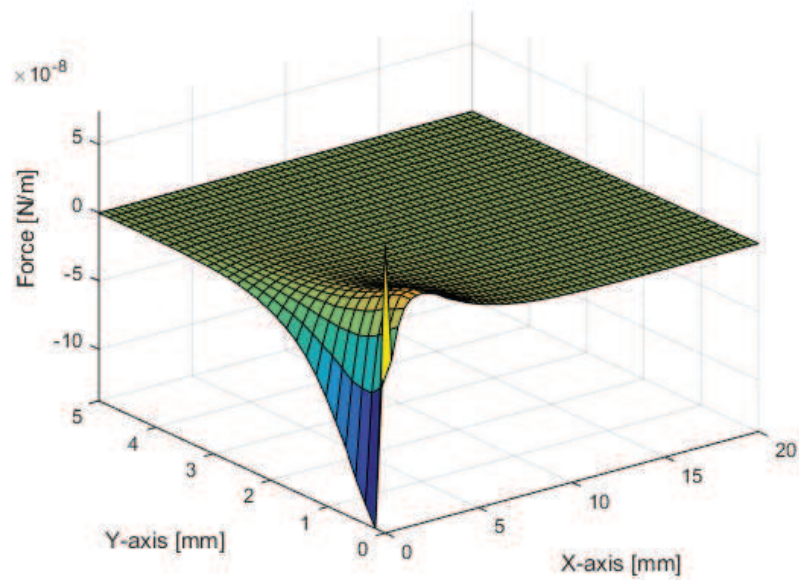
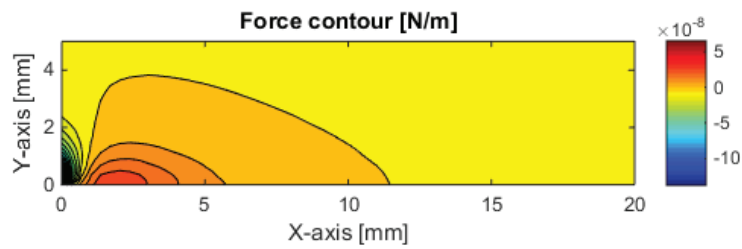
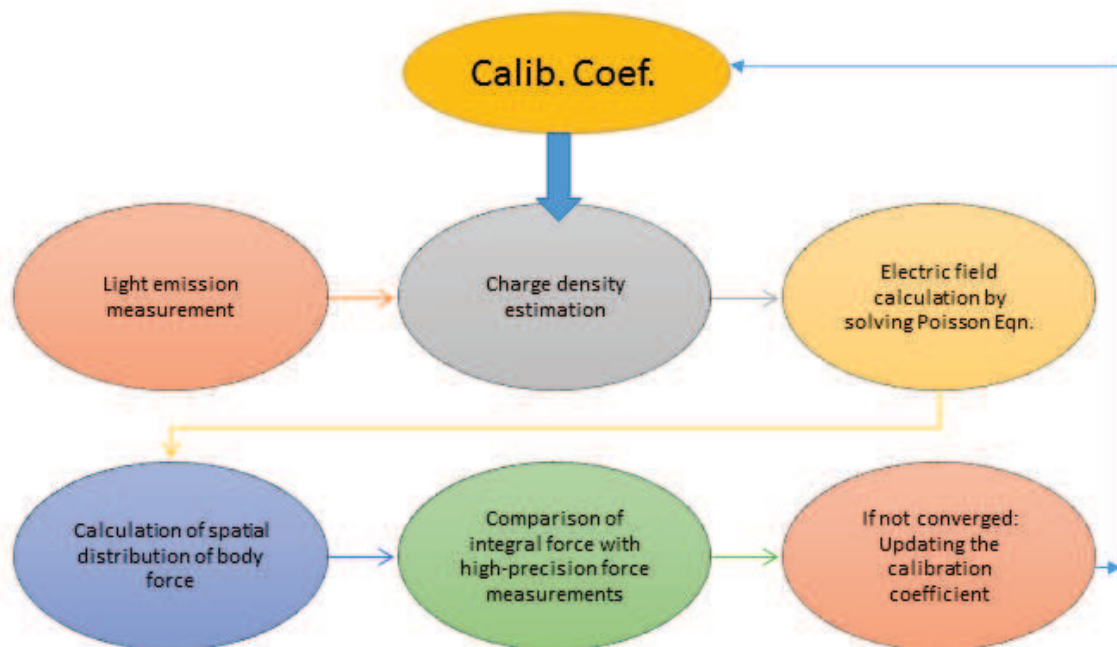


Figure B.9: Body force spatial distribution calculated for the plasma actuator.



*Figure B.10: Body force spatial distribution calculated for the plasma actuator.*

body force. The criteria for convergence will be when the integral body force reached within a tolerance from the quiescent-air experimental measurements of integral body force for the same actuator which are presented in *chapter 5*. When converged, the body force distribution is finalized. The flowchart of the iterative process is shown in Figure B.11.



*Figure B.11: Flowchart of iterative process to calculate the body force spatial distribution for the plasma actuator.*